Photocatalytic Synthesis of Hydrogen Peroxide from Molecular Oxygen and Water

Patricia Garcia-Munoz, Laura Valenzuela, Deborah Wegstein, Tobias Schanz, Girlie Eunice Lopez, Agnieszka Ruppert, Hynd Remita, Jonathan Bloh, Nicolas Keller

Photocatalytic Synthesis of Hydrogen Peroxide from Molecular Oxygen and Water

Patricia Garcia-Munoz,[2] Laura Valenzuela,[1] Deborah Wegstein,[3] Tobias Schanz,[3] Girlie Eunice Lopez,[4] Agnieszka M. Ruppert,[5] Hynd Remita,[4] Jonathan Z. Bloh,[3] Nicolas Keller[1,*]

[1] Institut de Chimie et Procédés pour l'Energie, l'Environnement et la Santé (ICPEES), CNRS/University of Strasbourg, 25 rue Becquerel, Strasbourg, France

[2] Department of Chemical and Environmental Engineering, Escuela Técnica Superior de Ingenieros Industriales, Universidad Politécnica de Madrid, 28006 Madrid, Spain

[3] DECHEMA-Forschungsinstitut, Theodor-Heuss-Allee 25, 60486 Frankfurt am Main, Germany

[4] Institut de Chimie Physique, CNRS UMR 8000, Université Paris-Saclay, 91405 Orsay, France

[5] Institute of General and Ecological Chemistry, Lodz University of Technology, Żeromskiego 116, 90-924 Łódź, Poland

* Corresponding author's address: nkeller@unistra.fr

Keywords

Hydrogen peroxide synthesis ; photocatalyst ; titania ; graphitic carbon nitride ; water treatment ; reaction mechanism

Acknowledgements:

The MOPGA program is acknowledged for funding the fellowship of Laura Valenzuela.

Abstract

Hydrogen peroxide is a powerful and green oxidant that allows for the oxidation of a wide span of organic and inorganic substrates in liquid media under mild reaction conditions, and forms only molecular water and oxygen as end-products. Hydrogen peroxide is therefore used in a wide range of applications, for which the well-documented and established anthraquinone autoxidation process is by far the dominating production way at the industrial scale. That method being highly energy-consuming and environmentally-costly, the search for more sustainable synthesis methods is of high interest. To this end, the article reviews the basis and the recent development of the photocatalytic synthesis of hydrogen peroxide. Different oxygen reduction and water oxidation mechanisms are discussed, as well as several kinetic models, and the influence of the main key reaction parameters is itemized. A large range of photocatalytic materials is reviewed, with emphasis on titania-based photocatalysts and on high-prospect graphitic carbon nitride based systems that take advantage of advanced bulk and surface synthetic approaches. Strategies for enhancing the performances of solar-driven photocatalysts are reported, and the search for new, alternative, photocatalytic materials is detailed. Finally, the promise of *in-situ* photocatalytic synthesis of hydrogen peroxide for water treatment and organic synthesis is described, as well as its coupling with enzymes and the direct *in-situ* synthesis of other technical peroxides.

1. Hydrogen peroxide: from chemistry to applications

1.1. Chemistry of hydrogen peroxide

Hydrogen peroxide (H_2O_2) is an odorless, colorless, and versatile liquid oxidant that shows high oxidation potential over the whole pH range, with E_0 = 1.763 V and 0.878 V at pH 0 and 14, respectively. It is an environmentally friendly oxidant under mild conditions, as it generates only oxygen and water as decomposition products according to reaction (1). The decomposition of H_2O_2 requires careful control as it forms gaseous oxygen with the release of heat at 100 kJ.mol^{-1}. Many compounds are able to catalyze the decomposition of H_2O_2, such as most of the transition metals and some organic substances.

Decomposition $$H_2O_2 \rightarrow H_2O + \frac{1}{2}O_2 \quad (1)$$

H_2O_2 is a powerful oxidant allowing the oxidation of a wide span of organic and inorganic substrates in liquid media (2). Also, H_2O_2 allows addition reactions in liquid phase, and molecularly binds to compounds such as metal peroxides with alkaline-earth or alkali metals, percarbonates or oxoacid salts among others (3). Further, the strong reducing power of H_2O_2 allows the reduction of strong oxidants like $KMnO_4$ or $Ce(SO_4)_2$, which is the basis for some volumetric methods for determining the H_2O_2 concentration (4). Last, substitution reactions with organic reactants can take place, with the formation of peroxido molecules in particular extensively used in organic synthesis (5).

Oxidation $$H_2O_2 + M \rightarrow H_2O + MO \quad (2)$$

Addition $$H_2O_2 + A \rightarrow AH_2O_2 \quad (3)$$

Reduction $$H_2O_2 + R \rightarrow RH_2 + O_2 \quad (4)$$

Substitution $$H_2O_2 + RX \rightarrow HX + ROOH \quad (5)$$

As oxidant, H_2O_2 differentiates from stoichiometric oxidants like nitrous oxide (N_2O), tert-butyl hydroperoxide (tBuOOH) or permanganates that produce wastes in large amounts, and make mandatory the implementation of additional separation steps. H_2O_2 also benefits from its low molecular weight, and in consequence from its high active oxygen content, in comparison to other popular oxidants such HNO_3 or NaClO (Table 1) [1].

Table 1. Classical industrial oxidants. Reproduced with permission from Ref. [1]. Copyright 2006 Wiley-VCH Verlag GmBH.

Oxidant	**By-product**	**Active oxygen (% w/w)**
H_2O_2	H_2O	47.1
N_2O	N_2	36.4
NaClO	NaCl	35.6
$NaIO_4$	NaI	29.9 [b]
HNO_3	NO_x, N_2O, N_2	25.0
NaClO	NaCl	21.6
tBuOOH	tBuOH	17.8
NaBrO	NaBr	13.4
« $KHSO_5$ »[a]	$KHSO_4$	10.5 -

[a] stabilized and marketed as the “triple salt” 2 $KHSO_5$ • $KHSO_4$ • K_2SO_4 (oxone), [b] considering that all four oxygen atoms are used.

1.2. Applications of hydrogen peroxide

Figure 1 depicts the main fields of applications of H_2O_2. Pulp and paper bleaching is one of the most important applications of H_2O_2, that is used as an alternative to classical chlorine-

based bleaches and allows the release of halogenated byproducts in wastewater to be hindered. In alkaline media, H_2O_2 operates as a bleaching agent through the presence of the HO_2^- anion, as it can eliminate many chromophores from the lignin polymer, notably by its nucleophilic attack on the carbonyl functions of the lignin. H_2O_2 is also used as a bleach for the recycled paper, where the printing dyes are removed by a combined action of H_2O_2 and of sodium dithionite used as reductive bleach.

H_2O_2 is also extensively used as a bleaching alternative to sodium hydrosulfite or hypochlorite in the textile industry, which requires the implementation of color-safe laundry bleaches. For this application, stable precursors like sodium perborate or percarbonate are used. They release H_2O_2 during dissolution in water, percarbonates being preferred to perborates owing to a lower dissolution temperature.

Driven by more and more stringent environmental regulations, wastewater treatment is the most significant application of H_2O_2 in the environmental field. It can supersede chlorine-based oxidants for the destruction of toxic chemicals such as thiocyanate, cyanide, chloride, hypochlorite, nitrite, cyanide or organic compounds in industrial wastewater, or hydrogen sulfide in the sewer pipes of municipal wastewater treatment networks [2]. One major advantage of H_2O_2 is the absence of halogenated by-products such as the carcinogenic trihalomethanes that require the downstream implementation of granular adsorbents.

Chemical synthesis is also a driving force for the H_2O_2 demand, with applications in the ammoximation of cyclohexanone to the corresponding oxime that is a key-intermediate in the Nylon-6 production [3], as well as in the HPPO (hydrogen peroxide propylene oxide) process, that integrates a unit generating H_2O_2 by direct reaction of H_2 and O_2 for a more efficient propylene oxide production [4-6]. Other reactions consist notably in alkene epoxidation, aromatic hydroxylation, alkane oxidation or oxo-halogenation reactions.

Last, H_2O_2 is used in several niche applications such as the mining and metal processing [7-8], with applications like the extraction and post-treatment of uranium and of many transition metals, but also metal finishing. H_2O_2 is further used for cleaning wafers of silicon and germanium semiconductors and etching printed circuit boards.

Figure 1. Main fields of applications of hydrogen peroxide. Adapted and reproduced with permission from Ref. [9]. Copyright 2019 American Chemical Society.

The annual world production of H_2O_2 demand was approximately 5.1 million metric tons in 2021. The sectoral distribution of the H_2O_2 demand depends clearly on the geographical location, but the paper and pulp bleaching is by far the dominating sector irrespectively of the

location, followed by decreasing order of importance, first by the chemical synthesis and the textile bleaching, and further among other sectors, by cosmetics and healthcare, wastewater treatment, food and beverage, electronics and semiconductors.

1.3. Key highlights into the global hydrogen peroxide market

Estimates are obviously subjected to variability depending on the projection models used, on intrinsic factors lying to the H_2O_2 market and on external regional and world conjunctural factors. The global hydrogen peroxide market is expected to reach a revenue of US$6.6 bn in 2026, compared to its 2020 level of US$3.9 bn, and is estimated to exhibit a compounded annual growth rate (CAGR) of 7.3% between 2022 and 2026, with a 1.9 fold expansion [10]. High-purity grades are projected to remain the most sought-after grades for the different end-users, and the 35-70% grade should amount for over 74% share in the market volume. Remarkable contribution to the market growth will likely result from the growth of specialty application areas like electronics and semiconductor manufacturing (expected to be the fastest-developing end-user), food and beverage, cosmetics, water treatment, and aquaculture, due to the growing environmental awareness and to the soaring availability of sustainable alternatives. This growing demand for high-purity H_2O_2 should provide new lucrative opportunities for key-manufacturers, and the main end-users that need high-purity H_2O_2 will form newer niche markets for H_2O_2 suppliers.

Asia Pacific is projected to keep its leadership in the market by contributing to over half of the revenues, while China should spearhead as the larger consumer and producer. However, the Middle East and Africa are all set to emerge as the most lucrative regional market for H_2O_2. The market is dominated by European players, and the top-five key-actors (namely Solvay S.A., Arkema S.A., Evonik Industries AG, Mitsubishi Gas Chemical Company and

Nouryon Holding B.V.) accounted in 2021 for a collective share of over 75% in the global hydrogen peroxide market space.

2. Synthesis routes of H_2O_2

2.1. An historical perspective of the industrial H_2O_2 manufacture

The first isolation of the H_2O_2 synthesis takes us back to the original works of L.J. Thenard in 1818 reporting that H_2O_2 is obtained as a byproduct of the reaction between barium peroxide and acids [11]. Table 2 lists the chronological developments achieved in the field of the industrial production of H_2O_2, itemized as chemical and electrochemical processes [12]. Reaction schemes and descriptions can be found in Jones [13], Goor et al. [14-15] and Ranganathan and Sieber [12].

Table 2. Historical development in the industrial manufacture of H_2O_2. Reproduced with permission from Ref. [12]. Copyright 2018 MDPI.

Year	Inventor	Catalysis type	Details
1818	L.J. Thenard	Chemical	Barium peroxide reacts with nitric acid and forms H_2O_2 as a by-product. Barium peroxide reacts with hydrochloric acid to form barium chloride and H_2O_2. Yield of 3% H_2O_2 was 2000 tons/annum (t/a) [11, 16]
1853	H. Meidinger	Electrochemical	Electrolysis of sulphuric acid to yield H_2O_2 [17]
1878	M. Berthelot	Electrochemical	Elucidated the mechanism of sulphuric acid electrolysis. Reported the formation of peroxodisulphuric acid as an intermediate [18]
1901	W. Manchot	Chemical	Autoxidation of hydroquinones and hydrazobenezenes under alkaline

			conditions in the presence of molecular oxygen to yield H_2O_2 [19-21]
1908	Degussa-Weissenstein Process	Electrochemical	First production plant set up in Weissenstein, Austria [22-23]
1910	Münchner Process or the Pietzsch-Adolph Process	Electrochemical	Developed by Pietzsch and Adolph at the Elektrochemische Werke, Munich. Used potassium peroxodisulphate instead of sulphuric acid to produce H_2O_2 [22-23]
1914	Hugo Henkel and Walter Weber	Chemical	First account of direct synthesis of H_2O_2 using its constituent gases [24]
1924	Riedl-Löwenstein Process	Electrochemical	Similar to the Pietzsch-Adolph Process; used ammonium peroxodisulphate to produce H_2O_2 by electrolysis. Yield of 100% H_2O_2 was 35 kt [22-23]
1932	Walton and Filson	Chemical autoxidation	Published their work on the alternate oxidation and reduction of hydrazobenzenes to produce H_2O_2 [25]
1935	Pfleiderer, Baden, Aniline and Soda Factory (BASF)	Chemical autoxidation	Alkaline autoxidation of hydrazobenzenes to form sodium peroxide, later hydrolysed to form H_2O_2 [26]
1935–1945	Riedl and Pfleiderer	Chemical autoxidation	Anthraquinone autoxidation process (AO) set up in two different cities each with 2000 t capacity [22, 27]
1953	E.I. du Pont de Nemours	Chemical autoxidation	Commercial plant setup with based on the Riedl and Pfleiderer process [13-15]
1957–1980	Shell process	Chemical autoxidation	Oxidation of 2-propanol to yield H_2O_2 at a capacity of 15 kt [28]

2.2. The anthraquinone process

The production of H_2O_2 is currently realized at the industrial scale via electrolysis, partial oxidation of isopropanol, and mainly through the anthraquinone (AQ) autoxidation process, that accounts for more than 95% of the worldwide production of H_2O_2 [1]. The first commercial development of the AQ autoxidation process with a production level of 1 ton/year was implemented in Germany by IG-Farbenindustrie AG following the so-called Riedl-Pfleiderer process pioneered at BASF in 1939 [27]. Although the original process has been improved, it is still based on a multi-step sequence consisting in hydrogenation, oxidation,

H_2O_2 extraction and treatment of the working solution. A simplified block diagram of the multi-step AQ autoxidation process is shown in Figure 2A.

2-alkylanthraquinone (AQ), mostly 2-ethyl anthraquinone, is first hydrogenated into the corresponding anthrahydroquinone (AHQ) over a Pd or Ni catalyst in an organic solvent (Figure 2B). After separation of the catalyst from the solution, AHQ is oxidized back into AQ with the equimolar formation of H_2O_2. H_2O_2 is recovered from the working organic solution by liquid-liquid countercurrent extraction with demineralized water. Further distillation allows for the purification of the aqueous H_2O_2 and the increase of its concentration up to *ca*. 70% while the AQ-containing solvent is recycled. In both hydrogenation and oxidation steps, side reactions such as the hydrogenation of the unsubstituted aromatic ring in AHQ to form 5,6,7,8-tetrahydroanthrahydroquinone (THAHQ), and its further oxidation into tetra hydroquinone (THAQ), are lowering the yields to H_2O_2 and result in a net consumption of AQ.

The great advantage of the AQ process remains the capacity to operate and to produce H_2O_2 in a continuous way at relatively mild temperature, and without any contact between H_2 and O_2. However, mass transfer limitations in both oxidation and hydrogenation reactors are lowering the performances, and the difficult control of both AQ residence time and AQ/H_2 ratio in the hydrogenation reactor favors the formation of byproducts. Cross-contamination between phases is observed, while organic contamination can also be introduced during the extraction step. Therefore, in addition to a significant energy input, the AQ process suffers globally from the generation of wastes in large amounts, namely wastewater containing *e.g*. 2-ethylanthraquinone, tri-octyl phosphate, tert-butyl urea or potassium carbonate, solid wastes (activated alumina) or exhaust gases (mesitylene isomers) [29].

Despite its relatively high E-factor (defined as the ratio between the amount of waste generated and that of the desired product) and its low atom efficiency, the AQ oxidation

process remains *de facto* the process operated at the industrial scale, as it is reported to be economically viable for yearly production volumes above 10^5 tons at H_2O_2 high concentrations.

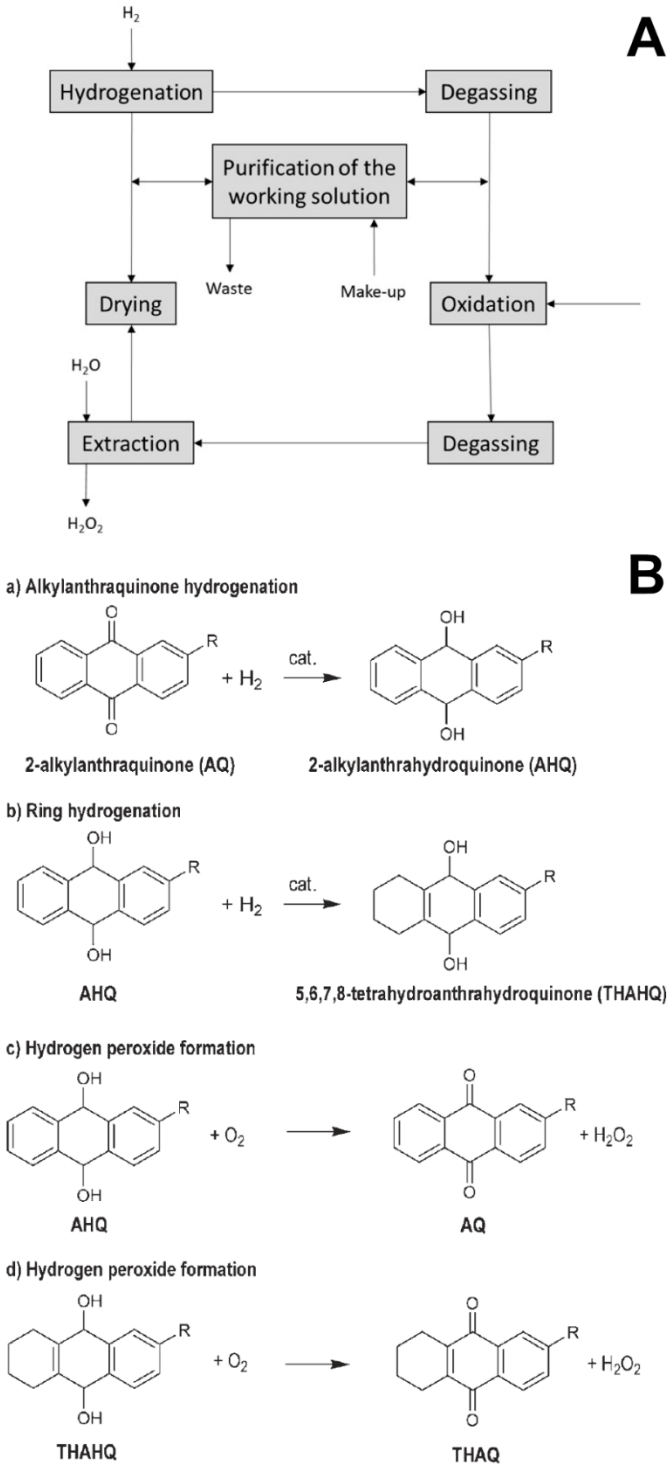

Figure 2. (A) Simplified block diagram of the multi-step AQ autoxidation process. Reproduced with permission from Ref. [12]. Copyright 2018 MDPI; **(B)** AQ autoxidation reaction process. Reproduced with permission from Ref. [1]. Copyright 2006 Wiley-VCH Verlag GmBH.

2.3. Industrial competitors to the anthraquinone process

As shown in Figure 3, H_2O_2 can be alternatively produced by the partial oxidation of primary or secondary alcohols, with the formation of aldehyde or ketone, respectively, as byproduct [30-31]. This process was implemented by Shell Chemical over the period 1957-1980, and relies on the autoxidation by an oxygen-rich gaseous stream of the 2-propanol reagent in an azeotrope mixture with water at moderate pressure and temperature (10-20 bar, 90-140°C).

The synthesis of H_2O_2 through the oxidation of methylbenzylalcohol was developed separately by Repsol Quimica and Lyondell Chemical (Arco Chemical). At 120-180°C and under pressures of 3-10 bar, the production of methylbenzylalcohol and of H_2O_2 as byproduct can occur without the help of any catalyst [32-33], although Ni-based complexes can be used as homogeneous catalysts [34].

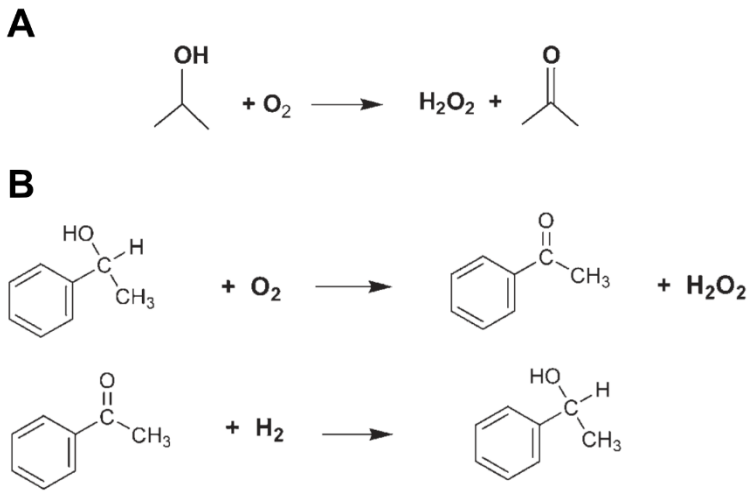

Figure 3. Large scale processes alternative to the main AQ oxidation, based on the oxidation of alcohols. **(A)** Autoxidation of a secondary alcohol; **(B)** oxidation of methylbenzylalcohol, with the subsequent recycling of the acetophenone into methylbenzylalcohol after the extraction/distillation step. Methylbenzylalcohol is a byproduct of the propylene-oxide-styrene process. Reproduced with permission from Ref. [1]. Copyright 2006 Wiley-VCH Verlag GmBH.

Last, the Dow process consists in conducting the electrochemical synthesis of H_2O_2 in a diluted solution of NaOH, with the following half and overall reactions (6-8). This technology can mostly be used when the application does not require the separation of H_2O_2 from the NaOH aqueous solution (*e.g.* pulp bleaching).

Anode $$2\,OH^- \rightarrow H_2O + \frac{1}{2}O_2 + 2\,e^- \quad (6)$$

Cathode $$H_2O + O_2 + 2\,e^- \rightarrow HO_2^- + OH^- \quad (7)$$

Full reaction $$NaOH + \frac{1}{2}O_2 \rightarrow HO_2Na \quad (8)$$

2.4. Direct synthesis of H_2O_2 from molecular O_2 and H_2

The direct synthesis of H_2O_2 from molecular O_2 and H_2 reactants appears as a greener and more atom-efficient route than the dominant, energy-intensive and low-sustainability industrial AQ process. Being in principle the simplest method, it might offer a valuable alternative in particular for decentralized production. Apart from the safety concerns related to the management of H_2/O_2 mixtures known as explosive over a wide range of

concentrations, the main challenge of the process lies in selectivity issues, given that the formation of H_2O from molecular O_2 and H_2 (10) is thermodynamically more favorable than that of H_2O_2 (9). In addition, the process selectivity is also affected by both H_2O_2 decomposition (11) and hydrogenation (12), which lead to the unwanted formation of H_2O.

$$H_2\,(g) + O_2\,(g) \rightarrow H_2O_2\,(l) \qquad \Delta G^0_{298K} = -120.5\ kJ/mol$$
$$\Delta H = -135.8\ kJ/mol \qquad (9)$$

$$H_2\,(g) + \tfrac{1}{2}O_2\,(g) \rightarrow H_2O\,(l) \qquad \Delta G^0_{298K} = -237.2\ kJ/mol$$
$$\Delta H = -241.6\ kJ/mol \qquad (10)$$

$$H_2O_2\,(l) \rightarrow 2\,H_2O\,(l) + \tfrac{1}{2}O_2\,(g) \qquad \Delta G^0_{298K} = -116.7\ kJ/mol$$
$$\Delta H = -105.8\ kJ/mol \qquad (11)$$

$$H_2O_2\,(l) + H_2\,(g) \rightarrow 2\,H_2O\,(l) \qquad \Delta G^0_{298K} = -354\ kJ/mol$$
$$\Delta H = -211.5\ kJ/mol \qquad (12)$$

Pd catalysts are known to be very active for the direct synthesis of H_2O_2 from molecular O_2 and H_2 since more than a century [24]. However, a proper and careful balance has to be found between activity and selectivity. Also, the degradation of H_2O_2 needs a clear and strict control of the experimental conditions for being minimized, in particular by using a low temperature of reaction.

It is proposed that the synthesis of H_2O_2 occurs by addition of hydrogen to the O_2* surface intermediate, and that the irreversible O-O cleavage in molecular O_2 leads to the formation of H_2O and prevents that of H_2O_2 [35-36]. A clear challenge relies on the ability of finely-tuned catalysts to unfavor the formation of both O* and OH* surface intermediates, known to lead to the formation of the unwanted H_2O molecule [37].

Pd-based catalysts are reported to be highly active for the direct synthesis of H_2O_2. However the evidence whether metallic or oxidized Pd phases are needed, still remains a matter of debate, as well as the nature of the Pd active site favoring the irreversible cleavage of the O-O with consequent formation of H_2O [38]. The use of additives, either as promotor to the catalyst itself or to the reaction media, was reported as a worthy strategy for enhancing the selectivity, and in particular for inhibiting the reaction pathways leading to the H_2O_2 degradation. They comprise mostly inorganic acids such as sulfuric or phosphoric acids, or halogen acids such as hydrochloric acid [39]. Solid acids as well as halides have also been used as additives to the catalyst. Wilson and Flaherty interestingly highlighted the crucial role of the protons in the formation of H_2O_2, in particular by aiding the key-reduction of O_2, while they suggested that the counteranions can play an important role towards the H_2O_2 selectivity [40].

While intensive works have been conducted on Pd systems, Au catalysts dispersed on a large range of supports were more recently reported to be promising for synthesizing H_2O_2 without addition of any halide promoters [41-42]. A wide range of noble (Pt, Ru, Au, Ir, Ag) and non-noble (Co, In, Ga, Zn, Ni, Sn, W, Sb, Te) secondary metals has been investigated, the use of cost-effective, abundant metals being of prime importance. Huge works remain to be performed to unravel the synergistic effect observed with finely-tuned bimetallic systems, that will require the association of both experimental and computational tools.

Further, as usually in heterogeneous catalysis, the support nature is a key-factor strongly impacting on the activity of the metal-based catalysts and on the selectivity pattern of the reaction. Among others, most of the supports studied comprise many transition metal oxides, mesoporous silica, zeolites, heteropolyacids or carbons under various forms [38].

An approach for preventing the detrimental decomposition of H_2O_2 into H_2O and O_2 lies in the use of a suited solvent, which strongly complexifies the process, in particular owing to mass transfer barrier limitations between the solvent and the gas phase. The solvent acts for enhancing the hydrogen solubility in the liquid phase but also can play additional roles. For instance, acetonitrile and ethanol were reported to inhibit the formation of H_2O by coordinating with the Pd surface [43]. Water as solvent provides the largest safety to the process, also with very good miscibility with H_2O_2. Unfortunately, it shows a low solubility with both O_2 and H_2, which in consequence lowers the production of H_2O_2. Organic solvents can be used, but they are usually introducing problems of contamination for the aqueous phase. CO_2 can be used as solvent in both supercritical and liquid phase conditions, the miscibility of H_2 and O_2 being by far higher than in aqueous or organic solvents. Nevertheless, mass transfer limitations between both liquid and gas phases are in favor of operating in supercritical conditions.

Additionally, membranes can be used as an elegant strategy to avoid the direct contact between molecular H_2 and O_2 [44]. They can in particular be used for supplying atomic hydrogen to the catalyst located in the porous network where it can interact with oxygen.

3. Experimental methodology for the quantification of H_2O_2 in water

The measurement of the H_2O_2 concentration is an indispensable first step to evaluate the catalyst performance, selectivity, and stability and, ultimately, to get the most suitable reaction conditions for developing new two-electron water oxidation reaction and two-electron oxygen reduction reaction (ORR) photo-, electro-, or photoelectro-catalysts able to pave for a more sustainable path in the synthesis of H_2O_2. Thus, analytic methods such as UV-

Vis spectroscopy [45], chemical titration [46], fluorometry [47], chemiluminescence [48], and colorimetric test strips [49] have been used to accurately quantify H_2O_2. Each method offers a unique advantage depending on the nature of the solvent or electrolyte, the accuracy requirement, or the concentration of *in-situ* produced H_2O_2. Although these methods are generally well established, accurate quantification sometimes poses a challenge since the complexity of the detection environments further complicates the H_2O_2 measurement. Here, we will briefly discuss the working principle, the pros and cons of each method, and the interferences that may affect the measurements.

3.1. Methods for H_2O_2 quantification

Among the different methods, the use of colorimetric test strips is the most convenient and straightforward means to estimate the unknown amounts of H_2O_2. When the strip is immersed in the sample solution, H_2O_2 reacts with the peroxidase and the organic redox indicator, forming a colored oxidation compound (Figure 4A) [50]. By visually comparing the strip with the fields of the color scale, the H_2O_2 concentration can be measured semi-quantitatively. Depending on the manufacturer, the paper strips can detect H_2O_2 within the concentration range of 0.5 ppm to 1000 ppm with an accuracy of ± 20% (Quantofix®). However, factors such as exposure time, compatibility with different solvents, electrolytes, and pH generally affect the precision of the test strips. For instance, the difference in air exposure time by 5 seconds before reading in a strip reader leads to an overestimated concentration of ~50% using 100 ppm test strips [51].

Methods such as spectrophotometry [45], chemical titration [52], and fluorimetry [47] are widely employed for more reliable quantification. In many reports, the concentration of H_2O_2 generated photocatalytically is in the micromolar and millimolar range after a few hours.

Therefore, the detection method must be sensitive and with a low detection limit. The most traditional measurement method is by permanganate ($KMnO_4$) titration (Figure 4B) [52]. It is based on the reduction of MnO_4^- by H_2O_2 to produce colorless Mn^{+2} ($MnSO_4$) under acidic conditions (13). A change in the color of H_2O_2 to faint pink indicates the reaction's endpoint. Based on the amount of $KMnO_4$ consumed during titration, and the reaction stoichiometry, the amount of H_2O_2 can be calculated. Although the strongest advantage of the $KMnO_4$ titration method is its accuracy, the limit of detection is high (200-1000 ppm), so it is only useful for medium to high H_2O_2 concentrations, and a large sample volume is usually necessary [52-53].

$$6H^+ + 2M_nO_4^- + 5H_2O_2 \rightarrow 2Mn^{2+} + 8H_2O + 5O_2 \quad (13)$$

In contrast to the permanganate method, the iodometric titration method utilizes the oxidizing properties of H_2O_2. With this method, H_2O_2 oxidizes I^- (coming from KI) to form triiodide (I_3^-) (14), then titrated with thiosulfate (15). Titration with thiosulfate results in a pale yellow-colored solution turning to deep blue with the addition of starch as the indicator [54].

$$H_2O_2 + 2KI + H_2SO_4 \leftrightarrow I_2 + K_2SO_4 + 2H_2O \quad (14)$$

$$I_2 + 2Na_2S_2O_3 \leftrightarrow Na_2S_4O_6 + 2NaI \quad (15)$$

Overall, the titrimetric method's advantage compared to any other method is that it does not require the determination of a calibration curve or the use of any specific equipment before analysis, however, the concentration of H_2O_2 being measured should be taken into consideration due to the high detection limit of quantification of this method.

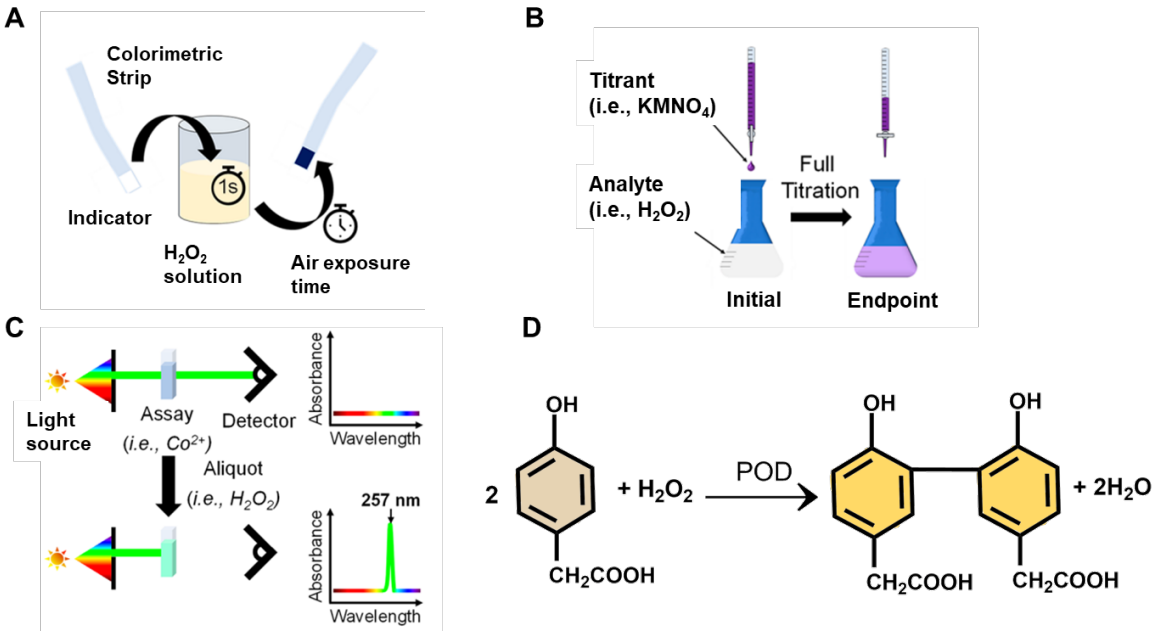

Figure 4. Schematic representation of different H_2O_2 quantification methods. **A)** Colorimetric test strips, **B)** titration by $KMnO_4$, **C)** UV-Vis spectroscopy, **D)** POHPAA fluorescence method. Reproduced with permission from [51]. Copyright 2020 American Chemical Society.

Direct detection of H_2O_2 in solution through optical absorption is possible, although it is challenging for low concentrations since its absorption coefficient is small (0.01 M^{-1} cm^{-1} at 360 nm and 13 M^{-1} cm^{-1} at 260 nm) [55]. Also, this method may have many interferences and should be only recommended in controlled reaction media. Therefore, colorimetric method is the most widely adopted for H_2O_2 detection of low concentration. Here, H_2O_2 can reduce or oxidize a reagent resulting in a color change, and measured using a UV-Vis spectrophotometer (Figure 4C). The absorption is usually proportional to the amount of H_2O_2, which can be accurately quantified by constructing a calibration curve. One example is the N, N-diethyl-p-phenylenediamine (DPD) method, which is based on the oxidation N, N- DPD by H_2O_2 catalyzed with peroxidase (POD).

The radical DPD^+ exhibits a stable pink color with strong absorption at 551 nm and 510 nm with a large absorption coefficient of 2.1 x 10^4 M^{-1} cm^{-1} [56] where the intensity at 551 nm can be directly correlated with the amount of H_2O_2. This method is linear for a concentration range of 0-100 µM. Therefore, with this method, dilution is always necessary for samples with high H_2O_2 concentration [57]. Parallel to DPD, the iodometric method using potassium iodide (KI) relies on the oxidation of excess I^- by H_2O_2 to produce a yellow-colored I_3^-, which can be observed at 350 nm (16).

$$H_2O_2 + 2I^- + 2H^+ \rightarrow I_2 + 2H_2O \quad (16)$$

$$I_2 + I^- \leftrightarrow I_3^- \quad (17)$$

This procedure is similar to iodometric titration, except the iodine is not titrated with thiosulfate, and the I_3^-, which is in equilibrium with I_2 and I^- is being measured. Since the reaction with KI and H_2O_2 is slow, a small amount of ammonium molybdate is usually added as a catalyst and potassium hydrogen phthalate (KHP) as the buffer [58]. The large value of molar absorption coefficient of I_3^- (2.6 x 10^4 M^{-1} cm^{-1}, λ = 350 nm) makes it very suitable to measure even at less than 10 µM H_2O_2 (17). Compared to $KMnO_4$ titration, the KI method is less sensitive in the presence of organic impurities [52]. Other colorimetric methods are also reported:

- Oxidation of Fe^{+2} to Fe^{+3} [59].
- Cerium sulfate method, where H_2O_2 reduces yellow-colored Ce^{4+} to Ce^{3+}, and is measured by the decrease in absorbance of Ce^{4+} at 316 nm [49].
- Cobalt-carbonate assay (Co/CO_3), which forms a greenish ($[Co(CO_3)_3]Co$) complex after Co^{2+} oxidation, where the formed complex can be measured at 260 nm [51].

- Reduction of vanadate (VO_3^-) under acidic conditions to produce a red-orange peroxo-vanadium cation (λ = 450 nm) [60].
- Reduction of Cu^{+2} by H_2O_2 in the presence of excess 2,9-dimethyl-1,10-phenanthroline (DMP) to form Cu^{+1}-DMP (λ = 454 nm) [61].
- Reaction of titanium sulfate reagent with H_2O_2 to produce a yellow-colored complex of pertitanic acid (H_2TiO_4), which absorbs at 410 nm [62].
- H_2O_2 oxidation of oxo [5,10,15,20-tetra(4-pyridyl)porphyrinato] titanium(IV) ($TiO(tpypH_4)^{+4}$) to $TiO_2(tpypH_4)^{+4}$ (λ=450 nm) [63].

The minimum detection limits for these methods range from 0.01-50 ppm, significantly lower than the titrimetric method [64]. Despite the numerous techniques mentioned here, new analytical methods are being developed to achieve a more robust, cheaper, and accurate H_2O_2 quantification. For instance, the presence of dyes in water, such as rhodamine B and acid orange 7, causes the same absorption with DPD^+ at 551 nm, leading to increased measured absorbance leading to inaccurate H_2O_2 measurements. To improve the traditional DPD-POD method, the POD-KI method was recently established to improve the measurement in the presence of dyes. Moreover, it shows high tolerance to counter ions such as Cl^-, NO_3^-, SO_4^-, and humic acids [65]. The accuracy of the measurement using the spectrophotometric method hugely relies on the accuracy of the known H_2O_2 concentration of the standards. If done correctly, spectrophotometric methods are preferable to titration-based techniques due to their simplicity, low detection limits, low execution cost, and being completely quantitative.

The fluorometric method is also used to quantify H_2O_2 accurately. This method relies on the horseradish peroxidase (HRP)-catalyzed dimerization of p-hydroxyphenyl acetic acid (POHPAA) by H_2O_2 (Figure 4D). As proposed by Miller & Kester [66], H_2O_2 oxidizes the

peroxidases from the +3 to +5 state. Subsequently, the oxidized peroxidase is reduced by the POHPAA to form POHPAA radicals through two related pathways. The two POHPAA radicals will form the fluorescent product, 2,2'-dihydroxybiphenyl, with excitation and emission wavelengths peaking at 320 nm and 400 nm, respectively. The formation of the dimer directly correlates to the concentration of H_2O_2 with the detection limit of 0.2 μg L^{-1} [67]. This assay is very sensitive towards impurities in the reagent POHPAA, so it should be freshly recrystallized before use. Table 3 provides more information about the analytical methods discussed above, as reviewed previously by Brandhuber & Korshin [64].

Table 3. Different analytical methods for H_2O_2 quantification. Reprinted with permission from Ref. [64]. Copyright The Water Research Foundation.

Type	Method	H_2O_2 range	Reaction mechanism and detection conditions	Performance assessment/interference
Titration	Iodometric	0.1-6 wt%	Oxidize iodide to iodine, titrated with thiosulfate and starch.	Not accurate at low concentration; subject to interference.
	Permanganate	0.25-70 wt%	Reduce permanganate to manganous ion.	Not accurate at low concentration.
	Ceric sulfate	1-13 wt%	With a ferroin indicator, titrate to a pale blue.	Not accurate at low concentration.
Spectrophotometry	Cobalt carbonate	up to 0.1 mg/L	Formation of a UV-absorbing complex between Co^{+3} and carbonate, detection at 260 nm.	Reducing and complexing agents; combined and free chlorine effects not known.
	Iodometric	0.05-10 mg/L	Oxidize iodide to iodine with molybdate catalyst at pH 5; detection at 351 nm.	Evidence of interference from oxidants; transition metals.
	Titanium oxalate	0.1-50 mg/L	In the presence of sulfuric acid, formation of colored peroxotitanium complex; detection at 400 nm.	Some UV absorbing species, turbidity, color; combined and free chlorine effects not known.
	Peroxidase enzyme-leuco crystal	0.1-10 mg/L	Oxidation of leuco-crystal violet dye by H_2O_2 in presence of peroxidase enzyme catalyst; detection at 551 nm.	Usually interference-free; slow color development; sensitive to sunlight; combined and free chlorine effects not known.

	Peroxidase enzyme-DPD	0.02-10 mg/L	Oxidation of DPD by H_2O_2in presence of peroxidase enzyme catalyst, detection at 551 nm.	Likely interference from combined and free chlorine, color unstable.
	Copper-DMP	0.03-10 mg/L	Reduction of Cu(II) and formation of copper-DMP complex, detection at 454 nm.	Reported to be effective in presence of chlorine stable color.
	Peroxovanadium	4-10 mg/L	Reduction of V(V) and formation of peroxovanadium cation; detection at 450 nm.	High detection limit; interference not known
Fluorescence	Peroxidase enzyme-POHPAA	> 1.0 x 10^{-3} mg/L	Peroxidase catalyzed oxidation of POHPAA by H_2O_2; fluoresces at 400 nm.	Known positive interference with chlorine.

3.2. Factors affecting H_2O_2 quantification

In a simple system, the accuracy of different H_2O_2 quantification methods is widely established. Indeed, each reported literature uses different methods because of the complexity of the catalytic reactions where the electrolytes, anions, and organic compounds acting as sacrificial agents can possibly interfere and may lead to overestimation and underestimation of H_2O_2 concentration. Recently, Zheng's group reported a systematic study of the effect of the complexation time, interferences such as the presence of alcohol, the pH, and the type of electrolytes on H_2O_2 quantification using different methods (*e.g.*, UV-Vis measurements using Co/CO_3 assay, titration with $KMnO_4$, Quantofix colorimetric test strips) [51]. For the detailed comparison of these effects, readers are directed to the reference [51].

In the photocatalytic process, organic compounds such as alcohols (*e.g.*, t-butanol, methanol, isopropanol) or organic acids (*e.g.*, oxalic acid, acetic acid, formic acid) are usually employed as electron donors or radical scavengers, which improves the rate of reaction. Overall, UV-Vis measurement is the most accurate method and less susceptible to species interference, contrary to the titration with $KMnO_4$. Hence, careful consideration must be implemented. In the presence of alcohol (such as ethanol or acetaldehyde), $KMnO_4$ titration overestimates H_2O_2 concentration [60]. For instance, the highest relative error of measurement was obtained when isopropanol was used, followed by ethanol and then methanol [51]. The overestimation in the presence of methanol is very important, especially at low H_2O_2 concentrations, as MnO_4^- is a strong oxidizing agent. Therefore, the MnO_4^- can easily oxidize the alcohol, increasing the consumption of MnO_4^- and leading to an overestimation of H_2O_2 concentration. In

contrast, iodometry, cerium sulfate, vanadate, and DPD methods are less affected by the presence of alcohol [60, 68].

Another parameter that impacts H_2O_2 quantification is the solution pH. The pH values of the solution or electrolyte play an essential role in the photo, electro, and photoelectro-catalytic processes, and many reports have shown the dependence of the H_2O_2 formation, including the selectivity and activity of H_2O_2 production on pH [69-70]. Changes in pH may interact with the reagents used in H_2O_2 measurements, which can introduce bias in the quantification. For instance, Zhang's group [51] has also shown that Co/CO_3 assay and $KMnO_4$ titration is fairly robust in the pH ranging from 0-14. On the other hand, the test strip obtained large deviations in the detected H_2O_2 at strongly acidic (pH 1) and alkaline solutions (pH 13), while a good reproducibility of the results was obtained over pH 2-12. Results imply that test strips can be a quick means to "semi-quantitatively" determine the H_2O_2 concentration, which can be followed by the UV-Vis or titration method for more accuracy.

Although the iodometry is less affected by the presence of alcohols [60, 68], the pH value is a critical issue for this method. In general, iodometry titration works well in slightly acidic solutions to prevent the dismutation of I_2 to I^- and IO_3^-, and avoid the dismutation of H_2O_2 to H_2O and O_2 at pH > 7. The optimal pH range identified for iodometry is pH 4.0 - 7.0 [65, 71]. In the presence of methanol, iodometric provides an underestimated amount of H_2O_2, especially at strongly acidic solutions (5 M H_2SO_4) and low H_2O_2 concentration (< 2 mM). Provided that H_2O_2 concentration is relatively high, iodometry and permanganate titration measurements in acidic alcoholic solutions are accurate [68].

Long and co-workers [60] studied the effect of organic compounds on the reliability of DPD, $KMnO_4$, and NH_4VO_3 methods. Organic compounds such as phenol, bisphenol-A, and *p*-benzoquinone can be easily oxidized by $KMnO_4$, increasing the measured H_2O_2 concentration. In the case of the DPD method, *p*-benzoquinone, rhodamine B, acid orange, and phenolic compounds can directly interact with DPD leading to an erroneous determination of H_2O_2, while NH_4VO_3 method is relatively accurate when < 1 mM benzoquinone is present [60].

Care should be taken when working in solutions with significant quantities of compounds which may form secondary peroxides from a reaction with H_2O_2. In particular, many acids are in equilibrium with their peracids in the presence of H_2O_2, resulting in the formation of compounds such as peracetic acid or peroxomonocarbonate. These are typically much more reactive than H_2O_2 itself and may therefore invoke a disproportionate response from the quantification methods [72]. These problems can be avoided by calibrating the method in a solution of exactly the same composition (buffer, additives) and allowing sufficient time for equilibration.

4. Photocatalytic synthesis of H_2O_2 from molecular O_2 and H_2O

4.1. Mechanism of peroxide formation

4.1.1. Oxygen reduction reaction mechanisms

Theoretically, H_2O_2 can be formed both reductively from molecular oxygen and oxidatively from water. By far the most studied of the two mechanisms is the reductive one. Generally, molecular oxygen can be reduced in a one-, two- or four-electron transfer mechanism. The primary product of the one-electron process (18) is the

superoxide anion radical ($O_2^{\bullet-}$) or, after protonation (19), a hydroperoxyl radical ($HO_2^{\bullet}$) [47]. These intermediates are usually further reduced to hydrogen peroxide in another one-electron transfer with subsequent protonation (20-21). Alternatively, the direct two-electron reduction mechanism leads directly from molecular oxygen to hydrogen peroxide (22).

Further reduction of the peroxide is also possible and eventually leads to water. On some very efficient oxygen reduction catalysts such as Platinum, the reduction of molecular oxygen may also directly proceed to water in a concerted four-electron reduction mechanism (23). However, in the context of H_2O_2 production and utilization, it is desirable to stop the reduction at the peroxide step and to avoid the pathway to water by over-reduction.

$$O_2 + e_{CB}^- \rightarrow O_2^{\bullet-} \quad (18)$$

$$O_2^{\bullet-} + H^+ \rightarrow HO_2^{\bullet} \quad (19)$$

$$HO_2^{\bullet} + e_{CB}^- \rightarrow HO_2^- \quad (20)$$

$$HO_2^- + H^+ \rightarrow H_2O_2 \quad (21)$$

$$O_2 + 2\ e_{CB}^- + 2\ H^+ \rightarrow H_2O_2 \quad (22)$$

$$O_2 + 4\ e_{CB}^- + 4\ H^+ \rightarrow 2\ H_2O \quad (23)$$

Studies on TiO_2 have shown that superoxide is formed with a similar rate as hydrogen peroxide, strongly indicating that the majority of peroxide is formed in consecutive one-electron transfers *via* superoxide/hydroperoxide radicals as intermediate [73]. This is not surprising as on un-modified photocatalysts, charge

carriers are strongly gated and only have limited local availability which impedes multi-electron transfers [74].

The one-electron reduction requires a significantly higher reduction potential (-0.05 V/RHE) than the two-electron reduction (+0.68 V/RHE) and is therefore not accessible by some single oxide photocatalytic materials such as WO_3 or Fe_2O_3. These are instead fully reliant on the direct two-electron transfer mechanism which may require the use of co-catalyst materials to promote this pathway. For example, it has been shown that grafting Cu(II) ions onto WO_3 dramatically improves its H_2O_2 generation rate while it only has a slight effect on TiO_2 [75]. Presumably, this is the case because contrary to WO_3, TiO_2 can already reduce O_2 through the one-electron pathway so unlocking the two-electron pathway with Cu(II) ion co-catalysts is not a game-changer.

Another possible strategy is to employ anthraquinones which are already well-known from the namesake AQ process for their excellent activity in forming H_2O_2 from O_2. Here, it is believed that the photocatalyst reduces AQ to its hydroquinone which then reacts with oxygen to form the peroxide. This strategy has been successfully applied to graphitic carbon nitride, where the addition of AQ carboxylic acid increased the H_2O_2 formation rate constant by more than 4-fold (see section 5.2.2) [76]. However, it should be noted that anthraquinones are photocatalysts themselves so it is difficult to only assign them co-catalytic properties [77].

Some photocatalysts such as graphitic carbon nitride also have an intrinsic catalytic activity for the two-electron pathway and are therefore very efficient for H_2O_2 production even without a co-catalyst [46]. The mechanism here is thought to proceed via a very fast formation of an 1,4-endoperoxide intermediate which suppresses the release of any possible superoxide intermediates (see section 5.2.2). Consequently,

Electron Paramagnetic Resonance (EPR) spectroscopy analysis yielded no detectable amounts of superoxide as intermediates [46].

If high reaction rates are achieved, *e.g.*, by employing powerful lamps in combination with efficient photocatalysts, it should be kept in mind that the oxygen availability in an aqueous reaction medium may present a limiting factor [78]. The solubility of oxygen in water is rather poor and even further reduced in the buffer systems (*e.g.*, phosphate or borate) which are popular for H_2O_2 generation [79]. A possible method to overcome this is to employ the photocatalyst directly on the gas-liquid interface, so the photocatalytic reaction may proceed on the three-phase-boundary akin to a gas-diffusion electrode [80].

4.1.2. Anodic H_2O_2 synthesis by water oxidation mechanism

In addition to the reductive process, hydrogen peroxide can also be formed by partial oxidation of water. This is a two-electron transfer process (25) which competes with both the one-electron oxidation to hydroxyl radicals (24) and the full four-electron oxidation to dioxygen (26). However, the former may also eventually lead to hydrogen peroxide formation *via* dimerization of hydroxyl radicals (27). Which one of these processes dominates is dependent on the relative binding energies of O* and OH* as surface species [81]. Among the more commonly studied materials, TiO_2, WO_3, SnO_2, $BiVO_4$ and MnO_2 lie within the range predicting hydrogen peroxide formation, as displayed in Figure 5 [81].

$$H_2O + h_{VB}^+ \rightarrow OH^\bullet + H^+ \quad (24)$$

$$2\,H_2O + 2\,h_{VB}^+ \rightarrow H_2O_2 + 2\,H^+ \quad (25)$$

$$2\,H_2O + 4\,h_{VB}^{+} \rightarrow O_2 + 4\,H^{+} \quad (26)$$

$$2\,OH^{\bullet} \rightarrow H_2O_2 \quad (27)$$

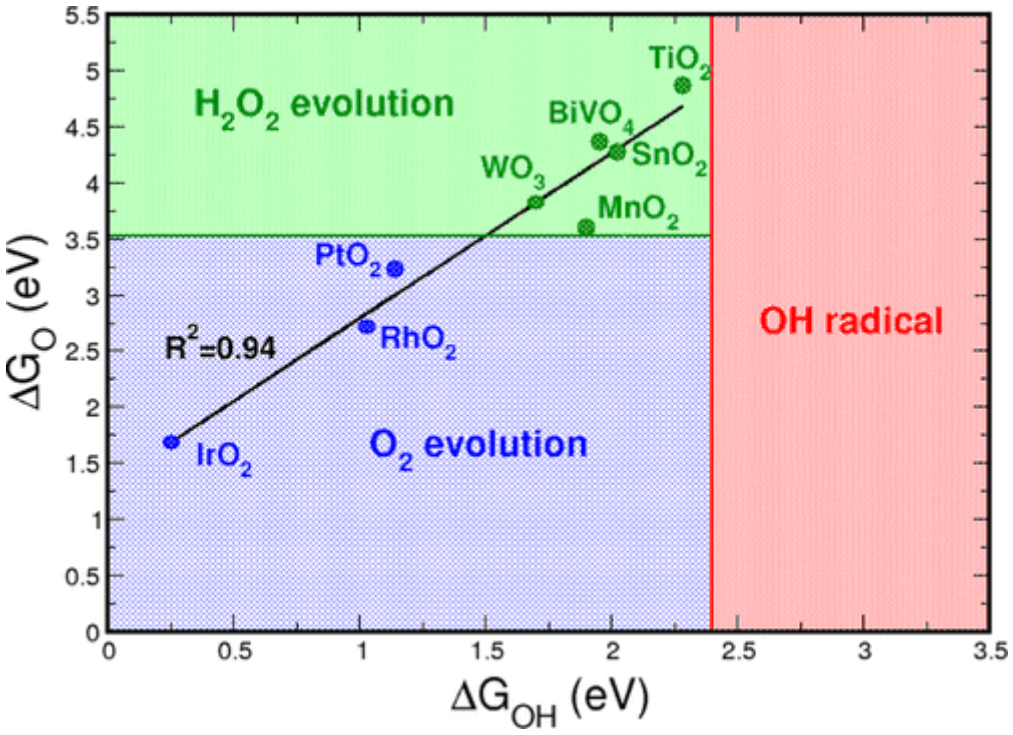

Figure 5. Phase diagram in terms of the binding energies of O* versus OH*. The black solid line displays the scaling line between O* and OH* surface species on different metal oxides. Blue, green, and red highlighted colors indicate regions in which O_2, H_2O_2, or OH radical are expected to be the major water oxidation product, respectively, in terms of purely thermodynamic constraints. Reproduced with permission from Ref. [81]. Copyright 2017 American Chemical Society.

The simultaneous production of peroxide from both the reductive and oxidative pathways opens up very efficient processes with potentially up to 200% efficiency. In photocatalytic experiments, it is difficult to investigate the oxidative H_2O_2 production

directly, as even in an oxygen-free medium, oxygen may be formed *in-situ* by water oxidation and subsequently reduced to H_2O_2. So, the observation of H_2O_2 formation alone is no definite proof for the direct oxidative pathway. However, this becomes possible in photo-electrochemical or electrochemical experiments where the half-reactions are spatially separated.

Using these techniques, experimental evidence for oxidative (anodic) H_2O_2 production has been reported for a variety of materials, most prominently TiO_2 [82], SnO_2 [82], WO_3 [83], $BiVO_4$ [83], ZnO [84] and $CaSnO_3$ [85]. Nørskov et al. showed that TiO_2, SnO_2, WO_3 and $BiVO_4$ were able to anodically generate H_2O_2 in sodium hydrogen carbonate electrolyte [86]. They observed that every metal oxide studied has its own optimal potential for the production of H_2O_2. For WO_3, a low potential of 2.25 *vs*. RHE is sufficient to generate H_2O_2 with a maximum faradaic efficiency (FE) of 47%. TiO_2, SnO_2 and $BiVO_4$, on the other hand, require a higher potential of over 3 V *vs.* RHE for optimal performance. $BiVO_4$ achieves an FE of 70% at 3.1 V *vs*. RHE, SnO_2 50% at 3.1 V and TiO_2 19% at 3.25 V *vs*. RHE [86]. It could also be shown that the required potential is significantly lowered when the electrodes are illuminated, indicating that this reaction can also be triggered under bias-free photo-electrochemical or photocatalytic conditions [86]. Generally, the efficiency appears to be higher in photo-electrochemical than in electrochemical systems [86], possibly due to the limited availability of holes which will impede the four-electron oxidation of water [74].

Even larger FE's have even been documented for ZnO and $CaSnO_3$. In aqueous 2M potassium hydrogen carbonate solution, ZnO (enriched in $(10\bar{1}0)$ facets) could achieve an FE of 81% at 2.6 V *vs.* RHE and $CaSnO_3$ at 3.2 V *vs*. RHE an FE of 76% [84-85]. In the last few years, the materials already mentioned have been further modified. $BiVO_4/WO_3$

was coated with a thin layer of Al_2O_3 in order to slow down the decomposition of H_2O_2 and thereby achieve higher concentrations and efficiency [87]. By doping $BiVO_4$ with gadolinium, a high stability and efficiency of the electrodes could be achieved [88]. In more recent works more promising materials were discovered. Porphyrins are able to oxidize water to hydrogen peroxide [89]. There is also work with PTFE-doped carbon [90], boron doped diamond [91] or other metal oxides such as $InSbO_x/CuSb_2O_x$ [92] or $LaAlO_3$ [93].

The reaction is reported to be strongly dependent on the electrolyte or buffer system [59]. The best results have been obtained using a 2 M $KHCO_3$ solution (pH 8.3) or even higher concentrated more alkaline carbonate systems [94-95]. Here, the working hypothesis is that in the concentrated bicarbonate solution, peroxomonocarbonate (HCO_4^-) is the primary oxidation product which is subsequently hydrolyzed to H_2O_2 [94, 96]. However, we note that there is an equilibrium between H_2O_2 and HCO_4^-, and in 2 M $KHCO_3$ there will be no complete hydrolysis, but also significant (stable) concentrations of the latter [72,97].

4.2. Kinetics of H_2O_2 formation (and degradation)

The first kinetic model for the photocatalytic formation and degradation of H_2O_2 was described by Kormann et al. in 1988 [98]. They studied the illumination of aqueous dispersions of ZnO, TiO_2 and a specifically prepared sample of desert sand from the Death Valley in presence of O_2 and organic electron donors. They described three possible pathways for the hydrogen peroxide formation:

- The first and most important one is the reduction of O_2 by conduction band electrons, whose yield can be enhanced by adding electron donors as sacrificial reagents for the valence band holes.
- The second pathway is the oxidation of water, which is only likely to occur in the absence of electron donors.
- The last pathway is the generation of H_2O_2 by secondary reactions of oxidized organic electron donors such as the dimerization and decomposition of methylperoxy- or α-peroxy-acetic acid radicals [99-100]. These reactions are important at high concentration of organic molecules and long illumination times.

If pathway 2 can be neglected [99] and pathway 3 is negligible in the initial phase, only the first pathway is relevant. With an excess concentration of electron donors and a constant oxygen concentration to accept conduction band electrons, the reaction order for the formation is zero. Equation (28) describes the formation rate r_F where ϕ_0 is the quantum yield of the formation and I_{abs} the absorbed photon flux, the product of which can also be termed as the formation rate constant k_F:

$$r_F = \phi_0 \cdot I_{abs} = k_F \qquad (28)$$

The degradation can occur to water by reduction and to oxygen by oxidation. Both processes are first order reactions when the H_2O_2 concentration is low. Eq. (29) describes the degradation rate r_D where ϕ_1 is the quantum yield and the k_D rate constant for the degradation:

$$r_D = \phi_1 \cdot [H_2O_2] \cdot I_{abs} = k_D \cdot [H_2O_2] \quad (29)$$

The combination of the formation and degradation results in a steady-state concentration of hydrogen peroxide during continuous irradiation. The overall concentration change of H_2O_2 is given by combining eqs. (28-29) into eq. (30):

$$\frac{d[H_2O_2]}{dt} = r_F - r_D = (k_F - k_D[H_2O_2]) \cdot I_{abs} \quad (30)$$

Integration of this rate law with $[H_2O_2] = [H_2O_2]_0$ at $t = 0$ leads to the explicit Eq. (31) which can be used to model the concentration-time profiles of photocatalytic H_2O_2 formation:

$$[H_2O_2] = \frac{k_F}{k_D}(1 - e^{-k_D t}) + [H_2O_2]_0 \cdot e^{-k_D t} \quad (31)$$

Under these conditions and assumptions, the steady-state concentration (at $t \to \infty$) of hydrogen peroxide $[H_2O_2]_{ss}$ should be independent of the photon-flux during the experiment (32).

$$[H_2O_2]_{ss} = \frac{k_F}{k_D} \quad (32)$$

Further illumination may lead to higher total peroxide concentration due to the formation of peroxides from organic radicals. These are formed during the oxidation of the organic hole scavengers if present [98]. Therefore, this simple model is only valid in

the initial phase if organic components are involved in the reaction. It also does not take into account many reaction parameters such as the catalyst loading and assumes a completely linear relationship between light intensity and reaction rate, which is usually not observed [47].

Understanding the influence of the light intensity in photocatalysis is particularly important. Many authors describe a linear increase in the reaction rate with the light intensity at low light intensities, while at higher light intensities a square root function can be assumed [101]. The nonlinearity is assumed to be a result of the increased charge carrier recombination. Others describe an exponential increase at high light intensities due to multiple electron transfers [102]. Burek et al. varied both the light intensity and the amount of TiO_2 over 4 orders of magnitude to fill gaps in the literature values [47]. As expected, the formation rate initially increased linearly, while a diminished response was observed at a higher light intensity. However, an increase in the catalyst concentration extended the range of the linear regime towards higher light intensities, revealing an interdependence of both parameters. The degradation rate of H_2O_2 is nearly constant over the complete investigated range of catalyst concentration and light intensity when 2-propanol is used as an electron donor. Therefore, contrary to the abovementioned model (30-32), the steady state concentration changes with the light intensity [47].

To account for this, a new holistic model for photocatalytic reactions was developed and applied to the case of the hydrogen peroxide formation [47, 103]. This new model is based on the three elementary reaction steps that are excitation, reaction and recombination, and employs a quasi-steady state approach. In certain geometries

featuring collimated unidirectional illumination, the integration of the resulting local rate law yields the explicit equation (33) for the overall observed reaction rate [47].

$$r_F = k_F = \frac{\beta}{\alpha} \cdot ln\left(\frac{\phi \cdot \alpha \cdot c_{pc} \cdot I_{avg}}{\beta \cdot c_{pc} + k_{recom}} + 1\right) \quad (33)$$

This equation has three reaction- and catalyst-specific parameters with direct physical meaning, namely the intrinsic quantum yield ϕ, the maximum reaction rate per catalyst mass β and the recombination rate constant k_{recom}. Additionally, the reactor geometry plays a role via the effective optical density α as well as the reaction parameters that are the catalyst concentration c_{pc} and the average incident photon flux I_{avg}. This rate equation was subsequently applied to the observed data points and the resulting plot is shown in Figure 6 [47].

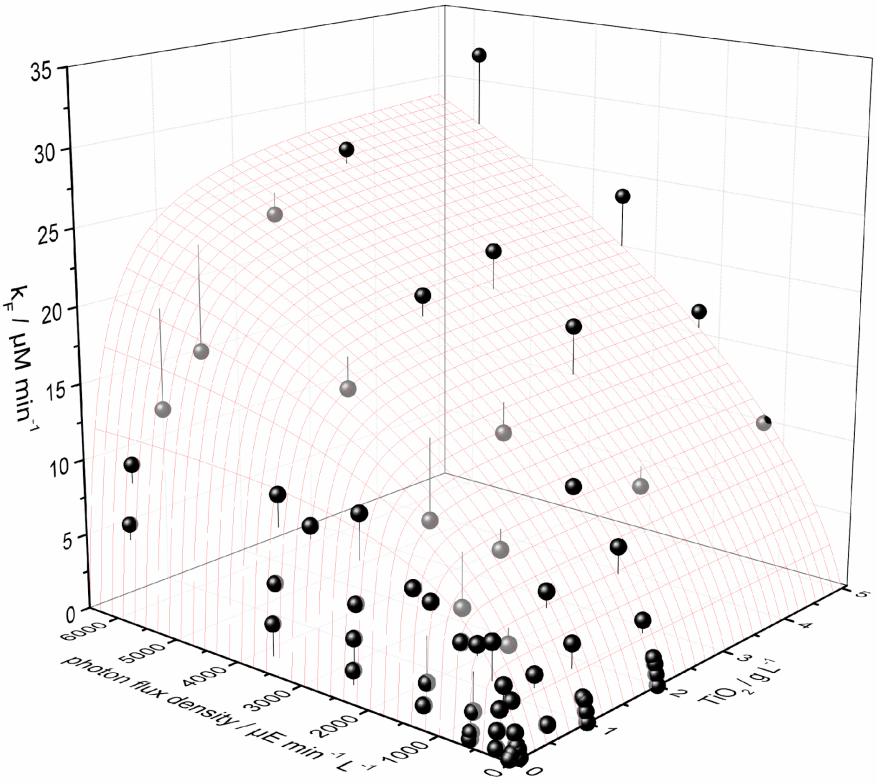

Figure 6. Interdependence of the amount of catalyst and the photon flux density shown as black and dark gray dots, on the measured H_2O_2 formation rate constant k_F. Also shown is the calculated best fit to the proposed model (32) as a surface plot. Reproduced with permission from Ref. [47]. Copyright 2019 American Chemical Society.

As can be seen from the data, the reaction rate initially increases linearly with the light intensity but shows a pronounced non-linear behavior at a higher light intensity, even leveling off completely to a plateau in case of low catalyst concentration [47]. This is a symptom of photon saturation, in this case the photocatalyst is unable to transfer the photo-generated charges to oxygen fast enough to make use of additional photons (kinetic limitation) [77, 103]. However, as it is apparent in Figure 6, this can partly be counteracted by employing a higher catalyst concentration. This both increases the

maximum attainable reaction rate and also shifts to higher light intensity the tipping point at which non-linear effects appear [47]. So essentially, efficiency losses at higher light intensity can be at least partially counteracted by employing higher catalyst concentrations. Tuning other reaction parameters (see section 4.3.) which increase the photocatalysts' surface kinetics has a similar effect [77].

Likewise, increasing the catalyst concentration initially increases the reaction rate, both by increasing the amount of absorbed light but also by increasing the overall available active sites. However, once a sufficiently-high concentration is reached, no further gain in reaction rate is observed upon further addition. Nonetheless, a high light intensity demands a higher catalyst concentration to reach the plateau because the amount of photogenerated charge carriers is higher and therefore needs more active sites [47, 77]. Another approach to alleviate kinetic bottlenecks is to improve the light distribution in the reactor, *i.e.*, reduce the degree of inhomogeneity, for example using delocalized internal illumination [104].

It should be noted that currently all kinetic models of the photocatalytic H_2O_2 production in particulate systems only account for the reductive formation *via* the reduction of molecular oxygen. The possible oxidative formation from water is usually deemed insignificant and neglected. This is because in particulate systems, there has not been any experimental evidence suggesting a significant contribution of this pathway in the studied materials. Also, the common use of sacrificial electron donors strongly suppresses the water oxidation reaction and thereby the oxidative H_2O_2 pathway. However, this assumption should be carefully revisited for materials and conditions which may more strongly favor this pathway (see section 4.1).

4.3. Influence of reaction conditions

In addition to the influence of both the light intensity and the catalyst concentration, numerous other parameters also influence the hydrogen peroxide formation rate. First of all, the employed electrolyte has a significant effect on both the formation and degradation rate of H_2O_2. The use of phosphate buffer as a solvent instead of water has the advantage of a higher formation rate and lower degradation rate due to the stabilization of H_2O_2 [105]. Moon et al. systematically investigated the effect of different electrolytes on the H_2O_2 formation rate over carbon nitride photocatalysts [106]. Generally, phosphate systems performed best, particularly those based on high fractions of KH_2PO_4. In a similar fashion to phosphate, bisulfate or bicarbonate electrolytes also showed beneficial effects, although not as pronounced. Among the cations, potassium salts showed higher formation rates than the sodium, lithium or ammonium variants.

Burek et al. investigated the influence of pH, oxygen partial pressure and temperature on the H_2O_2 formation over illuminated TiO_2 [47]. When the pH value of the phosphate buffer solution was varied between pH 2 and pH 10, the degradation rate increases exponentially between pH 2 and 9 and decreases slightly at higher pHs values [107]. H_2O_2 is stabilized in acidic phosphate solutions; in presence of hydroxyl ions, hydrogen peroxide disproportionates to H_2O and O_2. The formation rate, on the other hand, stays constant between pH 2 and 7 but increases exponentially above pH 8, emphasizing the critical role of hydroxyl ions also in the formation reaction. However, this may be different if a sacrificial electron donor such as an alcohol is employed [47].

The oxygen content in solution has also a significant effect as it is the required reagent. Due to its poor solubility in aqueous systems, limitation of oxygen availability

may already occur at mild reaction rates. It is therefore important to achieve a high oxygen transfer rate into the system, *e.g*., by using a sparger or by using pure oxygen gas instead of air. The effect of the oxygen partial pressure in the supplied gas was already observed in the early studies by Kormann et al. [98]. Up to 20 % oxygen content, the reaction rate increased before reaching saturation, indicating that the oxygen availability was no longer a limiting factor. However, in the study of Burek et al., 50 % oxygen partial pressure was necessary for reaching saturation, indicating that this is dependent on the mode of aeration and also the reaction rate [47]. When the formation rate is lower, a lower gradient between liquid and gas phase oxygen is needed to maintain saturation at the catalyst surface and thus less oxygen is required in the atmosphere. The same study also shows that the oxygen concentration can be accounted for in the proposed kinetic model, *e.g*., by integrating a Langmuirian adsorption term, and this fits well with the observed behavior [47]. Simple oxygen bubbling may not be enough at high light intensities to ensure oxygen saturation, as more oxygen is needed at high formation rates. Possible solutions include for example the use of a photocatalytic membrane, similar in function to a gas-diffusion electrode in electrochemistry [79].

Temperature is often treated as an insignificant parameter in photocatalysis as the majority of the energy for the reaction comes from the photons. However, in some cases, pronounced temperature effects are observed, particularly at high light intensity [47]. This is due to the fact that the increase in the rate of charge transfer on the photocatalysts' surface with increasing the temperature only translates into an observable reaction rate increase if the reaction is conducted in the kinetically-limited regime (and not in a photon-limited regime at low light intensity) [77]. An attempt to

determine the activation energy of the reaction (E_A) led to a value of 31.6 kJ mol^{-1} when using 2-propanol as a sacrificial electron donor [47]. However, the overall temperature effect is much more complex as it also affects other parameters such as the oxygen solubility and peroxide decomposition and can therefore have more complex interactions with the reaction rate.

The reaction kinetics are strongly influenced by the electron donor, *i.e.*, the corresponding oxidation reaction. While theoretically, water can fill this role and even increase the peroxide formation rate by concomitant oxidative production, it is a kinetically-demanding reaction. So in practice, this approach often leads to poor quantum yield with the oxidation reaction being rate-limiting. Therefore, alternative, easily oxidizable electron donors, often termed *sacrificial reagents*, are very popular. These are often simple alcohols such as methanol, 2-propanol or triethanolamine. Side-effects of the use of alcohols are autoxidation with molecular oxygen or superoxide radicals, which can lead to imperfect electron balance and the so-called current-doubling effect, which may double the number of reducing equivalents per photon [108-109]. The addition of alcohols also increases the oxygen solubility in the solution, which may in turn increase the reaction rate.

The effect of the concentration of 2-propanol in the solution was studied between 0 and 30 % [47]. The formation rate rises with increased 2-propanol up to 10 % volume and declines at higher amounts. This can be explained by a better availability at higher concentrations due to better mass transfer, but too much alcohol blocks the oxygen from the catalyst surface. Also, the solubility of oxygen in the solution is higher with alcohol present. The degradation rate gets smaller with higher 2-propanol concentrations because of the preferred oxidation of the alcohol and therefore less

oxidation of hydrogen peroxide. The degradation is already suppressed down to a quarter at 1 % volume of 2-propanol in the solution because it is easier to oxidize the alcohol compared to water.

When working with sacrificial reagents, it should be considered that their oxidation also yields secondary compounds which may induce unexpected side-effects. Aldehydes such as formaldehyde often react readily with other compounds, acidic intermediates (*e.g*. formic or acetic acid) can influence the pH value. With this in mind, methanol, ethanol, 2-propanol and *tert*-butanol were studied and evaluated for their use as sacrificial reagents [110]. Methanol is oxidized to CO_2 *via* formaldehyde and formic acid, the subsequent reaction steps are faster so that no significant build-up of intermediates is observed. Ethanol is oxidized *via* acetaldehyde to acetic acid, which is relatively stable and accumulates to significant concentrations before being broken down *via* a photo-Kolbe reaction and subsequently the above-mentioned C_1-pathway. 2-propanol is oxidized to acetone, which is resistant to further oxidation and accumulates. Eventually, this can be broken down to acetaldehyde and formaldehyde which can be oxidized to CO_2 as described. In the case of *tert*-butanol, several pathways are possible which lead to a plethora of intermediates, many of them accumulating [110].

The comparison of the H_2O_2 generation rates with the different alcohols showed similar rates for the primary and secondary alcohols but a significantly lower rate for *tert*-butanol. Overall, methanol proved to be the most suitable candidate for use as a sacrificial reagent because it both yields a high H_2O_2 formation rate, and the intermediates react quickly and cannot accumulate [110].

5. Photocatalytic materials for H_2O_2 synthesis from molecular O_2 and H_2O

5.1. TiO_2-based photocatalysts

In 2013, Shirashi et al. described one of the first H_2O_2 photocatalytic syntheses by using the TiO_2 Aeroxide P25 Degussa catalyst [111]. In this work, they studied the effect of different organics in efficiency and selectivity. Figure 7 shows the mechanism that this group proposed regarding the main steps involved in the photocatalysis synthesis of H_2O_2 from molecular O_2 in aqueous solution. Titania (TiO_2) systems were logically the first family of semiconductor photocatalysts being of interest for the synthesis of H_2O_2 [110-117], due to good stability and biocompatibility as well as suited optical and electronic properties. Indeed, the CB of titania (-0.19 V *vs*. NHE) favors the reduction of oxygen into hydrogen peroxide (0.68 V).

Nevertheless, TiO_2 requires UV light to be excited, making use of only 3.3% of the solar spectrum in terms of irradiance. Furthermore, the scarce production of hydrogen peroxide obtained so far can be attributed to its surface decomposition due to further reaction at the titania surface, giving rise to complexes which are further decomposed into OH- or H_2O.

In this regard, several strategies have been followed in order to inhibit the decomposition of H_2O_2. Some studies affirm that the decomposition can be avoided if the surface -OH sites are blocked by complexation with cations like Zn^{2+} [118], or substituted by anions like F^- [119]. However, in those works, in addition to the needed use of UV light, an organic sacrificial agent (alcohol, organic acid, etc.) was employed as hole scavenger (easier to oxidize compared to water).

Also, noble metals like Au, Ag or Pt nanoparticles have been interfaced with the TiO_2 photocatalyst for this reaction. In most of cases, UV light was employed as a source of energy and also by using an organic hole scavenger. Loading with noble metals has demonstrated that the electrons in the CB of TiO_2 can be trapped by the metal particle, leading to a more efficient charge separation [113, 120-121]. Besides, it decreases the decomposition of H_2O_2 by Ti-OOH species as required and in some cases it can also absorb visible light due to the surface plasmon resonance effect [29]. Nevertheless, in some cases, like Au-decorated TiO_2, the metal particle strongly interacts with H_2O_2 promoting its depletion through reduction reactions [122]. This confirms that there are some controversial statements about how H_2O_2 is photocatalytically produced. The maximum rate achieved was 6 mM in 24 h of irradiation in presence of ethanol for Au-TiO_2. In the case of combined materials, the highest H_2O_2 production rate achieved so far is 26 mM in 20 h under UV-A light with an Au-TiO_2/carbon catalyst by using ethanol and oxygen at acidic pH [79].

In Figure 8, Tsukamoto et al. [120] shows the change in H_2O_2 concentration over time with the employment of the bimetallic-titania base catalyst and titania for the sake of comparison. The rate for H_2O_2 production becomes lower as the time proceeds due to the simultaneous peroxide decomposition.

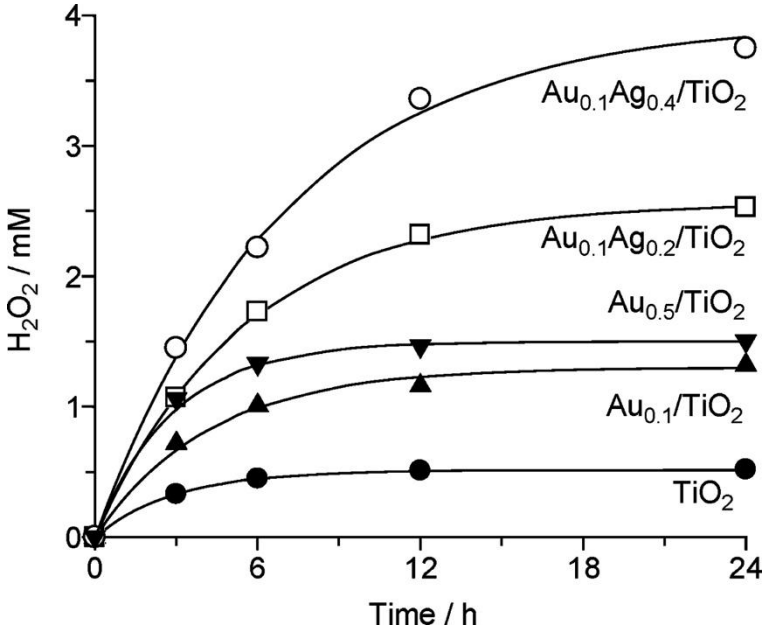

Figure 8. Time-dependent change in H_2O_2 concentration during photoreaction with respective catalysts. The reaction conditions are identical to those in Table 4. The lines are the calculated results using the equation; $[H_2O_2] = (k_f/k_d)\{1 - \exp(1-k_dt)$. Reproduced with permission from Ref. [120]. Copyright 2012 American Chemical Society.

Others propose the employment of heterojunction to promote the charge separation for higher yield achievements (*e.g.*, CoPi/T-GO/TiO_2, C-dots/r-GO/TiO_2) [105, 123]. However, the amount of H_2O_2 obtained in the range 0.08-1.3 mM was far from those of pure TiO_2 (≈40 mM).

The last strategy followed with titania is the combination with reduced graphene oxide (rGO). The interest of that resides in that rGO helps to transfer electrons to O_2 due to the fact that the Fermi level of rGO is lower than the CB of titania. In an early study, Moon et al. obtained much higher activity with rGO/TiO_2 than with bare titania [105]. Then, this composite was incorporated in a ternary heterojunction giving rise to

TiO_2/rGO/WO_3 [123]. The role of the rGO was to act as electron mediator between the two other photocatalytic phases. Nevertheless, this ternary material also employed a hole scavenger and reached relatively low yields: a final concentration of 270 µM after 1 h, without photonic yield reported.

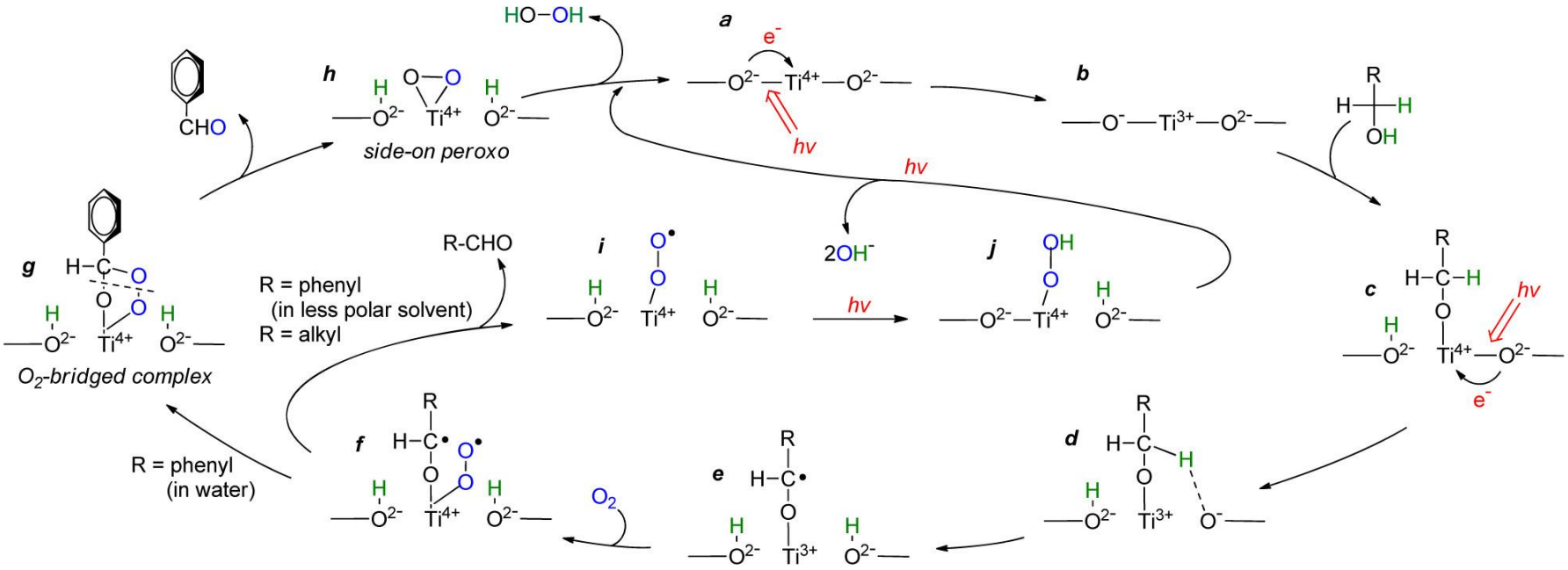

Figure 7. Proposed Mechanism for Photocatalytic Oxidation of Alcohols with O_2 on the TiO_2 surface. Reproduced with permission from Ref. [111].

Table 4. Titania-based photocatalysts for the photocatalytic production of H_2O_2.

Catalyst	Conditions	H_2O_2 measurements	Amount produced	Reference
TiO_2	Benzyl alcohol, Hg lamp UV-Vis, O_2 saturation	redox titration with $KMnO_4$	40 mM	[111]
Co@TiO_2	Methanol reduces H_2O_2 production (competition with H_2O_2)	Scavengers	1.71 mmol/L in 60 min	[112]
Au-TiO_2	UV	horseradish peroxide-catalyzed oxidation of N,N−diethyl-pphenylenediamine	0.3 mM	[113]
Au-Ag/TiO_2	Ethanol/water, O_2 saturated solution, UV radiation	redox titration with $KMnO_4$ (detection limit: 0.05 mM).	4 mM (24h)	[120]
F-TiO_2	O_2/hole scavenger (formic acid)		1.3 mM	[119]
CoPi/r-GO/TiO_2	O_2 and UV (wavelength>320 nm)	DPD method	80 µM	[105]
C-dots/r-GO/TiO_2	Disinfection/ UV/2-propanol/pH=7	colorimetric method using copper (II) ions and DMP at 454 nm	300 µM (1h)	[123]
Pt/TiO_2 (anatase)	No sacrificial agent. Water splitting with H_2 production too.	o-tolidine method	5096 µmol g^{-1} h^{-1} (first 1 h)	[121]
Carbon/Au-TiO_2	Ethanol, oxygen, pH=3	iodometric titration using the UV-Vis spectroscopy	26 mM (20h)	[79]
Carbon dots/ TiO_2 nanotube	Ethanol, UV light	redox titration using standard $Ce(SO_4)_2 \cdot 4H_2O$ solution	3.4 mM (3h)	[124]

$WO_3/TiO_2/GO$	2-propanol as hole scavenger, Xenon lamp with 1.5 AM filter	colorimetric method using copper(II) ions and DMP at 454 nm	270 µM	[123]
$Au/SnO_2/TiO_2$	Alcohol, UV light	ESR spectra	15 mM (25 h)	[125]
Nafion Coatings on S,N-Codoped Graphene-Quantum-Dots-Modified TiO_2	Solar and visible light, neutral pH, 2-propanol as hole scavenger, O_2 saturation	DPD−POD method	373 µM/h	[126]
Zn-TiO_2	Formate as scavenger, O_2, varied pH values	spectrophotometric method based on the catalysed iodide oxidation	0.22 mM	[118]

5.2. Graphitic carbon nitride based photocatalysts

5.2.1. Introduction to graphitic carbon nitride materials

g-C_3N_4 is a metal-free n-type polymeric semiconductor regarded as a promising candidate for a wide span of energy and environmental applications, as it can be activated by visible light irradiation, is produced from Earth-abundant elements by facile synthesis methods, and possesses high physicochemical stability and unique electronic band structure [127-129]. Since its first report in 2009 by Wang et al. for the photocatalytic production of hydrogen from water [130], g-C_3N_4 has been extensively employed in photocatalytic CO_2 reduction, organic pollutant degradation, organic synthesis, H_2 evolution, water splitting, nitrogen fixation, and H_2O_2 production [130-136]. g-C_3N_4 is composed by stacked 2D layered polymeric *s*-triazine or tri-*s*-triazine units interconnected through tertiary amines forming π-conjugated graphitic planes of sp^2 hybridized carbon and nitrogen with a stoichiometric C/N ratio of 0.75 (Figure 9) [128, 130, 138]. The band gap of g-C_3N_4 is approximately 2.7 eV (~460 nm), providing a wide visible-light absorption range, and the position of the conduction band is appropriate for various reduction reactions, such as H_2 evolution, CO_2 reduction and O_2 reduction [139-141]. g-C_3N_4 is thermally stable up to 600°C due to the aromatic C-N heterocycles, with complete decomposition occurring beyond 700°C. It exhibits high chemical resistance to acidic and basic media, as well as commonly used solvents (*e.g.*, water, alcohols, dimethylformamide, tetrahydrofuran, toluene and diethyl ether), owing to the Van der Waals interactions between the stacked graphitic layers [129, 142-143].

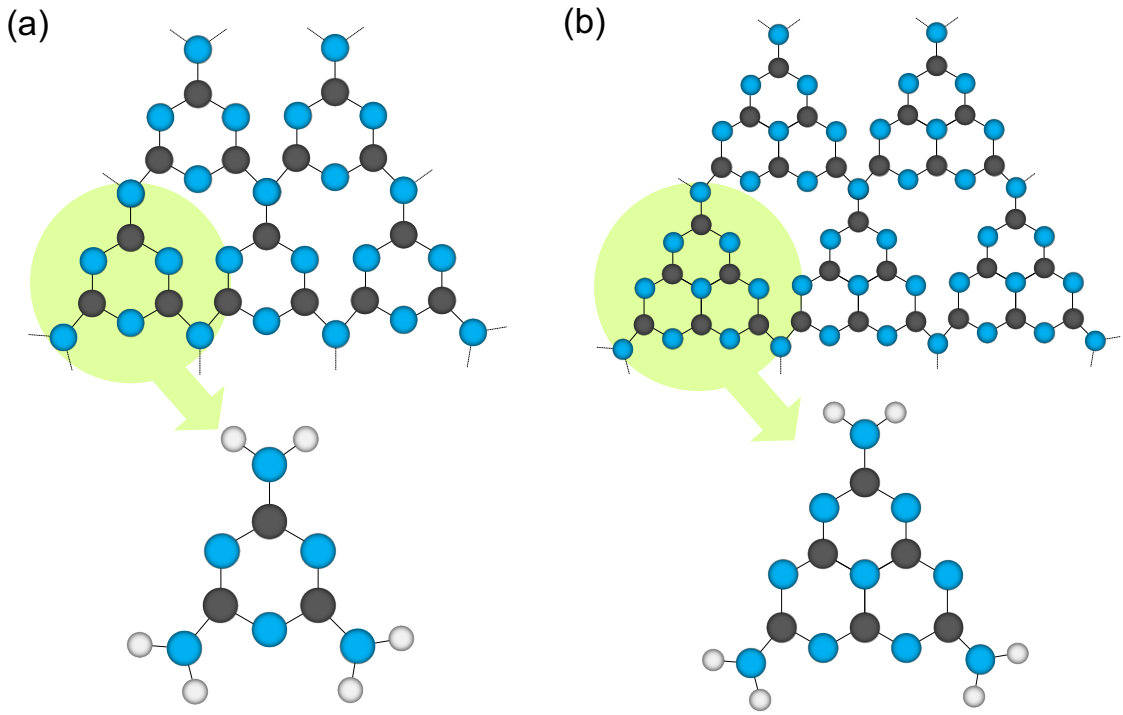

Figure 9. **(a)** Triazine and **(b)** tri-*s*-triazine (heptazine) structures of g-C_3N_4 (H, white; C, grey; N, blue).

g-C_3N_4 materials are generally synthesized by simple and cost-effective thermal polycondensation at 450-650°C of nitrogen-rich precursors, such as dicyanamide, cyanamide, melamine, urea and thiourea [46, 144-147]. The reaction pathway mainly involves three temperature-dependent processes: (i) polymerization of precursors to melamine by additional and condensation reactions, (ii) condensation of melamine releasing ammonia, and (iii) g-C_3N_4 formation *via* polymerization [128, 130, 148-150]. The precursor type, as well as the reaction conditions (temperature, duration and atmosphere), have demonstrated to influence the g-C_3N_4 physicochemical features (*i.e.*, morphology, specific surface area, porosity, C/N ratio, electronic band structure,

presence of defects and carbon/nitrogen vacancies, etc.) and, in consequence, the photocatalytic activity [151-152].

Despite the remarkable properties mentioned above, bulk g-C_3N_4 faces a few redhibitory shortcomings that hinder its practical applications, such as a low specific surface area (<10 $m^2 g^{-1}$), a high recombination rate of photogenerated charge carriers, an inefficient visible light utilization at wavelengths above 460 nm, and a relatively poor electrical conductivity, that are globally responsible of the achievement of low photocatalytic performances [153-156]. In addition, pristine g-C_3N_4 exhibits a relatively low oxidation potential of holes from VB, relative to water oxidation potential, compared to other semiconductors (*e.g.*, TiO_2 or ZnO) and a limited ability to adsorb target reactants, such as O_2 and NO [157-160]. To overcome these limitations, multiple approaches have been developed, including the exfoliation of g-C_3N_4 into nanosheets, defect engineering, nanoarchitecture engineering (*e.g.*, nanospheres, nanorods, nanoribbons, nanobelts, nanowires, etc.), hard and soft-templating, metal and non-metal doping, copolymerization, and coupling with carbon materials and/or other semiconductors, which have been discussed in the literature [128, 138, 148-149, 161-163]. Among them, thermal exfoliation into 2D nanosheets stands out for its simplicity, and allows for a significant increase in the specific surface area (it should be noted that the theoretical specific surface area of an ideal monolayer of C_3N_4 is about 2500 $m^2 g^{-1}$), facilitates the separation of charge carriers and improves the diffusion of reactants and products [149, 164].

5.2.2. Photocatalytic H_2O_2 production on g-C_3N_4 materials

g-C_3N_4 photocatalyst can selectively generate H_2O_2 under visible light irradiation and mild conditions (neutral pH, room temperature) in the presence of dissolved oxygen owing to its electronic properties and the formation of 1,4-endoperoxide species [46, 145, 165]. The conduction band of g-C_3N_4, with an energy level of approximately -1.12 eV, is properly located to promote O_2 reduction to H_2O_2, as the standard redox potential of O_2/H_2O_2 is less negative (-0.33 V *vs*. SHE; pH = 7) [166-167]. In comparison to the water oxidation route, O_2 reduction is the only pathway observed for photocatalytically generating H_2O_2 on g-C_3N_4, as demonstrated by experiments performed under anoxic conditions (in absence of oxygen) where no formation of H_2O_2 was observed [144-145, 168]. Compared to other semiconductors such as TiO_2, g-C_3N_4 displays higher selectivity (> 90%) for H_2O_2 production when activated by visible light irradiation (> 400 nm), since subsequent decomposition of the formed H_2O_2 by UV light is suppressed [46, 167]. The addition of a sacrificial agent (aliphatic or aromatic alcohols) to the g-C_3N_4 system under visible light irradiation has been reported to yield higher concentrations of H_2O_2 than in pure water, the H_2O_2 selectivity increasing as the proton-donating capacity of the organic sacrificial agent increases [46, 144-145]. In this regard, it is worth mentioning that the photocatalytic generation of H_2O_2 and the degradation of pollutants acting as proton donors can be conducted simultaneously (see section 6.1) [137, 145].

Table 5 displays a selection of recent works on H_2O_2 synthesis using g-C_3N_4-based photocatalysts including details on the reaction conditions, the H_2O_2 quantification method, and the H_2O_2 production performance. Following their pioneering works on TiO_2, Shiraishi et al. first reported the high selectivity of g-C_3N_4 for H_2O_2 production through the two-electron reduction of O_2 and proposed a mechanism involving the formation of the 1,4-endoperoxide intermediate on the catalyst surface under visible

light irradiation (Figure 10) [46]. According to this mechanism, the process takes place as follows: (a) visible light triggers electron-holes pairs generation, (b) photoexcited electrons are located at the C1 and N4 positions of the triazine ring, while holes are positioned on the N2 and N6 positions, (c) holes take α- and β-hydrogens of alcohol (sacrificial agent) producing aldehyde, (d) O_2 is reduced by photoexcited electrons forming superoxo radical, (f) superoxo radical is further reduced by another electron at the *para* position of the triazine ring to the 1,4-endoperoxide species, suppressing one-electron O_2 reduction (e), and finally the 1,4-endoperoxide species are converted to H_2O_2 by protonation [46, 165, 169]. The inhibition of the one-electron O_2 reduction to the superoxide and the formation of 1,4-endoperoxide species were confirmed by electron spin resonance (ESR) analysis and Raman spectroscopy, respectively [46].

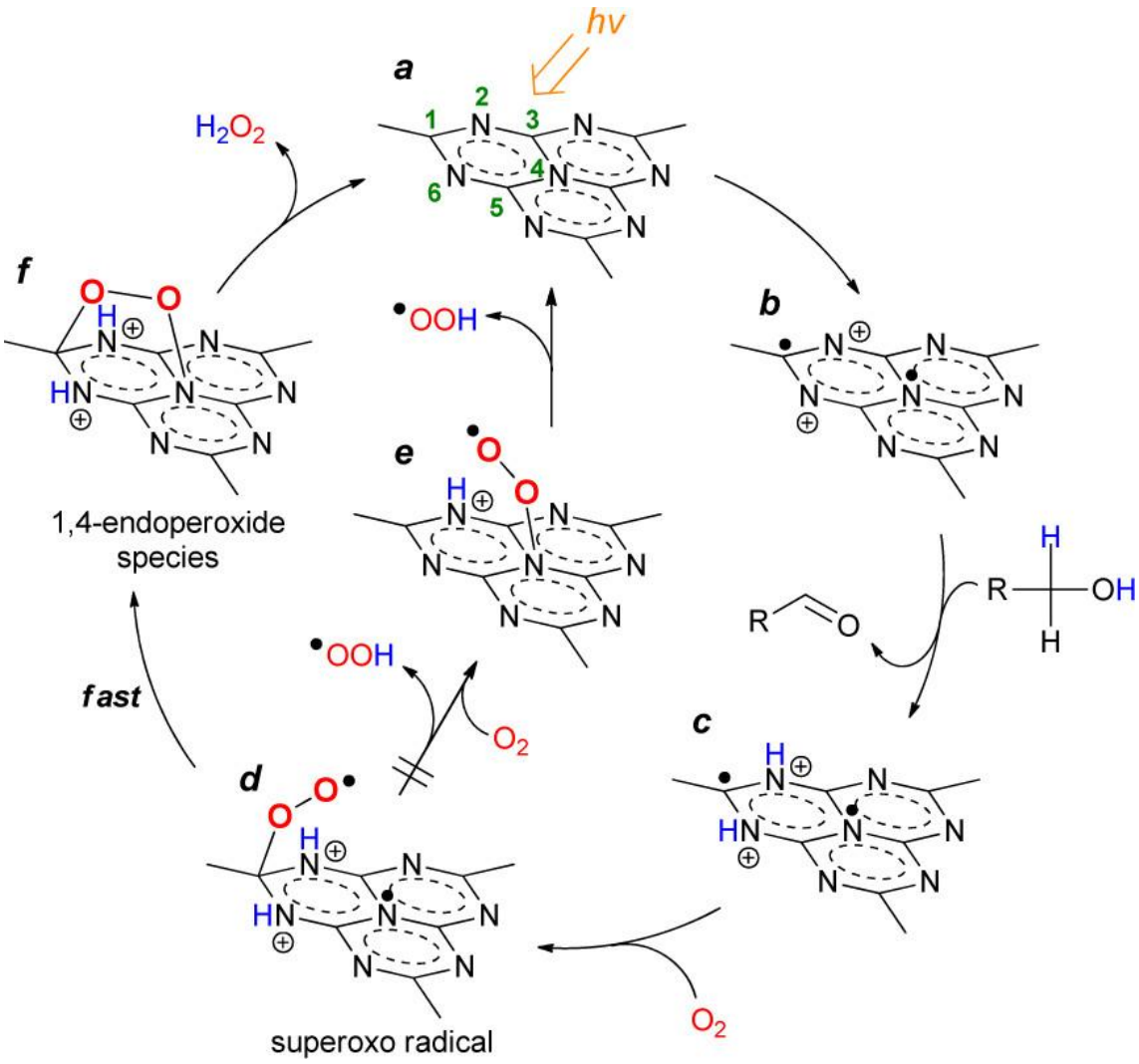

Figure 10. Two-electron O_2 reduction-based mechanism involving the surface 1,4-endoperoxide intermediate proposed by Shiraishi for the selective formation of H_2O_2 on the surface of photoactivated g-C_3N_4. Reproduced with permission from Ref. [46]. Copyright 2014 American Chemical Society.

Nanoarchitecture and defect engineering of g-C_3N_4

Subsequently, the same authors prepared g-C_3N_4 catalysts with larger surface areas by silica-templated thermal polymerization of cyanamide with the aim of improving the photocatalytic activity for H_2O_2 production [170]. Noteworthily, they

found that the selectivity for the two-electron reduction of O_2 decreased as the surface area of the catalysts increased (92% for 10 m^2 g^{-1} > 72% for 56 m^2 g^{-1} > 58% for 160 m^2 g^{-1} > 42% for 228 m^2 g^{-1}), which was explained by the formation of a large number of primary amine moieties on the surface of mesopores [170]. They proposed that these defects promoted the four-electron reduction of O_2 to H_2O, as confirmed by ESR analysis, as well as the rapid photocatalytic decomposition of the formed H_2O_2 due to the attraction between the basic primary amine sites and acidic H_2O_2 [170-171]. Liu et al. transformed amino groups (-NH_2) on the g-C_3N_4 surface into stable *N*-hydroxymethyl groups (-NH-CH_2-OH) by reaction with formaldehyde (g-C_3N_4–NH_2 + HCHO → g-C_3N_4-NH-CH_2-OH), while maintaining the morphological features, light absorption capacity, electronic structure, and charge separation and transfer ability of the photocatalyst [172]. Interestingly, g-C_3N_4 with surface -NH-CH_2-OH functions showed more energetically favorable kinetics for photocatalytic O_2 reduction to H_2O_2 in water compared to pristine g-C_3N_4, owing to enhanced O_2 adsorption and H_2O dehydrogenation properties.

In order to increase the photocatalytic activity for H_2O_2 production, Liu et al. synthesized ultra-thin g-C_3N_4 nanoplates (1-3 nm thickness) through a glucose-assisted mechanical exfoliation process, which exhibited an increased surface area (89.5 m^2 g^{-1}), a higher charge separation efficiency, and a lower charge transfer resistance compared to the a bulk g-C_3N_4 counterpart at 10.6 m^2 g^{-1} [173]. In addition, the exfoliation treatment was shown to improve the redox capacity of g-C_3N_4 by raising the CB potential and changed the reaction pathway from a sequential two-step one-electron route to a one-step two-electron reduction of O_2 to H_2O_2, as determined by Mott-Schottky and ESR analyses, respectively. g-C_3N_4 microrods with the simultaneous presence of C, N dual

vacancies and a nearly stoichiometric C/N ratio were obtained through thermal polymerization of melamine-cyanuric acid supramolecular precursors under H_2 [174]. The C and N vacancies were reported to enhance visible light absorption, suppress charge carrier recombination by trapping/donating electrons and serve as active sites for O_2 adsorption, facilitating its reduction to H_2O_2 by a sequential two-step one-electron pathway.

Non-metal doping of g-C_3N_4

Non-metal doping (C, O, P, S, B) is a strategy that has been extensively explored to improve the performance of H_2O_2 photocatalytic synthesis by g-C_3N_4. Carbon modified g-C_3N_4 photocatalysts with tunable energy levels were prepared by adjusting the concentration of glucose additive during a hydrothermal synthesis [175]. The authors found that C atoms partially replaced N atoms in the g-C_3N_4 framework, leading to an increased light absorption capacity and a positive shift of the conduction and valence bands, which improved the selectivity for the reduction of O_2 to H_2O_2 and favored the water oxidation reaction, respectively. g-C_3N_4 with oxygen-enriched structures (C-O-C and -OH), obtained using dicyandiamide and ammonium paratungstate, was demonstrated to promote the formation of the 1,4-endoperoxide species and, in consequence, the reduction of O_2 to H_2O_2 *versus* the generation of the superoxide radical [176]. According to DFT calculations, the C-O-C group (rather than the -OH group) was responsible for the increased activity, leading to an efficient charge carrier separation and favoring, especially, the final release of H_2O_2.

Phosphate modification of g-C_3N_4 by acid-hydrothermal method (22.2% H_3PO_4 solution) resulted in an increase in the surface area, a better separation of the

photogenerated electron-hole pairs, as well as an improved ability for both adsorption and reduction of O_2 [177]. As determined by O_2 temperature-programmed desorption (O_2-TPD) experiments, more O_2 molecules could be adsorbed due to the presence of phosphate on the g-C_3N_4 surface that can trap the photoexcited electrons, what is therefore enhancing the charge carrier separation. In addition, Moon et al. reported that the incorporation of phosphate species to g-C_3N_4 by solid-state thermal polymerization of melamine in the presence of dibasic potassium phosphate (~25 wt.%) facilitated the proton transfer process and suppressed the decomposition of *in-situ* generated H_2O_2 [106]. Thereby, H_2O_2 production in water was enhanced by the presence of phosphate species and less dependent on the pH of the medium (or the proton concentration). On the other hand, g-C_3N_4 was co-doped with K, P, O, and S (0.1, 1, 3, 5 and 10 wt.% K_2HPO_4, and 50 wt.% urea/thiourea as precursors), achieving higher visible light absorption and hindering the recombination of photogenerated electron-hole pairs due to the presence of heteroatoms and of N defects after doping [178]. In particular, S-doping was reported to increase the H_2O_2 synthesis performance, which was explained by a favored charge transfer through the heptazine ring [178-179].

In this context, the introduction of S atoms into the heptazine units of g-C_3N_4 nanosheets (in replacement of N atoms) has been reported to result in improved light absorption ability and charge transfer efficiency due to the reduction of the band gap and the increase of the local electronic density, respectively [180]. Although thermal exfoliation mostly leads to a wider band gap with a positive shift of CB and VB compared to the bulk g-C_3N_4, when the treatment was performed simultaneously with S-doping, a smaller shift of the VB was observed, overcoming this constraint. Furthermore, S-doped g-C_3N_4 nanosheets exhibited a highly selective two-electron reduction of O_2 to H_2O_2,

enhancing the performance of pristine g-C_3N_4 nanosheets, on which the simultaneous two-electron and one-electron reduction pathways occurred, but only a part of the superoxide radical intermediate gave rise to H_2O_2. Liu et al. synthesized non-metal (B, P, S) doped g-C_3N_4 tubes by a hydrothermal method with a subsequent thermal polymerization from a melamine-cyanuric acid supramolecular precursor (Figure 11a) [181]. The obtained tube structure (~1 μm diameter, 30-80 nm wall thickness), displayed in Figure 11b-c, was proposed to increase the light absorption capacity by multiple reflection-effect, while the dopants would promote the separation of photogenerated electron-hole pairs, as confirmed by transient photocurrent response experiments (Figure 11d), and tune the electronic structure of g-C_3N_4 [181]. XPS results (Figure 11e) indicated that B and P atoms replaced the C atoms, while N atoms were replaced by S atoms, as depicted in Figure 11f. Interestingly, in this case, H_2O_2 was mainly generated through the two-steps one-electron O_2 reduction pathway by B, P, and S- doped g-C_3N_4 tubes.

B-doped g-C_3N_4 nanoplatelets (~2.5 nm thickness) and nanosheets with a highly porous structure and a large surface area have been obtained *via* thermal polymerization followed by an ultrasound-assisted exfoliation process [182-183]. The oxidative ultrasonic exfoliation process was informed to improve both the hydrophilicity and the surface area, while B doping led to a decrease in the band gap and to an increase in the electron density at the B site, promoting charge separation and transfer [182]. It was found that the electron-deficient B-N units served as active sites for O_2 adsorption and the subsequent two-step one-electron O_2 reduction route yielded H_2O_2 [183].

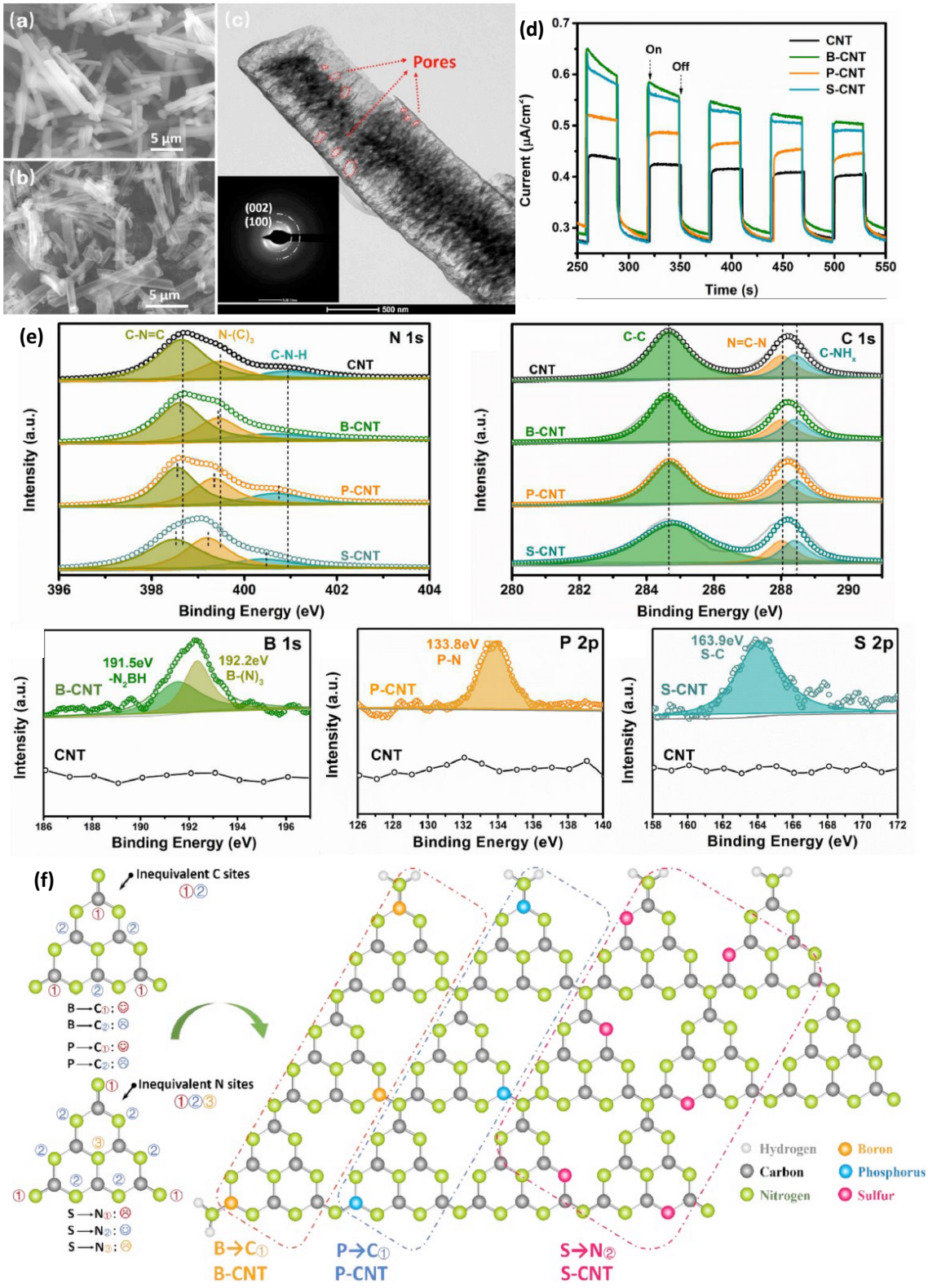

Figure 11. SEM image of melamine-cyanuric acid supramolecular precursor **(a)**; SEM **(b)** and TEM **(c)** images of g-C_3N_4 tubes (CNT); Transient photocurrent response **(d)** and XPS

spectra **(e)** of CNT and B-, P-, and S -doped CNT; Schematic diagram of B, P, and S atoms doping sites in the g-C_3N_4 framework **(f)**. Reproduced with permission from Ref. [181]. Copyright 2021 Elsevier.

Metal doping of g-C_3N_4

The doping of the g-C_3N_4 framework by alkali and transition metals has been also investigated and demonstrated to promote the photocatalytic synthesis of H_2O_2. Alkali metal (K^+ and Na^+) modified g-C_3N_4 with tunable band gap was obtained by adjusting the weight ratio of eutectic salts to the melamine precursor using the molten salt method [184]. Molten salt synthesis involves incorporating salts to the constituent precursors and carrying out the reaction at temperatures above the melting point of the salts, which act as a solvent enhancing solid-state reaction rates by increasing the contact area and mobility [185]. K^+ and Na^+ coordinated into the C-N rings and provided g-C_3N_4 with enhanced visible light absorption, larger specific surface area and reduced recombination of electron-hole pairs. K^+ and Na^+ co-doped g-C_3N_4 with a weight ratio of 20:1 for eutectic salts to melamine (1.3 wt.% and 0.7 wt.% of K^+ and Na^+ contents, respectively) was able to produce H_2O_2 in the absence of O_2 and in the presence of an electron scavenger, suggesting that H_2O_2 was not only synthesized by the O_2 reduction pathway but also by the oxidation of OH^- to $HO^\bullet$ with subsequent reaction between two $HO^\bullet$ forming H_2O_2 due to a more positive VB potential [184, 186].

Likewise, Zhao et al. introduced sodium cyanaminate moiety into g-C_3N_4 (sodium content of 6.9 wt.%) [187]. For that purpose, sodium thiocyanate (NaSCN) molten salt method was used, which resulted in a coordinative interaction between sodium and pyridinic nitrogen, as shown in Figure 12, and, together with cyanamino groups,

promoted photon absorption, charge carrier separation efficiency, O_2 adsorption and selective two-electron O_2 reduction to H_2O_2. However, reusability experiments showed that the catalyst lost both cyanamino groups and Na^+ when subjected to long-term reactions. On the other hand, potassium intercalated into the g-C_3N_4 structure by a $KHCO_3$-mediated synthesis (*ca*. 6.49 wt.%), with the simultaneous introduction of cyano groups (–C≡N) into the framework, was reported to increase the number of active sites and favor a highly selective two-electron O_2 reduction route to H_2O_2 [188].

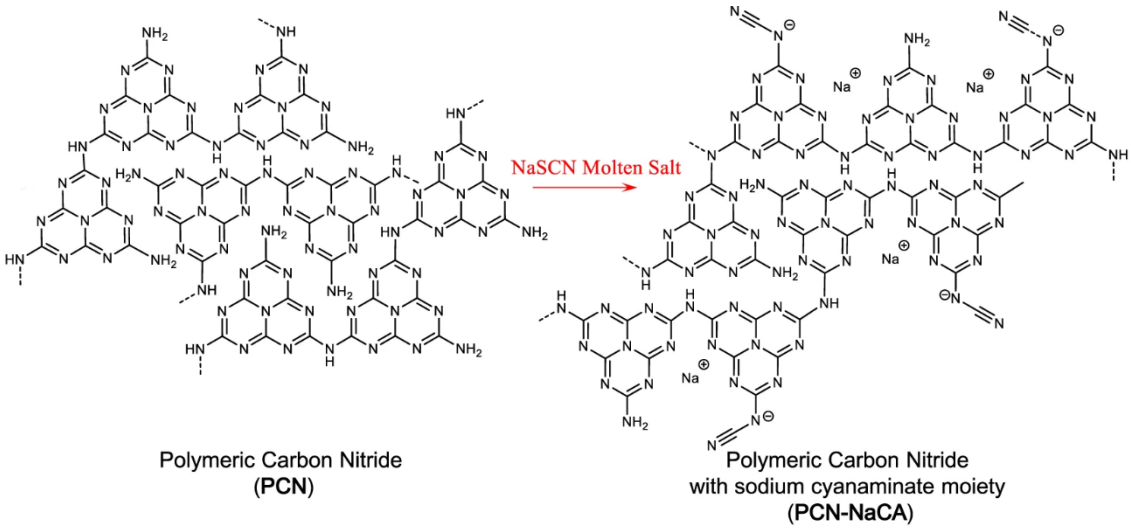

Figure 12. Schematic diagram of g-C_3N_4 with cyanaminate moiety (PCN-NaCA) synthesized from g-C_3N_4 (PCN) by the molten-salt method. Reproduced with permission from Ref. [187]. Copyright 2021 Nature Publishing Group.

Cu-doped g-C_3N_4 hollow microspheres (~100 nm diameter and 0.23 wt.% Cu content) were prepared using a SiO_2 template, where Cu^+ was inserted at the interstitial position through coordinative Cu(I)-N bonds [157]. These Cu(I)-N active sites significantly improved the O_2 adsorption capacity, while acting as a transfer bridge for

the photogenerated electrons from the catalyst to the adsorbed O_2 molecules, generating H_2O_2 by a selective one-step two-electron reduction pathway. Metal-ion incorporated single atom g-C_3N_4 photocatalyst (< 0.7 wt.% of metals species) were prepared by isolating three transition metals (Fe, Co, Ni) and two main group metals (In, Sn) sites with pyridinic N atoms [189]. It was observed that the introduction of Fe^{2+}, Fe^{3+}, Co^{2+} and Ni^{2+} favored the charge carrier recombination, leading to a decrease in the photocatalytic performance compared to bare g-C_3N_4. In contrast, In^{3+} and Sn^{4+} sites accumulated electrons during excitation, inhibiting the recombination of electron-hole pairs and promoting the adsorption of the electrophilic O_2 and its subsequent reduction.

Metal/g-C_3N_4 heterostructures

Metals and metal oxides have also been incorporated as nanoparticles into g-C_3N_4 with the purpose of improving its photocatalytic activity. In this regard, Chang et al. anchored Au nanoparticles in a C_3N_4 matrix (1.05 wt.% Au loading) through a carbon-layer-stabilized method, achieving a reduction of charge carrier recombination, which was explained by the robust metal-support interaction and the small size of the nanoparticles (~5 nm) and led to a good photocatalytic performance for H_2O_2 production [190]. Hollow tubular g-C_3N_4 was substitutionally doped with oxygen (replacing N atoms) and loaded with highly dispersed Ni nanoparticles in the size range of 20-60 nm by a photodeposition process [144]. The authors found that oxygen doping and the presence of Ni increased the visible light absorption and charge separation efficiency, while the Ni loading (2%, 4%, 6% and 8%) changed the reaction pathway from a two-step one-electron to a single-step two-electron O_2 reduction to H_2O_2, with an increase in the selectivity from 60.8% to 88.9%. Nevertheless, an excess of Ni (≥ 6% Ni loading) lowered

the performance for H_2O_2 synthesis, which was attributed to the aggregation of metal particles blocking light absorption.

Dysprosium oxide (Dy_2O_3) particles were dispersed on N-deficient g-C_3N_4 nanosheets by a simple thermal condensation route, with an observed interlayer stacking of the g-C_3N_4 structure, and a reduction of both the band gap and the photogenerated charge carrier recombination [191]. H_2O_2 formation was proposed to occur in Dy_2O_3/g-C_3N_4 systems *via* a mixed two-step one-electron and one-step two-electron O_2 reduction route. Chu et al. prepared a cyano and SnO_2 co-modified g-C_3N_4 *via* one-step pyrolysis of melamine with Na_2SnO_3 (mass ratio of 1%, 2.5%, 5% and 10% to melamine), which exhibited an enhanced photocatalytic performance for H_2O_2 production [192]. In addition to increasing the utilization of visible light and inhibiting charge carrier recombination, the introduction of cyano groups and SnO_2 nanocrystals favored the adsorption of O_2 and H^+ due to the negatively charged catalyst surface. Briefly, photoexcited electrons in g-C_3N_4 were suggested to be accepted by the cyano groups and subsequently transferred to SnO_2, where the adsorbed O_2 was reduced to H_2O_2 through a two-step single-electron pathway.

Molecular engineering of g-C_3N_4

Molecular engineering has proven to be a simple and effective approach to significantly improve the photocatalytic performance by extending the π-conjugated system or by incorporating proton donors into the g-C_3N_4 structure. In this context, Yang et al. synthesized a 2-hydroxy-4,6-dimethylpyrimidine (HDMP) grafted g-C_3N_4 through an *in-situ* keto-enol cyclization of urea and acetylacetone that improved the photocatalytic activity for H_2O_2 production [193]. The incorporation of the HDMP moiety

into the g-C_3N_4 framework enhanced the visible light absorption, as delocalized π-electrons increased, and promoted charge carrier separation and transfer. This efficient charge separation and transfer was ascribed to the electronegativity of HDMP, which accepted the photoexcited electrons while the holes remained in the heptazine moiety. 1,3,5-Trihydroxybenzene (TB)-substituted g-C_3N_4, compared to pristine g-C_3N_4, displayed larger specific surface area, improved visible light absorption capacity, and reduced charge carrier recombination, what resulted in superior photocatalytic activity for H_2O_2 synthesis [194]. In addition, as the free -NH_2 groups of the urea were partially replaced by TB (rich in -OH groups), the catalyst hydrophilicity increased. Zhang et al., reported the use of hydroxyethyl cellulose (HEC) as proton donor for modifying g-C_3N_4 *via* hydrogen bonds (0.01-0.2 mass ratio of HEC to g-C_3N_4) [195]. HEC modification was shown to promote not only proton-coupled electron transfer, but also charge carrier separation through electron transfer from HEC to g-C_3N_4, thus enhancing H_2O_2 production performance.

Proton-coupled electron transfer also occurred when AQ was anchored onto C_3N_4 (10 wt.% of AQ-COOH) by heat-induced hybridization method without altering its structure, with in consequence the favored formation of H_2O_2 and the reduction of its decomposition [76]. As shown in Figure 13, AQ molecules are suggested to accept photoexcited electrons from C_3N_4, and to transfer them to initiate the hydrogenation reaction of AQ to anthrahydroquinone (AQH_2), H_2O_2 being formed as side-product of the dehydrogenation of AQH_2 back to AQ with the reduction of O_2. Torres-Pinto et al. also obtained an enhanced photocatalytic performance for H_2O_2 production using an AQ-functionalized g-C_3N_4 catalyst (10 wt. % of AQ) prepared by a simple hydrothermal method [196]. The increased H_2O_2 formation was explained by the replacement of some

functional groups in g-C_3N_4 with C-O, C=O bonds and quinone groups. Specifically, the C-O bond has proton-donating capacity, and the C=O and quinone groups would trap electrons due to their high electronegativity, thus suppressing charge carrier recombination and favoring the formation of intermediate radicals (*e.g.*, hydroperoxyl radicals).

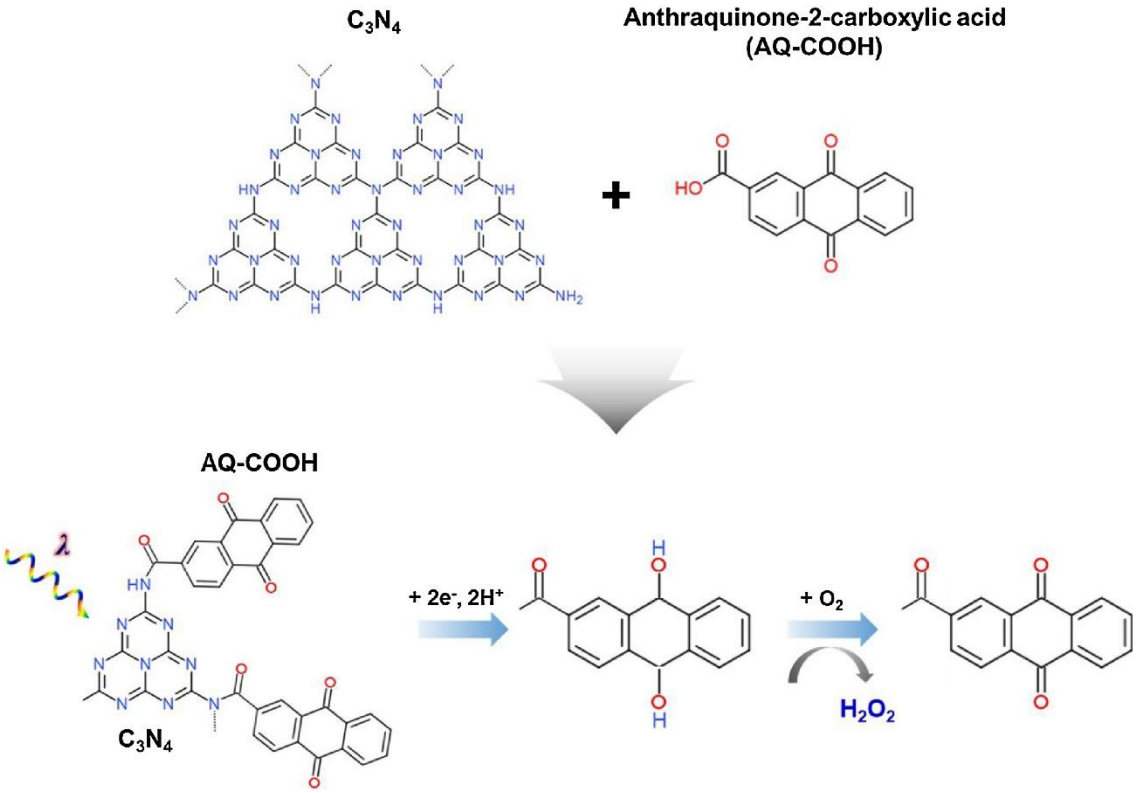

Figure 13. Schematic diagram of the coupling process of C_3N_4 with AQ and the photocatalytic synthesis of H_2O_2 by AQ/C_3N_4 under solar light irradiation. Reproduced with permission from Ref. [76]. Copyright 2018 Elsevier.

Semiconductor/g-C_3N_4 heterojunctions

Heterojunction construction is a strategy that has been shown to favor charge carrier separation and transfer, and in consequence to lead to an improved photocatalytic activity for H_2O_2 production. The growth of $NiIn_2S_4$ on C_3N_4 with lamellar structure resulted in a highly efficient $C_3N_4/NiIn_2S_4$ heterostructure with a larger number of catalytic sites, higher visible light absorption and better separation of the photogenerated charge carriers [197]. Additionally, the authors found that the Ni atoms from the $C_3N_4/NiIn_2S_4$ heterojunction possessed mixed valence states (Ni^{3+} and Ni^{2+}), giving the composite a low electrical resistance. Farzin et al. elaborated a Z-scheme heterojunction system by decorating oxygen-doped g-C_3N_4 nanosheets with $NaBiS_2$ nanoribbons that achieved an effective charge separation, as electrons and holes accumulate in the CB of $NaBiS_2$ and the VB of oxygen-doped g-C_3N_4, respectively, and generated H_2O_2 following the one-step two-electron O_2 reduction pathway [198]. $Bi_4O_5Br_2$ nanorods (~3.8 nm diameter, 25-30 nm length) decorating on g-C_3N_4 nanosheets (25, 50 and 75 wt.% of $Bi_4O_5Br_2$ to g-C_3N_4) were also proposed to form a highly efficient Z-scheme system [199]. In this case, photoinduced electrons accumulated in the CB of g-C_3N_4 would be responsible for the reduction of O_2 to H_2O_2 *via* simultaneous one-step two-electrons and two-steps one-electron pathways, while electrons in the CB of $Bi_4O_5Br_2$ would combine with the holes in the VB of g-C_3N_4 (Figure 14). Furthermore, it was found that the holes in the VB of $Bi_4O_5Br_2$ had the potential to oxidize H_2O molecules to O_2 and $HO^{\bullet}$, which subsequently combined with each other to form H_2O_2.

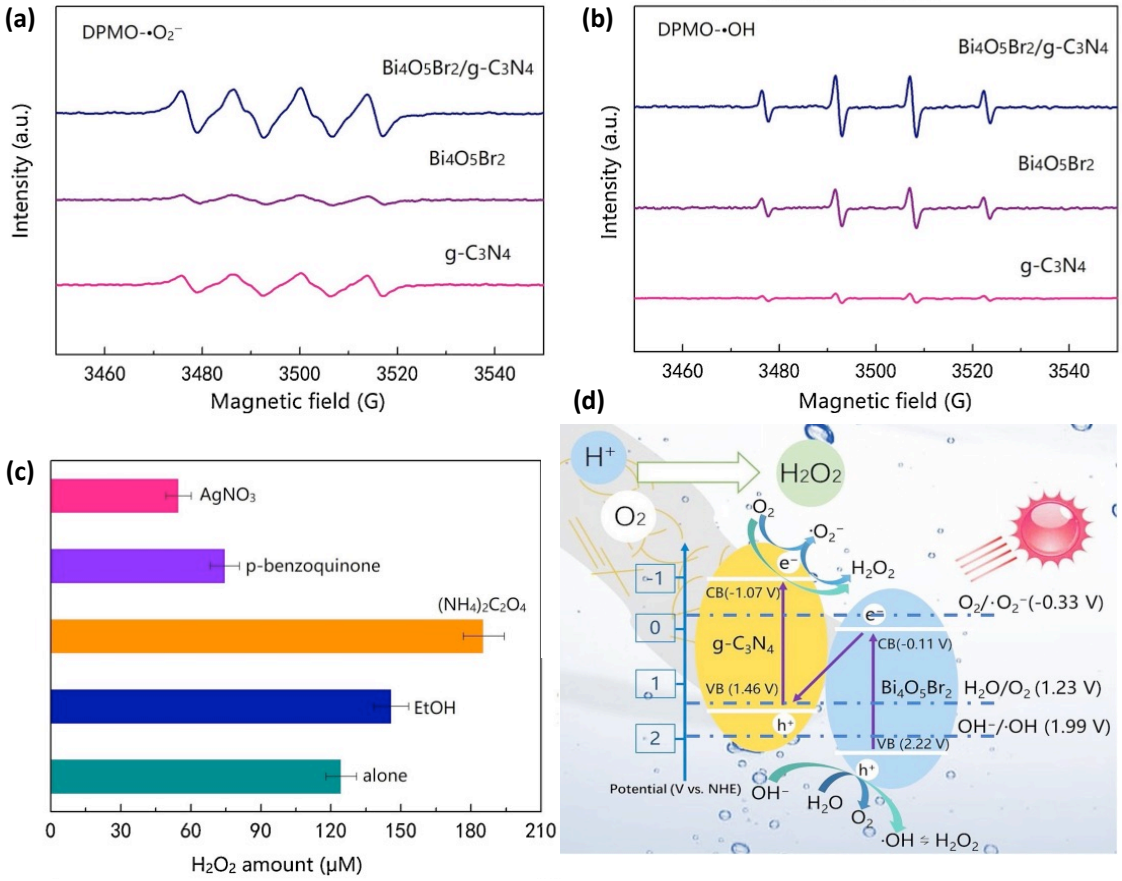

Figure 14. EPR spectra of DMPO-$O_2^{\bullet-}$ **(a)** and DMPO-$^{\bullet}$HO **(b)** for g-C_3N_4, $Bi_4O_5Br_2$ and $Bi_4O_5Br_2$/g-C_3N_4. Photocatalytic production of H_2O_2 on $Bi_4O_5Br_2$/g-C_3N_4 in the presence of $AgNO_3$, *p*-benzoquinone, $(NH_4)_2C_2O_4$ and ethanol (EtOH) as scavenger species for electrons, superoxide radicals, holes and hydroxyl radicals, respectively **(c)**. Proposed mechanisms for the photocatalytic synthesis of H_2O_2 by a Z-scheme mechanism on $Bi_4O_5Br_2$/g-C_3N_4 **(d)**. Reproduced with permission from Ref. [199]. Copyright 2020 Elsevier.

An interfacial Schottky junction constructed by an electrostatic self-assembly process from Ti_3C_2 nanosheets and porous g-C_3N_4 nanosheets (1, 2 and 5 wt.% of Ti_3C_2 to g-C_3N_4) was reported to enhance visible light absorption, photogenerated electron-

hole pairs separation and thus the performance for O_2 reduction to H_2O_2 *via* a two-step single-electron pathway [200]. Photogenerated electrons were proposed to migrate from g-C_3N_4 to Ti_3C_2 with the formation of a Schottky barrier, which prevented electrons from back-transfer to the g-C_3N_4 semiconductor, and lowered charge carrier recombination. Yang et al. reported the simultaneous formation of a Schottky barrier-type junction and a Z-scheme mechanism by decorating the surface of g-C_3N_4 with Ti_2C_3 and BiOCl, which synergistically promoted the photocatalytic synthesis of H_2O_2 [201]. In such a mechanism involving the photogeneration of electrons and holes in both g-C_3N_4 and BiOCl semiconductors of the Ti_2C_3/g-C_3N_4/BiOCl composite upon the sunlight irradiation, the photoexcited electrons in the CB of BiOCl could combine with the holes in the VB of g-C_3N_4, favoring the oxidation reaction in the VB of BiOCl. Meanwhile, the electrons in the CB of g-C_3N_4 were transferred to Ti_2C_3 taking part in the reduction of O_2 to H_2O_2.

The formation of a g-C_3N_4/Co_9S_8 heterojunction by coating the surface of Co_9S_8 nanosheets with ultrathin protonated g-C_3N_4 (2, 5 and 10 wt.% of g-C_3N_4 to Co_9S_8) was proposed to favor visible light absorption and both separation and transfer of photogenerated electron-hole pairs, resulting in a higher photocatalytic activity for H_2O_2 production (Figure 15a) [202]. In the g-C_3N_4/Co_9S_8 composite, the photoexcited electrons migrated from the CB of g-C_3N_4 to the CB of Co_9S_8, participating in the one-step two-electron reduction of O_2 to H_2O_2 pathway, and the holes were transferred from the VB of Co_9S_8 to that of g-C_3N_4 (type-II heterojunction), as displayed in Figure 15b. Moreover, the remaining electrons in the CB of g-C_3N_4 can form H_2O_2 *via* a *two-step* single-electron O_2 reduction route, thus allowing both pathways to simultaneously occur in the composite. Finally, an isotype heterojunction consisting of g-C_3N_4 doped with

benzene-rings, which partially replaced the heterocyclic rings in the g-C_3N_4 network, and P-doped g-C_3N_4 was constructed and demonstrated efficient charge carrier separation and enhanced visible light absorption [203]. The electronic structure of the composite resulted in the promotion of photoinduced electrons from the benzene-ring doped g-C_3N_4 to the P-modified g-C_3N_4, and vice versa in the case of holes (type-II heterojunction).

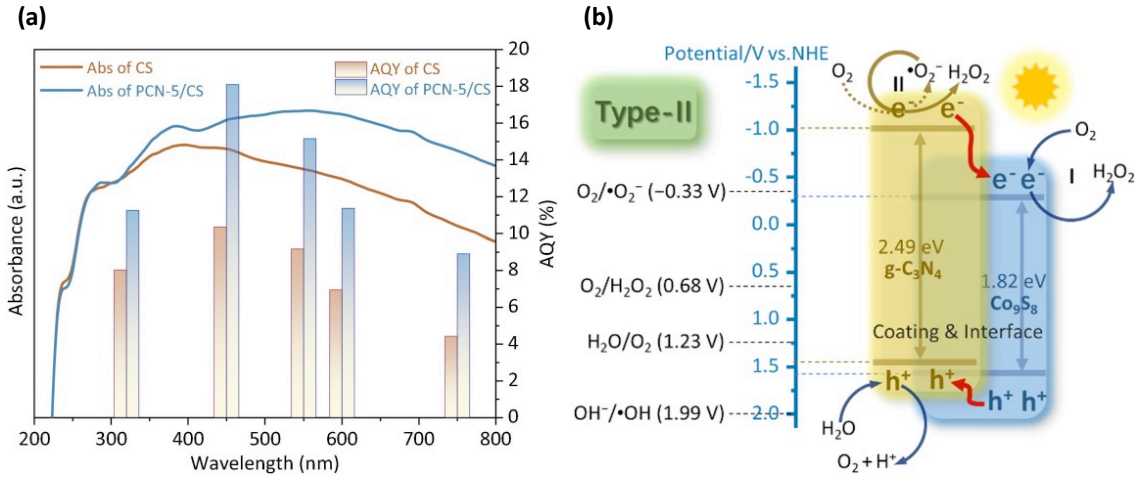

Figure 15. UV–vis absorption spectra and wavelength-dependent apparent quantum yield (AQY) of photocatalytic H_2O_2 production on Co_9S_8 (CS) and g-C_3N_4/Co_9S_8 (PCN-5/CS) **(a)**. Proposed mechanism for the photocatalytic synthesis of H_2O_2 by a type-II heterojunction on g-C_3N_4/Co_9S_8 **(b)**. Reproduced with permission from Ref. [202]. Copyright 2022 Elsevier.

Stability of g-C_3N_4 photocatalysts

The stability of photocatalytic materials under reaction conditions is a key-factor for practical application and, therefore, has been also extensively studied for H_2O_2

synthesis using g-C_3N_4 based catalysts. Reusability tests and physico-chemical characterization have shown that g-C_3N_4 photocatalysts are stable and recyclable for H_2O_2 production [144, 157, 172-175, 177-178, 182, 184, 194, 199-203]. It must be stressed that the negligible reduction in photocatalytic performance observed in some cases corresponds typically to the inevitable catalyst loss that occurs during the test cycling of the powdery catalysts in slurry reactors when submitted to multiple recovery steps. For instance, ultra-thin g-C_3N_4 nanoplates maintained a yield of more than 75% for H_2O_2 synthesis, while no changes were observed by FTIR, XRD and XPS characterization after ten test cycles [173]. The activity and crystal structure of K-, P-, O-, and S-doped g-C_3N_4 did not change significantly after four reaction cycles [178]. SEM and XRD analyses proved that both the morphology and the crystal structure of Ni-loaded oxygen-doped g-C_3N_4 nanotubes were stable under the photocatalytic reaction conditions upon five 4 h-long cycles, keeping over 81% activity for H_2O_2 generation [144]. The catalytic stability of metal-doped g-C_3N_4 systems has been also confirmed by measuring metal concentrations after reaction using ICP [157]. Elemental analysis by ICP was also used to demonstrate that the C/N ratio did not change after five cycles using carbon-doped C_3N_4 catalysts [175].

Table 5. g-C_3N_4-based photocatalysts for H_2O_2 production.

Catalyst	Conditions	H_2O_2 measurements	Amount produced	Reference
g-C_3N_4	2 kW Xe lamp (λ > 420 nm, 26.9 W m^{-2}), 90% ethanol, O_2 saturation	$KMnO_4$ titration	30 µmol (12 h)	[46]
Mesoporous g-C_3N_4	2 kW Xe lamp (λ > 420 nm, 26.9 W m^{-2}), 90% ethanol, O_2 saturation	$KMnO_4$ titration	90 µmol (24 h)	[170]
g-C_3N_4 with -NH-CH_2-OH groups	5 W LED lamp (λ > 420 nm, 30 mW cm^{-2}), no scavenger, air bubbling	Iodometry	179 µmol L^{-1} (7 h)	[172]
Ultra-thin g-C_3N_4 nanoplates	Visible light (400 nm ≤ λ ≤ 700 nm), 10% isopropanol, dry air purging	DPD-POD method [a]	43.07 µmol g^{-1} h^{-1}	[173]
g-C_3N_4microrods with C, N dual vacancies	300 W xenon lamp (λ > 420 nm), 10% isopropanol, O_2 bubbling	Iodometry	~718.36 µmol g^{-1} h^{-1}	[174]
Carbon-content C_3N_4	300 W Xe lamp (100 mW cm^{-2}), 5% isopropanol, O_2 saturated, acidic pH	DPD-POD method	1271 µmol L^{-1} (4 h)	[175]
Oxygen-enriched g-C_3N_4	500 W Xe lamp (λ >420 nm), O_2 saturation, pure water or supplemented with 10% isopropanol	Iodometry	53 µmol (10 h) in water, 300 µmol (5 h) when supplemented with isopropanol	[176]
Phosphate-modified g-C_3N_4	250 W high-pressure sodium lamp with $NaNO_2$ solution filter (400-800 nm), EDTA scavenger (7.5 wt%), O_2 bubbling	Iodometry	5.4 mM (18 h)	[177]

C_3N_4 with heteroelements (K, P and O)	300 W Xe arc lamp (λ ≥420 or ≥320 nm; 726.8 and 833 mW cm^{-2}), 10% ethanol, O_2 saturation	DPD-POD method	~2mM (12 h)	[106]
K-, P-, O-, and S-co-doped g-C_3N_4	300 W Xe lamp (λ ≥ 420 nm), 10% vol isopropanol, O_2 saturated, pH = 3	Iodine titration	6.231 mM (180 min)	[178]
Sulfur-doped g-C_3N_4	300 W Xe lamp (λ > 420 nm), 10% isopropanol, O_2 saturated	Iodometry	566.69 µmol g^{-1} h^{-1}	[180]
B-, P-, S -doped g-C_3N_4 tubes	Simulated solar light, 10% isopropanol, O_2 bubbling	Iodometry	1830.98, 1677.75 and 1189.56 µM (2 h)	[181]
B-doped g-C_3N_4 nanoplatelets	6 neon lamps (20 W, 400-800 nm), 5% vol isopropanol, O_2 saturated	Iodometry	4240.3 µM g^{-1} h^{-1}	[182]
B-doped g-C_3N_4 nanosheets	LED 365 nm (100 mW cm^{-2}), 10% isopropanol, O_2 bubbling	Iodometry	1.16 mmol L^{-1} h^{-1}	[183]
K^+, Na^+- modified g-C_3N_4	250 W high-pressure sodium lamp with $NaNO_2$ solution filter (400-800 nm), no scavenger, O_2 bubbling	Iodometry	4.6 mM (18 h)	[184]
g-C_3N_4 with sodium cyanaminate moiety	Solar simulator (100mW cm^{-2}), 3.5 wt% glycerol, O_2 bubbling	DPD-POD method	18.7 µmol mg^{-1} h^{-1}	[187]
g-C_3N_4 decorated with K and cyano groups	300 W Xenon lamp (λ > 420 nm, 69.5 mW cm^{-2}), 10% isopropanol, O_2 saturated	Iodometry	278.9 µmol L^{-1} h^{-1}	[188]
Cu-doped g-C_3N_4	250 W high-pressure sodium lamp with $NaNO_2$ solution filter (400-800 nm), no scavenger, O_2 saturated	Iodometry	4.8 mM (18 h)	[157]

Fe, Co, Ni, In, Sn - C_3N_4 (single atomic catalyst)	500 W Xe lamp (λ >420 nm), 10% ethanol, O_2 bubbling	Colorimetric method using PACKTEST (4-Aminoantipyrine)	0.1-7.5 mg L^{-1}	[189]
Au-C_3N_4	300 W Xe lamp (100 mW cm^{-2}), 5% isopropanol, O_2 bubbling, acidic pH	DPD-POD method	1320 µM (4 h)	[190]
Ni-loaded oxygen-doped g-C_3N_4 nanotubes	300 W Xe lamp (λ ≥ 420 nm, 100 mW cm^{-2}), 10% vol ethanol	Iodometry	2464 µmol g^{-1} h^{-1}	[144]
Dy-oxide (Dy_2O_3)/nitrogen-deficient g-C_3N_4	Simulated solar light (25°C), 10 % ethanol, O_2 purging	Iodometry	48.36 mM g^{-1} h^{-1}	[191]
Cyano and SnO_2 co-modified g-C_3N_4	300 W Xe lamp (λ >420 nm), O_2 bubbling, 10 % vol isopropanol as sacrificial agent, acidic pH	Iodometry	703.4 µM g^{-1} h^{-1}	[192]
2-hydroxy-4,6-dimethylpyrimidine / C_3N_4	300 W xenon lamp (λ >420 nm), 10% isopropanol, O_2 bubbling	Iodometry	174 µmol L^{-1} (60 min)	[193]
1,3,5-Trihydroxybenzene substituted g-C_3N_4	300 W xenon lamp (λ > 400 nm, 100 mW cm^{-2}), 10% isopropanol, O_2 bubbling	Iodometry	257 µM h^{-1}	[194]
Hydroxyethyl cellulose-modified g-C_3N_4	PLS-SXE300D xenon lamp (λ ≥ 420 nm), no scavenger, O_2 saturated	DPD-POD method	65.76 µmol L^{-1} (60 min)	[195]

Anthraquinone (AQ)/ C_3N_4	Simulated solar light (100 mW cm^{-2}), 10% 2-propanol, O_2 bubbling	Titanium (IV) oxysulfate DPD-POD method	361 µmol g^{-1} h^{-1}	[76]
Glucose, perylene and anthraquinone functionalized g-C_3N_4	4 LEDs (417 nm, 450 W m^{-2}), 90% isopropanol, O_2 saturated	Titanium (IV) oxysulfate	11.1 (glucose), 14.2 (perylene) and 25.0 mmol g^{-1} h^{-1}	[196]
$C_3N_4/NiIn_2S_4$	300 W xenon lamp (λ > 420 nm, 100 mW cm^{-2}), 10% ethanol, O_2 saturated	Iodometry	1080 µmol L^{-1} h^{-1}	[197]
Oxygen-doped g-C_3N_4 nanosheet/$NaBiS_2$ nanoribbon	Xe lamp (25 ^oC), 10% isopropanol, O_2 bubbling	Iodometry	8.92 mmol L^{-1} (180 min)	[198]
$Bi_4O_5Br_2$/g-C_3N_4	300W Xenon (λ > 420 nm), no scavenger, O_2 saturated	$KMnO_4$ titration	124 µM (60 min)	[199]
Ti_3C_2/C_3N_4	200 W xenon lamp (λ >420 nm), 10% isopropanol O_2 bubbling	Iodometry	131.71 µmol L^{-1} (60 min)	[200]
Ti_2C_3/g-C_3N_4/BiOCl	300 W Xenon lamp, 5% isopropanol, O_2 saturated, pH = 2-3	Indirect UV-vis spectrometry	1275 µM (60 min) and 2277 µM (120 min)	[201]
Protonated g-C_3N_4 coated Co_9S_8	300W Xe lamp with cut-off filter, no scavenger, no O_2 supply, alkaline medium	$KMnO_4$ titration	2.17 mM (5 h)	[202]
g-C_3N_4 doped with benzene-ring / P-modified g-C_3N_4	9 W LED blue lamp (450 ± 5 nm, 43.6 mW cm^{-2}), no scavenger, O_2 bubbling	Iodometry	41.02 µmol L^{-1} (60 min)	[203]

[a] DPD-POD method: N,N-diethyl-1,4-phenylene-diamine sulfate (DPD), peroxidase (POD) horseradish.

5.3. Other photocatalytic systems

Aside from carbon nitrides and common inorganic semiconductor photocatalysts such as ZnO [204], TiO_2, or noble metal (Au, Pt, Au-Ag) modified TiO_2 [205], other semiconductors have also been applied for this process. The employment of some oxides and sulphides must be remarked, including MoS_2, CuO, and Ag_2O, most of them doped either with metals or with other semiconductors, like in Au-MoS_2, Cu_2O-CuO and WO_3-Ag-Ag_2O, for boosting the separation and the transfer of carriers while promoting the molecular O_2 activation [206-208]. The example of Cu_2O-CuO nanocomposite systems is highlighted in Figure 16.

Also, polymeric materials emerged as promising low-cost and easily processable materials for solar-driven H_2O_2 production, such as linear conjugated polymers [209], polymer networks [210-211] (*e.g.*, covalent organic frameworks (COFs), covalent triazene frameworks (CTF), resins [212-213], and pigments/dyes [214-215] in the form of thin films or powders.

The search for new systems is driven by the need to overcome the main drawbacks of most of the reference catalysts, namely the necessity to use a sacrificial agent and to extend the usable wavelengths towards the visible fraction of the solar light spectra. This section reports on a wide span of photocatalytic systems, either briefly itemized in Table 6 or more detailed in specific paragraphs.

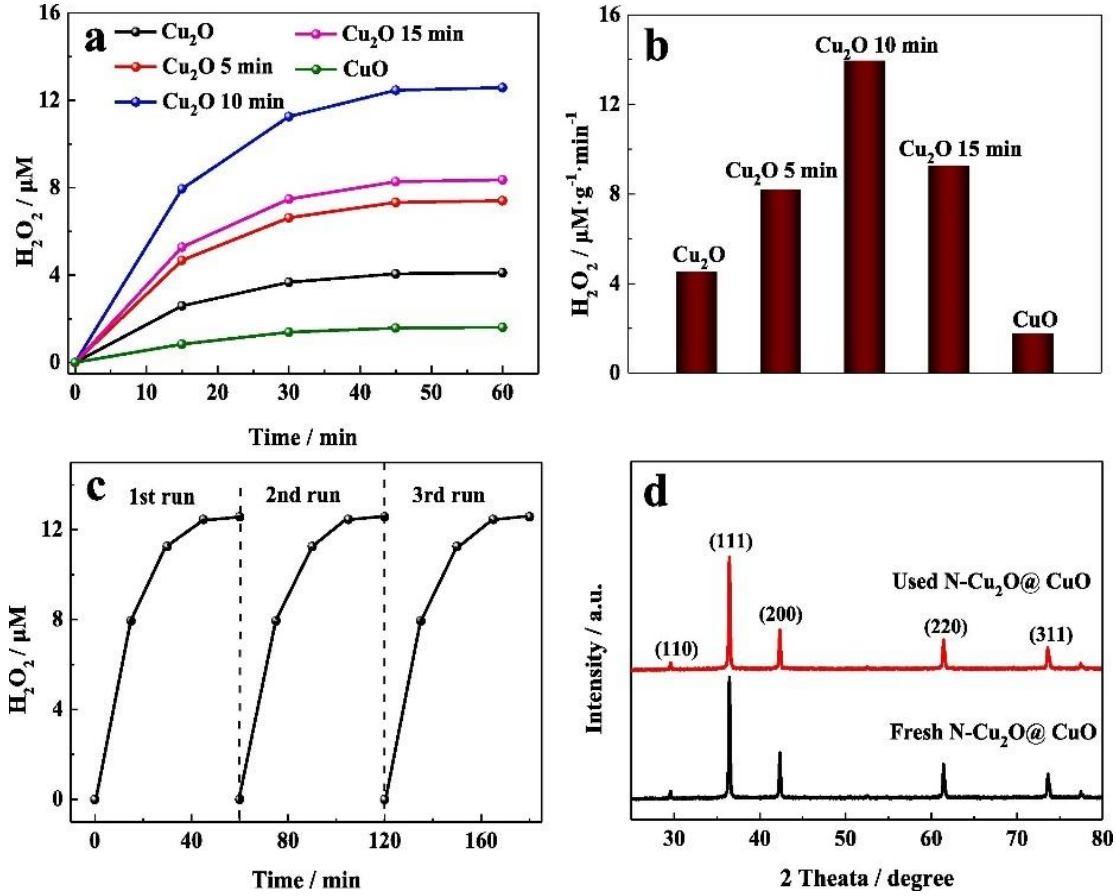

Figure 16. (a) Time-dependent photocatalytic H_2O_2 yields and **(b)** rates of Cu_2O octahedrons and N-doped Cu_2O@CuO after the nitrogen plasma treatments for different time of 5.0–15 min, taking pristine CuO as the control. **(c)** Recycling experimental results of N-doped Cu_2O@CuO nanocomposites in the photocatalytic H_2O_2 generation reactions, and **(d)** XRD patterns of the nanocomposites before and after being used for three runs of photocatalytic reactions, where the nanocomposites were yielded by the 10-min N_2 plasma treatment for Cu_2O octahedrons. Reproduced with permission from Ref. [208]. Copyright 2022 Elsevier.

Table 6. Selected semiconductor photocatalysts.

Catalyst	Conditions	H_2O_2 measurements	Amount produced	Reference
CN_{QDS} @MA-Ag	300 W Xenon lamp; 420 cut-off filter	Fluorescence (products of H_2O_2-HPAA)	≈5 µmol/L	[216]
WO_3/Ag@Ag_2O	300 W Xenon lamp; 420 cut-off filter norfloxacin	Different scavengers	-	[206]
Pd-$BiVO_4$	CH_3OH (hole scavenger) Visible light	Colorimetric based on the change of colour of Fe^{2+} to Fe^{3+}	>300 µM in 2h > 600 µM with phosphate buffer	[217]
$La_2Zr_2O_7$/rGO	Visible light, tetracycline oxidation	Scavengers (catalase)	Non measured	[218]
C_3N_4 biphenil Diimide (e-defficient)	Visible light		Milimollars levels	[219]
Au-MoS_2	sunlight		600 µM	[207]
Bi/$Bi_2O_{2-x}CO_3$	NO_x removal	ESR spectroscopy	1.2 mM	[220]
CN/rGO@BPQDs	Visible light	Iodine titration	1 µmol/Lmin	[221]
SN-GQDs Graphene, quantum-dots	Water/propanol, acidic pH Saturated with O_2 and visible light	DPD–POD method (peroxidase)	420 µmol /L in 60 min	[117]
ZIF	Xenon lamp, water, O_2 continuous flow	GC-FID (GC-2014, Shimadzu, Japan) and titration method	0.15 mmolL/L in 2h	[222]
Nitrogen (N)-doped Cu_2O@CuO	Visible light; Xe lamp cut-off visible light	PHPAA-based analysis method		[208]

Ni_2P/carbon dot	O_2 saturation, visible light, no sacrificial agent	potassium permanganate titration.	1281.4 µmol/h/g	[223]

5.3.1. Organic dyes

In a search for low-cost and robust semiconductors, Głowacki and group [215] have pioneered the use of dyes and pigments as promising ORR photo-electrocatalysts. In 2016, carbonyl-based organic pigments, epindolidione (EPI), and quinacridone (QNC) coated photoelectrodes have been reported to catalyze the two-electron oxygen reduction to H_2O_2 in low pH environments (Figure 17A) [215]. Of these two, EPI showed a more efficient two-electron ORR activity. The EPI pigment produced 3 mM of H_2O_2 within 48 h in O_2 purged system and 0.1 M HCl as the electrolyte, surpassing the g-C_3N_4 system reported in 2014 [46]. To improve H_2O_2 generation, organic heterojunction photocathodes with varying thicknesses of donor-acceptor layers based on phthalocyanine (H_2Pc) and perylene tetracarboxylic diimide (PTCDI) and EPI or PTCDI as the catalyst layer were constructed by the same group. To limit electron-hole recombination, a layer of Au was incorporated. The heterojunction photocathode, PN/Au/PTCDI and PN/Au/EPI, attained continuous H_2O_2 generation with a faradaic yield of 86-62% within 6 h of photoelectrolysis [224].

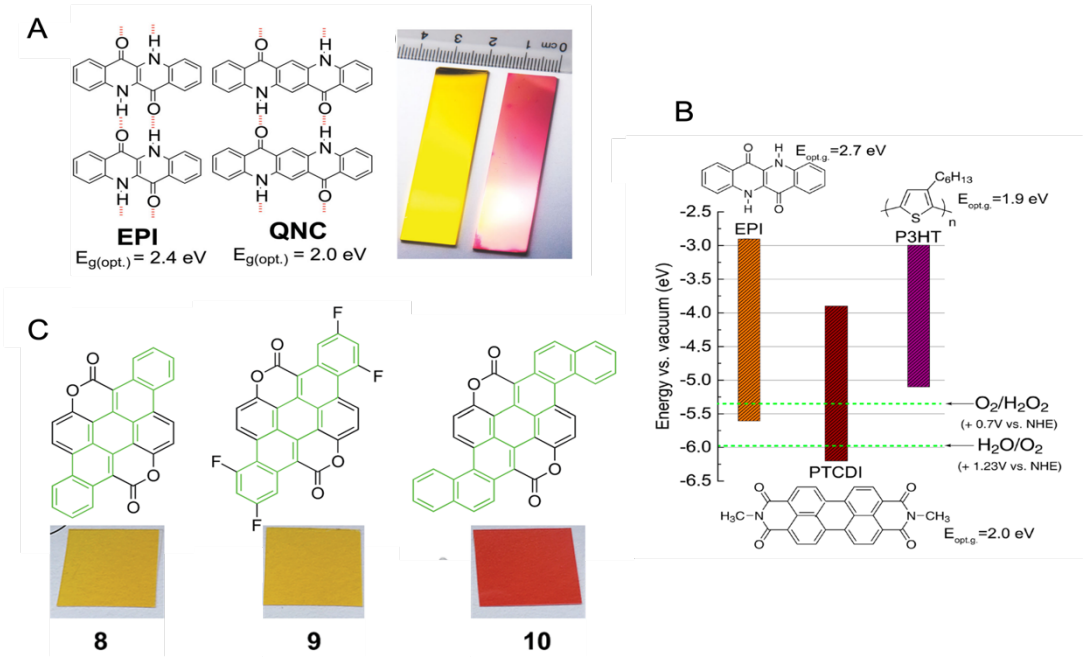

Figure 17. Dye-based organic semiconductors photocatalysts for H_2O_2 production. **A)** Molecular structures of EPI and QNC and its corresponding thin films coated on Au-coated glass slide. Reprinted with permission from Ref. [215]. Copyright 2016 Wiley-VCH. **B)** Energy diagram and molecular structures of EPI, PTCDI, and P3HT. Reprinted with permission from Ref. [225]. Copyright 2018 America Chemical Society. **C)** Molecular structures of biscoumarin-based pigments. Reprinted from Ref. [226]. Copyright 2017 Royal Society of Chemistry.

This work was further extended by depositing the organic semiconductors, EPI, PTCDI, and poly(3-hexylthiophene) (P3HT), in a TPU screen protector foil to examine the photocatalytic activity of the dyes in different electron donors (Figure 17B). Oxalate and phenol at pH 2 or 7 were shown to be the best electron donors for EPI and PTCDI with a possible turnover number for H_2O_2 production of 10-800. Further analysis shows that although PTCDI is capable of water oxidation to form H_2O_2, the H_2O_2 formation with PTCDI *via* oxygen reduction predominates. Compared to thin films, colloidal crystals of EPI showed faster H_2O_2

evolution rates due to an increase in the catalytic surface area. The mechanism of H_2O_2 production with EPI was recently studied by DFT and identified to be similar to the AQ method [227]. Based on the theoretical calculations, the hydrogen atoms in EPI-2H (reduced form of EPI after photoinduced 2 H^+/2 e^- process) are capable of abstracting triplet oxygen, $^3O_2$, forming an intermediate complex of $HOO^\bullet$ and EPI-$H^\bullet$. The $HOO^\bullet$ after released, will abstract another hydrogen atom from EPI-$H^\bullet$, forming H_2O_2, and thereby regenerating EPI in the process (Figure 18). Another pathway being considered was the abstraction of hydrogen from neighboring EPI-2H, forming EPI-$H^\bullet$. Although it can be perceived that the hydrogen in N-H could also participate in the hydrogen atom transfer (HAT) (Figure 17A), their DFT calculations also showed negligible participation of hydrogen from N-H, which coincides with their earlier experiment [215, 227].

Inspired by the performance of EPI and QNC, they evaluated three types of biscoumarin-containing molecules (Figure 17C, compounds 8-10). Visible light irradiation of the compounds in pure water and ambient air conditions showed an evolution rate of 1-3 μg_{H2O2} mg^{-1} h^{-1}. The biscoumarins did not show any degradation and were stable in the pH range of 2-13. Similar to the structure of the previous molecules EPI and QNC, the carbonyl functionalities in biscoumarin compounds were identified as the key factor for their observed catalytic activities [226].

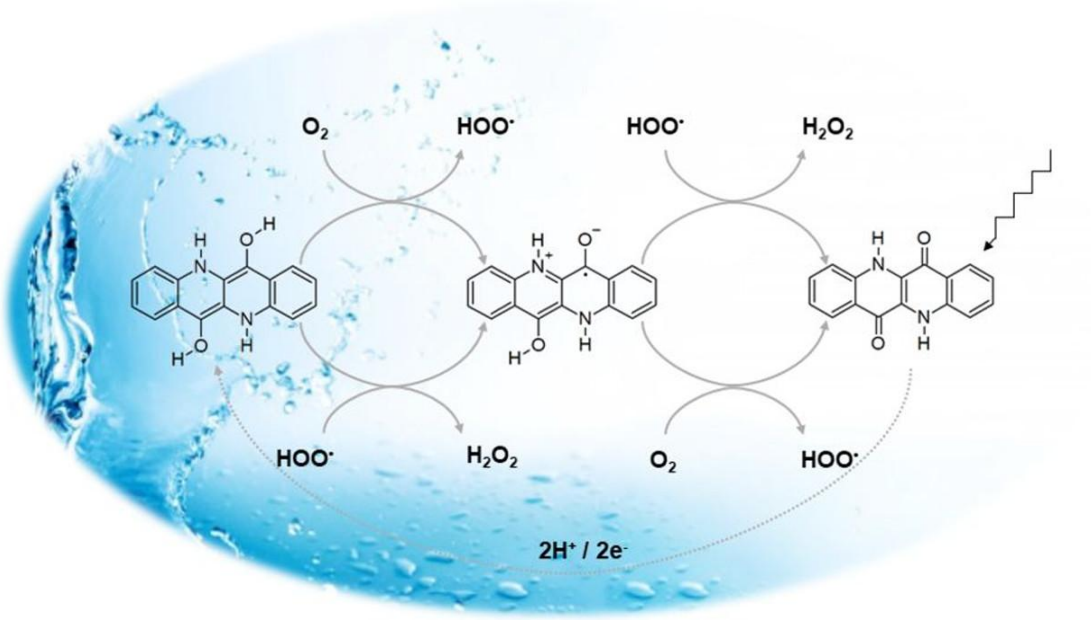

Figure 18. Proposed mechanism for H_2O_2 formation *via* two-electron ORR of EPI. Reprinted with permission from Ref. [227]. Copyright 2020 American Chemical Society.

5.3.2. Conjugated polymers

Aside from the utilization of organic semiconductors, many efforts have been dedicated to synthesizing π-conjugated polymers with attractive functionalities to drive kinetically-challenging redox reactions [228]. Well-known semiconducting polymers such as polyaniline (PANI), polypyrrole (PPy), and polythiophene (PTh), poly(3,4-ethylenedioxythiophene) (PEDOT) are known to possess catalytic activity towards oxygen reduction based on the early electrocatalytic studies [229-231]. However, in the past years, designing conjugated polymers, especially with donor and acceptor moieties, has become a popular approach to tune photocatalytic H_2O_2 generation from two-electron ORR [232]. Shiraishi and co-workers reported that resorcinol-formaldehyde (RF) resin (Figure 19A) prepared by the simple hydrothermal treatment could catalyze the overall photosynthesis of H_2O_2 production. These

RF powders have a broad light absorption of up to 700 nm and a low band gap of 1.7 eV. The polymeric system composed of π-conjugated and π-stacked benzenoid-quinoid donor-acceptor (D-A) units, serving as the sites of redox reactions, achieved a solar-to-chemical conversion (SCC) efficiency of ∼0.7% for H_2O_2 production under O_2 and simulated solar conditions [212]. However, the D-A units were linked by non-π- conjugated methylene, producing a discontinuous band that interferes with the charge transport. The same group achieved an improvement in H_2O_2 amount and SCC efficiency to ∼1% under solar irradiation when these RF powders were doped with poly(3-hexylthiophene-2,5-diyl (P3HT)). P3HT enhances the charge transport of the photogenerated electrons by acting as a conducting linker between the quinoid and benzenoid units [213].

Inspired by the utilization of AQ in H_2O_2 production, phenanthrequinone (PQ) (which possesses two adjacent carbonyl functionalities in cyclohexane linking two phenyl groups) was utilized as a redox-active site for the same purpose. Cross-coupling of 2,7-dibromophenanthrenequinone (PQ) and 1,1,2,2-tetrakis(4-ethynylphenyl)ethene with phenanthrequinone moieties as redox centers were reported as a photocatalyst for H_2O_2 production. Within the polymeric chain, tetraphenylene and phenanthrenequinone serve as the electron-donating and electron-withdrawing groups. The improved photocatalytic activity is attributed to the push-pull effect of these substituents, which improves the light-harvesting and separation of the photo-induced charges. As the redox-active site, phenanthrenequinone accepts the photogenerated electrons and transfers them to adsorbed O_2 through an electron-coupled hydrogenation reaction (PQ to PQH_2). The H_2O_2 production rate of BPTEE-COP and PQTEE-COP reached 982 and 3009 μmol g^{-1} h^{-1} respectively from H_2O and O_2 under visible light irradiation (> 400 nm) without any sacrificial agent (Figure 19B) [233].

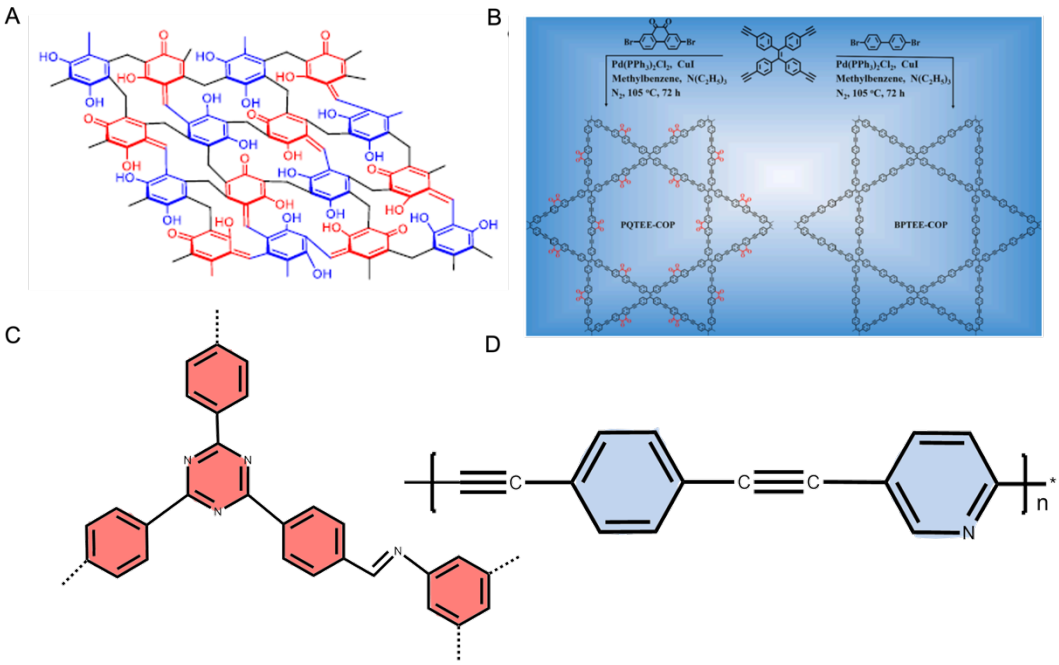

Figure 19. Molecular structures of **A)** resorcinol-formaldehyde resin. Reprinted with permission from Ref. [212]. Copyright 2020 Nature Publishing Group. **B)** PQTEE-COP and BPTEE-COP. **C)** sonoCOF-F2 **D)** DE7. Reprinted with permission from Ref. [233]. Copyright 2023 Elsevier.

Pushing the utilization of conjugated polymers as two-electron ORR catalysts, high throughput experiments were recently conducted to screen many conjugated linear polymers and covalent organic frameworks (COFs) as potential photocatalytic systems [209, 234]. COFs are emerging photocatalysts for solar-to-fuel conversion. It is a porous crystalline organic material made up of covalently linked organic moieties. They are highly tunable polymers such that one can change the charge transfer kinetics and charge separation just by incorporating molecules such as triazine, porphyrin, benzothiadizole, or even alternating donor-acceptor moieties into the covalent framework [235]. Linear conjugated polymer poly(3-4-ethynylphenyl)ethynyl)pyridine (DE7) (Figure 19D) showed efficient activity towards

photocatalytic two-electron ORR to H_2O_2. At short reaction times, DE7 was more active than the reported RF resins with an apparent quantum yield of 8.7% at 420 nm. However, this polymer decomposed after 50 hours of reaction [209]. The same group performed high-throughput sonochemical synthesis and explored 76 conjugated organic polymers for H_2O_2 production. Imine-based COF coined as sonoCOF-F2 showed the highest photocatalytic H_2O_2 production among all the tested polymers (Figure 19C). Without any sacrificial agents, sonoCOF-F2 produced > 300 µmol H_2O_2 within 90 h of visible light irradiation, which was further improved using benzyl alcohol as electron donor [234]. Diarylamine moiety, a strong reducing agent, has been used to design a (diarylamino) benzene-based COF for H_2O_2 production [236]. The highest H_2O_2 production rate was obtained with TAPD-$(Me)_2$ COF (97 µmol g^{-1} h^{-1}) under visible light with ethanol as an electron donor. In another study, triphenylbenzene-dimethoxyterephthaldehyde-COF (TPB-DMTP-COF) was rationally designed. DFT calculations show that O_2 molecules were being activated and reduced in the TBP region. Moreover, by immobilizing the TPB-DMTP-COF in carbon paper, a triphase system (gas-liquid-solid) was realized, which facilitated high O_2 transfer rate leading to the enhancement in the photocatalytic activity [237]. From using organic semiconductors to novel conjugated polymers, studies have suggested that rationally designing materials with organic moieties acting as the activation center is a useful approach toward H_2O_2 photosynthesis.

5.3.3. Miscellaneous catalysts

Similar to the reports on EPI, QNC, and biscoumarins, the presence or incorporation of oxygen functional groups is very beneficial for oxygen reduction reaction to H_2O_2. Hou and Wang first reported the potential of pure graphene oxide (GO) to catalyze H_2O_2 photoproduction without any electron donors [205]. Metal-free GO reached a millimolar

concentration of H_2O_2 after 6 hours of solar irradiation at pH 7. The addition of oxalate as an electron donor enhanced the photoproduction at low pH. The authors proposed a similar two-electron ORR pathway identified for g-C_3N_4, although further studies are necessary [205]. Carbon dots incorporated in a polymer formed by dye-crosslinked molecule procyanidine and 4-methoxybenzaldehyde (PM-CDs) have also been shown to be very efficient photocatalysts for H_2O_2 production. While the polymer alone also generated H_2O_2 at a rate of 771 µmol g^{-1} h^{-1}, the incorporation of carbon dots (CDs) has significantly improved the photoproduction (1776 µmol g^{-1} h^{-1}), especially in a seawater medium. According to the authors, the functional groups -OH, C=O, -COOH of the carbon dots efficiently traps electrons, thereby increasing the time of electron-hole separation, while the ions in seawater ionize the functional groups on the surface of CDs, which increases the "electron sink effect" inducing a higher photocatalytic activity in seawater [238]. Recently, enhanced selectivity and activity of H_2O_2 production were obtained with oxidized carbon nanotubes (O-CNTs) [49]. The increase in the oxygen content (C=O, C-O) by simple surface oxidation treatment enhances the oxygen reduction performance, further substantiating the importance of oxygen functional groups. Based on DFT calculations, carbon atoms adjacent to oxygen functional groups, COOH and C-O-C, were the active sites of two-electron ORR.

6. *In-situ* photocatalytic synthesis of H_2O_2

As hydrogen peroxide is often used as a reagent in chemical reactions, there is also the option of integrating the photocatalytic peroxide synthesis directly into these reactions. This way, the peroxide is generated *in-situ*, skipping the otherwise required process steps of separation, purification and concentration as well as storage and transportation. The resulting

integrated processes may therefore be more efficient, less expensive, and also safer, as no concentrated peroxide solutions need to be handled. This section reports on the interest of the *in-situ* photocatalytic synthesis of H_2O_2 for Fenton-type advanced oxidation processes for water treatment and for organic synthesis. The coupling of *in-situ* H_2O_2 synthesis with enzymes as well as the direct in-situ generation of other technical peroxides are also discussed.

6.1. *In-situ* synthesis for water treatment

In water treatment, the *in-situ* synthesis of H_2O_2 is usually associated to a catalytic Fenton-type process that operates in homogeneous or heterogeneous phase through the catalytic decomposition of H_2O_2 in the dark or under light by Fe cations via the $Fe^{III/II}$ redox cycle (34-35).

H_2O_2-mediated Fenton-type catalysis is a family of Advanced Oxidation Processes (AOPs) promising for the removal in water of a large panel of (bio)recalcitrant (refractory) compounds that are not degraded by classical treatments, or at least for their degradation into readily biodegradable compounds [239]. As part of AOPs, this catalysis is based on the generation of highly active HO_x• (HO• and HOO•) oxidative radicals that react with the pollutant and further with the reaction intermediates to yield full mineralization of the pollutant. Are concerned, the homogeneous catalytic Fenton process, or its heterogeneous counterpart, Catalytic Wet Peroxide Oxidation (CWPO) for which Fe is incorporated as cation in a catalytic solid [240]. Photo-CWPO (also called heterogeneous photo-Fenton) consists in performing the CWPO process under light, as a strategy to enhance the catalyst reactivity by further boosting the rate-limiting $Fe^{III} \rightarrow Fe^{II}$ conversion in the $Fe^{III/II}$ redox cycle (Eqs. 34-35). In a typical Fenton-

type catalysis, the Fe-catalyzed H_2O_2-mediated generation of HO_x• leads to initial reaction rates far higher than those achieved in photocatalysis on semiconductors [239].

$$Fe^{3+} + H_2O_2(h\upsilon) \rightarrow \ Fe^{2+} + HOO^{\bullet} + H^{+} \quad (34)$$

$$Fe^{2+} + H_2O_2(h\upsilon) \rightarrow Fe^{3+} + HO^{\bullet} + OH^{-} \quad (35)$$

Albeit very active, and although H_2O_2 is a green oxidant, producing only H_2O and O_2 as end-products, H_2O_2-mediated Fenton-type catalysis still faces a limited perspective for technological deployment. This results from the external use of costly H_2O_2 instead of O_2 as oxidant, its non-sustainable production *via* the AQ process, and the moderate H_2O_2 efficiency value of the catalytic reaction, owing to a high rate of useless recombinations of radicals. Also, commercial H_2O_2 solutions are stabilized with inhibitors that act as poisons for the catalyst.

In a typical reaction, the concentration of external H_2O_2 oxidant is usually exceeding that of stoichiometry, and a very high proportion of H_2O_2 is wasted inefficiently in side-reactions. For instance, Li et al. have calculated that *ca.* 25% of the amount of externally-added H_2O_2 was used for the degradation of an organic pollutant in a homogeneous system, the efficiency dropped down to 0.4% in a heterogeneous H_2O_2/Fe_3O_4 system in dark conditions [241].

In consequence, there is a need for the development of new processes and/or of novel materials combining two catalysts working in synergy, the first one producing and providing H_2O_2 *in-situ* to the second one for degrading the pollutants. For instance, formic acid, hydrazine and hydroxylamine were used as substitutes to molecular H_2 to generate H_2O_2 for performing the degradation of phenol by Fenton reaction using *in-situ* generated hydrogen peroxide. The combined process operated at ambient conditions in a semi-heterogeneous mode using a Pd/Al_2O_3 catalyst (for the production of H_2O_2) and soluble Fe^{2+} as homogeneous

catalyst (for the decomposition of H_2O_2 into active radicals), as well as in a fully heterogeneous mode with $FePd/Al_2O_3$ catalysts [242]. It must be said that the catalysts were more stable in the presence of formic acid than hydrazine or hydroxylamine. Using the degradation of phenol in aqueous phase, Hutchings et al. attributed to the absence of any stabilizing additives such as acetanilide or phosphoric acid, the superiority of generating *in-situ* H_2O_2 from molecular O_2 and H_2 on Fenton-type Pd-Fe bimetallic catalysts supported on TiO_2 and SiO_2 in comparison to the addition of commercial H_2O_2 as oxidant [243]. Very recently, Sable et al. combined adsorption and catalytic properties for the Fenton-like oxidation of phenol over Pd/Fe-ZSM-5 catalysts allowing the *in-situ* formation of H_2O_2 using formic acid as H-source and externally-supplied oxygen [244].

In the search for efficient and sustainable heterogeneous solutions, an elegant and high-prospect approach relies on the use of H_2O as hydrogen provider instead of external molecular hydrogen. In that case, two main strategies are investigated. The first one consists in operating with two different heterogeneous catalysts working in tandem for the synthesis of H_2O_2 from H_2O and molecular oxygen, and further its use as oxidant over a heterogenized photoFenton catalyst. Usually close proximity of both active sites strongly enhances the overall process yield. The second one consists in using the dual ability of some catalysts to oxidize water and to be used as a photocatalyst for degrading organic pollutants in water, and diffusion limitations of the H_2O generated should be avoided.

Finally, as the sacrificial agent used to enhance the H_2O_2 production needs usually to be present in the aqueous media in by-far higher concentrations than the pollutants to degrade for playing a significant role, the necessity to design photocatalysts able to operate in the absence of any sacrificial agents is highly important. Also the degradation of the sacrificial

agent forms various reaction intermediates and consequently complexifies the aqueous mixture and alter the impact of the sacrificial organic substrate(s).

The approach of *in-situ* synthesis of H_2O_2 is only in its infancy, but we have to stress that the objective is not to compete with the industrial anthraquinone process in terms of kinetics or production level. The strategy aims at delivering H_2O_2 only from water and molecular O_2 as reagents in the closest vicinity of the surface active site of the Fenton-type catalysts. While the maintain of the Fe-catalyzed decomposition kinetics in the absence of any costly external H_2O_2 supply would be seen as a holy grail, *a priori*, even moderate production of H_2O_2 should be beneficial and allow the external supply of H_2O_2 to be significantly lowered.

6.2. H_2O_2-mediated organic synthesis

Beside degradation and mineralization of pollutants in water, it must be said that synthetic chemistry is also an area of interest for the one-pot combination of the *in-situ* generation and use of H_2O_2. Indeed, the use of H_2O_2 as an *in-situ* oxidant is a promising research field that finds applications in catalysis also beyond the specific area of light-mediated catalytic water treatment. One can cite for instance the propylene oxidation to propylene oxide, the valorization of methane into methanol, or the cyclohexane oxidation into cyclohexanone and cyclohexanol (mixture known as KA oil) [38].

Already approximately 30% of the global peroxide production is utilized for chemical synthesis [245]. This market is also expected to grow steadily as more and more oxidation processes are converted to utilize greener oxidants. One example is the oxidation of propylene to propylene oxide, where using hydrogen peroxide (HPPO process) has been established as a green alternative to the waste-intensive chlorohydrin-process [246]. There are some early

attempts to also realize this reaction directly with oxygen as oxidant using photocatalysis to activate it *in-situ* to superoxide or hydrogen peroxide [247-248].

In addition to the already industrially implemented propylene oxidation, there is also extensive research into other H_2O_2-mediated oxidation reactions, which could all potentially be coupled with photocatalytic *in-situ* production. A noteworthy example is the production of adipic acid from cyclohexanol/one. This is industrially realized by oxidation with highly concentrated nitric acid which is associated with notable NOx and N_2O emissions. So H_2O_2 is explored as a greener alternative which can also be envisioned to be produced *in-situ* by a photocatalytic process [249-251].

6.3. Coupling of *in-situ* H_2O_2 synthesis with enzymes

The use of enzymes as biocatalysts has many advantages such as excellent selectivity and the typically mild reaction conditions [252]. The oxyfunctionalization of non-activated C–H, C–C or C=C bonds using enzymes has not yet been fully embraced by industry [253]. The main problems are the catalyst availability and the cofactor dependency of most oxidoreductases [254]. The so-called *Oxygen Dilemma* describes the disruption of electron transfer from the cofactor nicotinamide adenine dinucleotides (phosphate) (NAD (P) H) *via* a mediator to the active site of monooxygenase through oxygen [255]. The use of H_2O_2 as a cofactor comes with the advantages of using a green reagent and contains oxygen which is already reduced for catalysis with oxygenases. For example, the usage of the unspecific Peroxygenase from Agrocybe aegerita (*AaeUPO*) can hydroxylate a substrate with reduction of hydrogen peroxide to water and produces only water as the byproduct.

Different enzymes can use H_2O_2 as cofactor for example Peroxidases, Peroxygenases, Hydrolases and Haloperoxidases. The active center of peroxidases forms a heme center and a

coordinated ligand which can be cysteine (*Aae*UPO, P450) or histidine (HRP) [256]. An oxygen from the hydrogen peroxide can coordinate on the heme-Fe^{III}. Vanadium-dependent haloperoxidases form a peroxo-complex with the vanadate group in presence of H_2O_2 and are more robust against H_2O_2 than heme-dependent enzymes [257]. Hydrolases are capable of oxidizing carboxylic acid to their corresponding peracids [258]. The *Aae*UPO is known for many different oxidations like aromatic and aliphatic hydroxylations, alkene epoxidations, heteroatom oxidations, ether cleavage, halogenations and one-electron oxidations [259].

A major disadvantage of using peroxidases and peroxygenases is the relative instability to H_2O_2 even in the millimolar range. H_2O_2 as a strong oxidant can oxidize labile amino acids [259]. Amino acid oxidations affect enzyme stability when these undergo polymerization reactions or when an amino acid close to the active site is oxidized. Another instance of inactivation occurs when the hydrolyzed heme center reacts with another molecule of H_2O_2. Further reactions with oxygen and hydrogen peroxide leads to the generation of biliverdin under release of the iron [260]. The solution to the inactivation problem is to synthesize H_2O_2 *in-situ* to avoid hot spots in concentration, such as those caused by stoichiometric addition. Amongst others, the photocatalytic production of hydrogen peroxide offers a promising solution to this challenge [261-262].

The combination of enzyme catalysis with heterogeneous photocatalysis has the advantage that the utilized light is the only energy source and the photocatalyst can be easily removed from the product [72]. With the usage of water as electron donor, there is no waste left, but the hydrogen production rate is low and so is the turnover rate of the enzyme. With methanol or other alcohols as electron donors the production rate is significantly increased with only CO_2 as waste. The oxidation of water generates hydroxyl radicals, which quickly inactivates the enzyme so the usage of methanol also stabilizes the enzyme in solution [263].

The UV light used, which is required to stimulate TiO_2, for example, also inactivates the enzyme. Nevertheless, turnover numbers of 220,000 and an apparent quantum yield of 13.6% could be achieved. By enzyme immobilization a spatial separation of enzyme and inactivating radicals can be achieved, in addition, UV light can be avoided by using photocatalysts with a smaller band gap and therefore the efficiency further optimized. All three methods described have the disadvantage that they work with peroxide to a limited extent, so that the enzyme works below its K_m value and the turnover rate is reduced. The turnover numbers achieved are nevertheless high, due to the reaction conditions optimized for stability [264].

6.4. Direct *in-situ* generation of other technical peroxides

In addition to hydrogen peroxide a number of other peroxides are relevant in many applications. This is mostly due to the fact that H_2O_2 is inherently unstable, making its transport and storage problematic. Peroxides of acids such as percarbonate, peracetate, persulfate or perborate are therefore interesting alternatives, as they form precipable salts which are easier to handle than solutions. They also typically show faster reaction kinetics than H_2O_2 under many conditions. One reason for this is that the peroxide anions are more reactive and peracids are much easier to deprotonate than H_2O_2.

These peracids are typically produced by reacting the acid with concentrated H_2O_2 solutions. However, there is also evidence for their formation *via* direct oxidation or *via* hydroxyl radicals. An example of this is percarbonate, which occurs as peroxydicarbonate ($C_2O_6^{2-}$) and as peroxymonocarbonate (HCO_4^-). The generation of the peroxymonocarbonate should take place in hydrogen carbonate solutions via an OH· activated HCO_3·, which reacts with a CO_2 dimer $(CO_2)_2^*$ and the HOO^- formed by H_2O_2 to build HCO_4^- [265]. The

peroxydicarbonate can be synthesized electrochemically by BDD's in concentrated sodium carbonate solution [266]. In addition to percarbonate, it is also possible to generate electrochemically other peroxo-species such as peracetic acid [267], perphosphate [268] or persulfate [269]. Due to the similar mechanism and the presence of hydroxyl radicals in photocatalytic systems, it is highly likely those species may be formed *via* photocatalysis as well.

7. Conclusion

H_2O_2 is a green and powerful oxidant able to oxidize in mild conditions a large range of organic and inorganic substrates in liquid media, that differentiates from stoichiometric oxidants by its high active oxygen content and by the release of H_2O and O_2 as only end-products. However, the scientific literature dealing with the photocatalytic synthesis of H_2O_2 from water and molecular oxygen is still lower compared to other key-reactions and applications in photocatalysis such as water treatment, artificial photosynthesis of solar fuels, water splitting or photoreforming. The pioneering, albeit recent, works on TiO_2 under UV-A light and further on g-C_3N_4 under solar light paved the way for cutting-edge research and stimulating key-challenges that drive the actual research in the high-prospect field of the artificial photosynthesis of H_2O_2. As we have tried to point out here, some recent works have reported interesting results in respect of the fundamental mechanistic understanding of the reaction and of the advanced engineering of solar-light driven heterogeneous photocatalysts.

The artificial photosynthesis of H_2O_2 offers prospects to boost sustainability of the production of H_2O_2, albeit being in its infancy, and in consequence must face significant challenges, namely related to the necessity to work in the absence of sacrificial reagents, to

extend the usable wavelengths towards the visible fraction of the solar light spectra, and to increase the photonic efficiency of the photogenerated electron and hole charge carriers.

Advances should be the result of joint input of advanced operando/*in-situ* characterization and modeling/computational tools. Time-resolved techniques should be further applied for unraveling the surface mechanisms and getting full understanding of the key physico-chemical properties of the photocatalysts driving the performances in H_2O_2 synthesis.

By gathering a wide span of photocatalytic materials and of synthetic strategies, we hope that this article can inspire interdisciplinary research for designing the next generation of single- or multi-component photocatalytic materials with enhanced photonic efficiency towards selective artificial photosynthesis H_2O_2 and an optimized use of the solar spectra.

Declarations' section:

Competing Interests:

Authors declare no competing interests.

Funding:

Research grant awarded to Laura Valenzuela by the program Make Our Planet Great Again from the French Ministry for Europe and Foreign Affairs and the French Ministry for Higher Education and Research.

Author contributions:

Conceptualization of the review: Patricia Garcia-Munoz, Nicolas Keller; Literature search: Laura Valenzuela, Patricia Garcia-Munoz, Deborah Wegstein, Tobias Schanz, Girlie Eunice Lopez, Nicolas Keller; Data analysis: Laura Valenzuela, Patricia Garcia-Munoz, Girlie Eunice Lopez, Jonathan Z. Bloh, Nicolas Keller; Writing - original draft preparation: Laura Valenzuela,

Patricia Garcia-Munoz, Deborah Wegstein, Tobias Schanz, Girlie Eunice Lopez, Agnieszka M. Ruppert, Hynd Remita, Jonathan Z. Bloh, Nicolas Keller; Critical revision of the work: Laura Valenzuela, Patricia Garcia-Munoz, Agnieszka M. Ruppert, Hynd Remita, Jonathan Z. Bloh, Nicolas Keller; Funding acquisition: Jonathan Bloh, Hynd Remita, Laura Valenzuela, Nicolas Keller; Supervision: Nicolas Keller.

All authors read and approved the final manuscript.

References

1. Campos-Martin JM, Blanco-Brieva G, Fierro JLG (2006) Hydrogen Peroxide Synthesis: An Outlook beyond the Anthraquinone Process. Angew. Chem., Int. Ed. 45: 6962-6984. https://doi.org/10.1002/anie.200503779
2. Kosaka K, Yamada H, Shishida K, Echigo S, Minear RA, Tsuno H, Matsui S (2001) Evaluation of the treatment performance of a multistage ozone/hydrogen peroxide process by decomposition by-products. Water Res. 35: 3587-3594. https://doi.org/10.1016/S0043-1354(01)00087-2
3. Hu Y, Dong C, Wang T, Luo G (2018) Cyclohexanone ammoximation over TS-1 catalyst without organic solvent in a microreaction system. Chem. Eng. Sci. 187: 60-66. https://doi.org/10.1016/j.ces.2018.04.044
4. Lin M, Xia C, Zhu B, Li H, Shu X (2016) Green and efficient epoxidation of propylene with hydrogen peroxide (HPPO process) catalyzed by hollow TS-1 zeolite: A 1.0kt/a pilot-scale study. Chem. Eng. J. 295: 370-375. https://doi.org/10.1016/j.cej.2016.02.072

5. Lu J, Zhang X, Bravo-Suárez JJ, Fujitani T, Oyama ST (2009) Effect of composition and promoters in Au/TS-1 catalysts for direct propylene epoxidation using H2 and O2. Catal. Today 147: 186-195. https://doi.org/10.1016/j.cattod.2008.09.005

6. Signorile M, Crocellà V, Damin A, Rossi B, Lamberti C, Bonino F, Bordiga S (2018) Effect of Ti Speciation on Catalytic Performance of TS-1 in the Hydrogen Peroxide to Propylene Oxide Reaction. J. Phys. Chem. C 122: 9021-9034. https://doi.org/10.1021/acs.jpcc.8b01401

7. Jennings SR, Dollhopf DJ, Inskeep WP (2000) Acid production from sulfide minerals using hydrogen peroxide weathering. Appl. Geochem. 15: 235-243. https://doi.org/10.1016/S0883-2927(99)00041-4

8. Samanta C (2008) Direct synthesis of hydrogen peroxide from hydrogen and oxygen: An overview of recent developments in the process. Appl. Catal., A: Gen. 350: 133-149. https://doi.org/10.1016/j.apcata.2008.07.043

9. Liu J, Zou Y, Jin B, Zhang K, Park JH (2019) Hydrogen Peroxide Production from Solar Water Oxidation. ACS Energy Lett. 4: 3018-3027. https://doi.org/10.1021/acsenergylett.9b02199

10. Hydrogen Peroxide Market - Global Industry Analysis (2018 - 2021) - Growth Trends and Market Forecast (2022 - 2026). Research and Markets (2022)

11. Thénard LJ (1818) Observations sur des nouvelles combinaisons entre l'oxigène et divers acides. Ann. Chim. Phys. 8: 306-312.

12. Ranganathan S, Sieber V (2018) Recent Advances in the Direct Synthesis of Hydrogen Peroxide Using Chemical Catalysis—A Review Catalysts, vol 8

13. Jones CW, Clark JH (1999) Introduction to the preparation and properties of hydrogen peroxide In: Jones CW, Clark JH (eds) Applications of Hydrogen Peroxide and Derivatives. The Royal Society of Chemistry p 1-36
14. Goor G (1992) Hydrogen Peroxide: Manufacture and Industrial Use for Production of Organic Chemicals In: Strukul G (ed) Catalytic Oxidations with Hydrogen Peroxide as Oxidant. Springer Netherlands, Dordrecht p 13-43
15. Goor G, Glunneber J, S J (2012) Hydrogen Peroxide Ullmann's Encyclopedia of Industrial Chemistry. Wiley-VCH: Weinheim
16. Thénard LJ (1818) Nouvelles observations sur les acides et les oxydes oxygénés. Ann. Chim. Phys. 9: 51-56.
17. Meidinger H (1853) Ueber voltametrische Messungen. Justus Liebigs Ann. Chem. 88: 57-81. https://doi.org/10.1002/jlac.18530880103
18. Berthelot M (1878) Sur la formation de l'eau oxygénée, de l'ozone et de l'acide persulfurique pendant l'électrolyse. C. R. l'Academie. Sci., Ser. II Univers 86: 71-76.
19. Manchot W (1901) Ueber Sauerstoffactivirung. Justus Liebigs Ann. Chem. 314: 177-199. https://doi.org/10.1002/jlac.19013140117
20. Manchot W, Herzog J (1901) Ueber die Oxydation des Indigweisses durch Sauerstoffgas. Justus Liebigs Ann. Chem. 316: 318-330. https://doi.org/10.1002/jlac.19013160305
21. Manchot W, Herzog J (1901) Die Autoxydation des Hydrazobenzols. Justus Liebigs Ann. Chem. 316: 331-332. https://doi.org/10.1002/jlac.19013160306
22. Comyns AE (2007) Encyclopedic dictionary of named processes in chemical technology. CRC Press: Boca Raton, FL

23. Wendt H, Kreysa G (1999) Industrial processes In: Wendt H, Kreysa G (eds) Electrochemical Engineering: Science Technology in Chemical Other Industries. Springer: Berlin/Heidelberg p 290-369
24. Henkel H, Weber W (1914) Manufacture of hydrogen peroxid. U. S. Patent, United States
25. Walton JH, Filson GW (1932) The direct preparation of hydrogen peroxide in a high concentration. J. Am. Chem. Soc. 54: 3228-3229. https://doi.org/10.1021/ja01347a026
26. Von Schickh O (1960) Herstellung von Peroxyden durch Autoxydation. Geschichtliche Entwicklung. Chem. Ing. Tech 32: 462-462. https://doi.org/10.1002/cite.330320707
27. Hans-Joachim R, Georg P (1939) Production of hydrogen peroxide. U. S. Patent, United States
28. Rust FF, Porter LM (1959) Manufacture of hydrogen peroxide. U. S. Patent, United States
29. Hou H, Zeng X, Zhang X (2020) Production of Hydrogen Peroxide by Photocatalytic Processes. Angew. Chem., Int. Ed. 59: 17356-17376. https://doi.org/10.1002/anie.201911609
30. Roberts HC (1949) Production of hydrogen peroxide by the partial oxidation of alcohols. U. S. Patent
31. Rust FF (1955) (N. V. de Bataafsche Petroleum Maatschappij). [Chem. Abstr.] 53: 3613.
32. Leyshon D, Jones R, Cochran R (1993) Production of hydrogen peroxide. U. S. Patent
33. Padilla-Polo A (1997), University of Alcalá (Spain)
34. James TH, Weissberger A (1938) Oxidation processes. XI. The autoxidation of durohydroquinone. J. Amer. Chem. Soc. 60: 98-104.
35. Chinta S, Lunsford JH (2004) A mechanistic study of H2O2 and H2O formation from H2 and O2 catalyzed by palladium in an aqueous medium. J. Catal. 225: 249-255. https://doi.org/10.1016/j.jcat.2004.04.014

36. Dissanayake DP, Lunsford JH (2003) The direct formation of H2O2 from H2 and O2 over colloidal palladium. J. Catal. 214: 113-120. https://doi.org/10.1016/S0021-9517(02)00171-9

37. Lousada CM, Johansson AJ, Brinck T, Jonsson M (2013) Reactivity of metal oxide clusters with hydrogen peroxide and water – a DFT study evaluating the performance of different exchange–correlation functionals. Phys. Chem. Chem. Phys. 15: 5539-5552. https://doi.org/10.1039/C3CP44559C

38. Lewis RJ, Hutchings GJ (2019) Recent Advances in the Direct Synthesis of H2O2. ChemCatChem 11: 298-308. https://doi.org/10.1002/cctc.201801435

39. Ntainjua N E, Piccinini M, Pritchard JC, Edwards JK, Carley AF, Moulijn JA, Hutchings GJ (2009) Effect of Halide and Acid Additives on the Direct Synthesis of Hydrogen Peroxide using Supported Gold–Palladium Catalysts. ChemSusChem 2: 575-580. https://doi.org/10.1002/cssc.200800257

40. Wilson NM, Flaherty DW (2016) Mechanism for the Direct Synthesis of H2O2 on Pd Clusters: Heterolytic Reaction Pathways at the Liquid–Solid Interface. J. Am. Chem. Soc. 138: 574-586. https://doi.org/10.1021/jacs.5b10669

41. Landon P, Collier PJ, Papworth AJ, Kiely CJ, Hutchings GJ (2002) Direct formation of hydrogen peroxide from H2/O2 using a gold catalyst. Chem. Comm.: 2058-2059. https://doi.org/10.1039/B205248M

42. Okumura M, Kitagawa Y, Yamagcuhi K, Akita T, Tsubota S, Haruta M (2003) Direct Production of Hydrogen Peroxide from H2 and O2 over Highly Dispersed Au catalysts. Chem. Lett. 32: 822-823. https://doi.org/10.1246/cl.2003.822

43. Mul G, Zwijnenburg A, van der Linden B, Makkee M, Moulijn JA (2001) Stability and Selectivity of Au/TiO2 and Au/TiO2/SiO2 Catalysts in Propene Epoxidation: An in Situ FT-IR Study. J. Catal. 201: 128-137. https://doi.org/10.1006/jcat.2001.3239

44. Choudhary VR, Gaikwad AG, Sansare SD (2001) Nonhazardous Direct Oxidation of Hydrogen to Hydrogen Peroxide Using a Novel Membrane Catalyst. Angew. Chem., Int. Ed. 40: 1776-1779. https://doi.org/10.1002/1521-3773(20010504)40:9<1776::AID-ANIE17760>3.0.CO;2-C

45. Yang Y, Zhang C, Huang D, Zeng G, Huang J, Lai C, Zhou C, Wang W, Guo H, Xue W, Deng R, Cheng M, Xiong W (2019) Boron nitride quantum dots decorated ultrathin porous g-C3N4: Intensified exciton dissociation and charge transfer for promoting visible-light-driven molecular oxygen activation. Appl. Catal., B: Environ. 245: 87-99. https://doi.org/10.1016/j.apcatb.2018.12.049

46. Shiraishi Y, Kanazawa S, Sugano Y, Tsukamoto D, Sakamoto H, Ichikawa S, Hirai T (2014) Highly Selective Production of Hydrogen Peroxide on Graphitic Carbon Nitride (g-C3N4) Photocatalyst Activated by Visible Light. ACS Catal. 4: 774-780. https://doi.org/10.1021/cs401208c

47. Burek BO, Bahnemann DW, Bloh JZ (2019) Modeling and Optimization of the Photocatalytic Reduction of Molecular Oxygen to Hydrogen Peroxide over Titanium Dioxide. ACS Catal. 9: 25-37. https://doi.org/10.1021/acscatal.8b03638

48. Marquette CA, Blum LJ (2006) Applications of the luminol chemiluminescent reaction in analytical chemistry. Anal. Bioanal. Chem. 385: 546-554. https://doi.org/10.1007/s00216-006-0439-9

49. Lu Z, Chen G, Siahrostami S, Chen Z, Liu K, Xie J, Liao L, Wu T, Lin D, Liu Y, Jaramillo TF, Nørskov JK, Cui Y (2018) High-efficiency oxygen reduction to hydrogen peroxide

catalysed by oxidized carbon materials. Nat. Catal. 1: 156-162. https://doi.org/10.1038/s41929-017-0017-x

50. KG M-NGC Quantofix®Peroxide 100 Documentation

51. Gill TM, Zheng X (2020) Comparing Methods for Quantifying Electrochemically Accumulated H2O2. Chem. Mater. 32: 6285-6294. https://doi.org/10.1021/acs.chemmater.0c02010

52. Klassen NV, Marchington D, McGowan HCE (1994) H2O2 Determination by the I3- Method and by KMnO4 Titration. Anal. Chem. 66: 2921-2925. https://doi.org/10.1021/ac00090a020

53. Abutaha N, Hezam A, Almekhlafi FA, Saeed AMN, Namratha K, Byrappa K (2020) Rational design of Ag-ZnO-Fe3O4 nanocomposite with promising antimicrobial activity under LED light illumination. Appl. Surf. Sci. 527: 146893. https://doi.org/10.1016/j.apsusc.2020.146893

54. Gordon G, Cooper WJ, Rice RG, Pacey GE (1988) Methods of Measuring Disinfectant Residuals. Journal AWWA 80: 94-108. https://doi.org/10.1002/j.1551-8833.1988.tb03104.x

55. Nosaka Y, Nosaka AY (2017) Generation and Detection of Reactive Oxygen Species in Photocatalysis. Chem. Rev. 117: 11302-11336. https://doi.org/10.1021/acs.chemrev.7b00161

56. Bader H, Sturzenegger V, Hoigné J (1988) Photometric method for the determination of low concentrations of hydrogen peroxide by the peroxidase catalyzed oxidation of N,N-diethyl-p-phenylenediamine (DPD). Water Res. 22: 1109-1115. https://doi.org/10.1016/0043-1354(88)90005-X

57. Chen L, Chen C, Yang Z, Li S, Chu C, Chen B (2021) Simultaneously Tuning Band Structure and Oxygen Reduction Pathway toward High-Efficient Photocatalytic Hydrogen Peroxide Production Using Cyano-Rich Graphitic Carbon Nitride. Adv. Funct. Mater. 31: 2105731. https://doi.org/10.1002/adfm.202105731

58. Xiao J, Wang M, Pang Z, Dai L, Lu J, Zou J (2019) Simultaneous spectrophotometric determination of peracetic acid and the coexistent hydrogen peroxide using potassium iodide as the indicator. Anal. Methods 11: 1930-1938. https://doi.org/10.1039/C8AY02772B

59. Fuku K, Miyase Y, Miseki Y, Gunji T, Sayama K (2016) Enhanced Oxidative Hydrogen Peroxide Production on Conducting Glass Anodes Modified with Metal Oxides. ChemistrySelect 1: 5721-5726. https://doi.org/10.1002/slct.201601469

60. Wei Y, Zhang J, Zheng Q, Miao J, Alvarez PJ, Long M (2021) Quantification of photocatalytically-generated hydrogen peroxide in the presence of organic electron donors: Interference and reliability considerations. Chemosphere 279: 130556. https://doi.org/10.1016/j.chemosphere.2021.130556

61. Kosaka K, Yamada H, Matsui S, Echigo S, Shishida K (1998) Comparison among the Methods for Hydrogen Peroxide Measurements To Evaluate Advanced Oxidation Processes: Application of a Spectrophotometric Method Using Copper(II) Ion and 2,9-Dimethyl-1,10-phenanthroline. Environ. Sci. Technol. 32: 3821-3824. https://doi.org/10.1021/es9800784

62. Pérez JF, Sáez C, Llanos J, Cañizares P, López C, Rodrigo MA (2017) Improving the Efficiency of Carbon Cloth for the Electrogeneration of H2O2: Role of Polytetrafluoroethylene and Carbon Black Loading. Ind. Eng. Chem. Res. 56: 12588-12595. https://doi.org/10.1021/acs.iecr.7b02563

63. Kim K, Park J, Kim H, Jung GY, Kim M-G (2019) Solid-Phase Photocatalysts: Physical Vapor Deposition of Au Nanoislands on Porous TiO2 Films for Millimolar H2O2 Production within a Few Minutes. ACS Catal. 9: 9206-9211. https://doi.org/10.1021/acscatal.9b02269

64. Brandhuber PK, G. V. Methods for the Detection of Residual Concentrations of Hydrogen Peroxide in Advanced Oxidation Processes Project REUSE-04-19. Alexandria, VA: WateReuse Research Foundation

65. Wang M, Qiu S, Yang H, Huang Y, Dai L, Zhang B, Zou J (2021) Spectrophotometric determination of hydrogen peroxide in water with peroxidase-catalyzed oxidation of potassium iodide and its applications to hydroxylamine-involved Fenton and Fenton-like systems. Chemosphere 270: 129448. https://doi.org/10.1016/j.chemosphere.2020.129448

66. Miller WL, Kester DR (1988) Hydrogen peroxide measurement in seawater by (p-hydroxyphenyl)acetic acid dimerization. Anal. Chem. 60: 2711-2715. https://doi.org/10.1021/ac00175a014

67. Schick R, Strasser I, Stabel H-H (1997) Fluorometric determination of low concentrations of H2O2 in water: Comparison with two other methods and application to environmental samples and drinking-water treatment. Water Res. 31: 1371-1378. https://doi.org/10.1016/S0043-1354(96)00410-1

68. Sandri F, Danieli M, Zecca M, Centomo P (2021) Comparing Catalysts of the Direct Synthesis of Hydrogen Peroxide in Organic Solvent: is the Measure of the Product an Issue? ChemCatChem 13: 2653-2663. https://doi.org/10.1002/cctc.202100306

69. Pang Y, Xie H, Sun Y, Titirici M-M, Chai G-L (2020) Electrochemical oxygen reduction for H2O2 production: catalysts, pH effects and mechanisms. J. Mater. Chem. 8: 24996-25016. https://doi.org/10.1039/D0TA09122G

70. Zhao H, Yuan Z-Y (2021) Design Strategies of Non-Noble Metal-Based Electrocatalysts for Two-Electron Oxygen Reduction to Hydrogen Peroxide. ChemSusChem 14: 1616-1633. https://doi.org/10.1002/cssc.202100055

71. Domínguez-Henao L, Turolla A, Monticelli D, Antonelli M (2018) Assessment of a colorimetric method for the measurement of low concentrations of peracetic acid and hydrogen peroxide in water. Talanta 183: 209-215. https://doi.org/10.1016/j.talanta.2018.02.078

72. Schanz T, Burek B, Bloh J (2023) Fate and Reactivity of Peroxides formed over BiVO4 Anodes in Bicarbonate Electrolytes. Energy Lett. 2023, 8, XXX, 1463–1467. https://doi.org/10.1021/acsenergylett.3c00227

73. Burek BO, de Boer SR, Tieves F, Zhang W, van Schie M, Bormann S, Alcalde M, Holtmann D, Hollmann F, Bahnemann DW, Bloh JZ (2019) Photoenzymatic Hydroxylation of Ethylbenzene Catalyzed by Unspecific Peroxygenase: Origin of Enzyme Inactivation and the Impact of Light Intensity and Temperature. ChemCatChem 11: 3093-3100. https://doi.org/10.1002/cctc.201900610

74. Beranek R (2019) Selectivity of Chemical Conversions: Do Light-Driven Photoelectrocatalytic Processes Hold Special Promise? Angew. Chem., Int. Ed. 58: 16724-16729. https://doi.org/10.1002/anie.201908654

75. Nosaka Y, Takahashi S, Sakamoto H, Nosaka AY (2011) Reaction Mechanism of Cu(II)-Grafted Visible-Light Responsive TiO2 and WO3 Photocatalysts Studied by Means of ESR

Spectroscopy and Chemiluminescence Photometry. J. Phys. Chem. C 115: 21283-21290. https://doi.org/10.1021/jp2070634

76. Kim H-i, Choi Y, Hu S, Choi W, Kim J-H (2018) Photocatalytic hydrogen peroxide production by anthraquinone-augmented polymeric carbon nitride. Appl. Catal., B: Environ. 229: 121-129. https://doi.org/10.1016/j.apcatb.2018.01.060

77. Cervantes-González J, Vosburg DA, Mora-Rodriguez SE, Vázquez MA, Zepeda LG, Villegas Gómez C, Lagunas-Rivera S (2020) Anthraquinones: Versatile Organic Photocatalysts. ChemCatChem 12: 3811-3827. https://doi.org/10.1002/cctc.202000376

78. Bloh JZ (2021) Intensification of Heterogeneous Photocatalytic Reactions Without Efficiency Losses: The Importance of Surface Catalysis. Catal. Lett. 151: 3105-3113. https://doi.org/10.1007/s10562-021-03573-0

79. Narita E, Lawson F, Han KN (1983) Solubility of oxygen in aqueous electrolyte solutions. Hydrometallurgy 10: 21-37. https://doi.org/10.1016/0304-386X(83)90074-9

80. Liu Z, Sheng X, Wang D, Feng X (2019) Efficient Hydrogen Peroxide Generation Utilizing Photocatalytic Oxygen Reduction at a Triphase Interface. iScience 17: 67-73. https://doi.org/10.1016/j.isci.2019.06.023

81. Siahrostami S, Li G-L, Viswanathan V, Nørskov JK (2017) One- or Two-Electron Water Oxidation, Hydroxyl Radical, or H2O2 Evolution. J. Phys. Chem. Lett. 8: 1157-1160. https://doi.org/10.1021/acs.jpclett.6b02924

82. Viswanathan V, Hansen HA, Nørskov JK (2015) Selective Electrochemical Generation of Hydrogen Peroxide from Water Oxidation. J. Phys. Chem. Lett. 6: 4224-4228. https://doi.org/10.1021/acs.jpclett.5b02178

83. Fuku K, Sayama K (2016) Efficient oxidative hydrogen peroxide production and accumulation in photoelectrochemical water splitting using a tungsten trioxide/bismuth

vanadate photoanode. Chem. Comm. 52: 5406-5409. https://doi.org/10.1039/C6CC01605G

84. Kelly SR, Shi X, Back S, Vallez L, Park SY, Siahrostami S, Zheng X, Nørskov JK (2019) ZnO As an Active and Selective Catalyst for Electrochemical Water Oxidation to Hydrogen Peroxide. ACS Catal. 9: 4593-4599. https://doi.org/10.1021/acscatal.8b04873

85. Park SY, Abroshan H, Shi X, Jung HS, Siahrostami S, Zheng X (2019) CaSnO3: An Electrocatalyst for Two-Electron Water Oxidation Reaction to Form H2O2. ACS Energy Lett. 4: 352-357. https://doi.org/10.1021/acsenergylett.8b02303

86. Shi X, Siahrostami S, Li G-L, Zhang Y, Chakthranont P, Studt F, Jaramillo TF, Zheng X, Nørskov JK (2017) Understanding activity trends in electrochemical water oxidation to form hydrogen peroxide. Nat. Commun. 8: 701. https://doi.org/10.1038/s41467-017-00585-6

87. Miyase Y, Takasugi S, Iguchi S, Miseki Y, Gunji T, Sasaki K, Fujita E, Sayama K (2018) Modification of BiVO4/WO3 composite photoelectrodes with Al2O3via chemical vapor deposition for highly efficient oxidative H2O2 production from H2O. Sustain. Energy Fuels 2: 1621-1629. https://doi.org/10.1039/C8SE00070K

88. Baek JH, Gill TM, Abroshan H, Park S, Shi X, Nørskov J, Jung HS, Siahrostami S, Zheng X (2019) Selective and Efficient Gd-Doped BiVO4 Photoanode for Two-Electron Water Oxidation to H2O2. ACS Energy Lett. 4: 720-728. https://doi.org/10.1021/acsenergylett.9b00277

89. Kuttassery F, Mathew S, Sagawa S, Remello SN, Thomas A, Yamamoto D, Onuki S, Nabetani Y, Tachibana H, Inoue H (2017) One Electron-Initiated Two-Electron Oxidation of Water by Aluminum Porphyrins with Earth's Most Abundant Metal. ChemSusChem 10: 1909-1915. https://doi.org/10.1002/cssc.201700322

90. Xia C, Back S, Ringe S, Jiang K, Chen F, Sun X, Siahrostami S, Chan K, Wang H (2020) Confined local oxygen gas promotes electrochemical water oxidation to hydrogen peroxide. Nat. Catal. 3: 125-134. https://doi.org/10.1038/s41929-019-0402-8

91. Mavrikis S, Göltz M, Rosiwal S, Wang L, Ponce de León C (2020) Boron-Doped Diamond Electrocatalyst for Enhanced Anodic H2O2 Production. ACS Appl. Energy Mater 3: 3169-3173. https://doi.org/10.1021/acsaem.0c00093

92. Miyase Y, Miseki Y, Gunji T, Sayama K (2020) Efficient H2O2 Production via H2O Oxidation on an Anode Modified with Sb-Containing Mixed Metal Oxides. ChemElectroChem 7: 2448-2455. https://doi.org/10.1002/celc.202000276

93. Baek J, Jin Q, Johnson NS, Jiang Y, Ning R, Mehta A, Siahrostami S, Zheng X (2022) Discovery of LaAlO3 as an efficient catalyst for two-electron water electrolysis towards hydrogen peroxide. Nat. Commun. 13: 7256. https://doi.org/10.1038/s41467-022-34884-4

94. Fan L, Bai X, Xia C, Zhang X, Zhao X, Xia Y, Wu Z-Y, Lu Y, Liu Y, Wang H (2022) CO2/carbonate-mediated electrochemical water oxidation to hydrogen peroxide. Nat. Commun. 13: 2668. https://doi.org/10.1038/s41467-022-30251-5

95. Gill TM, Vallez L, Zheng X (2021) Enhancing Electrochemical Water Oxidation toward H2O2 via Carbonaceous Electrolyte Engineering. ACS Appl. Energy Mater 4: 12429-12435. https://doi.org/10.1021/acsaem.1c02258

96. Gill TM, Vallez L, Zheng X (2021) The Role of Bicarbonate-Based Electrolytes in H2O2 Production through Two-Electron Water Oxidation. ACS Energy Lett. 6: 2854-2862. https://doi.org/10.1021/acsenergylett.1c01264

97. Richardson DE, Yao H, Frank KM, Bennett DA (2000) Equilibria, Kinetics, and Mechanism in the Bicarbonate Activation of Hydrogen Peroxide: Oxidation of Sulfides by

Peroxymonocarbonate. J. Am. Chem. Soc. 122: 1729-1739. https://doi.org/10.1021/ja9927467

98. Kormann C, Bahnemann DW, Hoffmann MR (1988) Photocatalytic production of hydrogen peroxides and organic peroxides in aqueous suspensions of titanium dioxide, zinc oxide, and desert sand. Environ. Sci. Technol. 22: 798-806. https://doi.org/10.1021/es00172a009

99. Riente P, Fianchini M, Llanes P, Pericàs MA, Noël T (2021) Shedding light on the nature of the catalytically active species in photocatalytic reactions using Bi2O3 semiconductor. Nat. Commun. 12: 625. https://doi.org/10.1038/s41467-020-20882-x

100. Schuchmann H-P, Sonntag Cv (1984) Methylperoxyl Radicals: A Study of the γ-Radiolysis of Methane in Oxygenated Aqueous Solutions. 39: 217-221. https://doi.org/10.1515/znb-1984-0217

101. Dilla M, Mateblowski A, Ristig S, Strunk J (2017) Photocatalytic CO2 Reduction under Continuous Flow High-Purity Conditions: Influence of Light Intensity and H2O Concentration. ChemCatChem 9: 4345-4352. https://doi.org/10.1002/cctc.201701189

102. Takeuchi S, Takashima M, Takase M, Ohtani B (2018) Digitally Controlled Kinetics of Titania-photocatalyzed Oxygen Evolution. Chem. Lett. 47: 373-376. https://doi.org/10.1246/cl.171093

103. Bloh JZ (2019) A Holistic Approach to Model the Kinetics of Photocatalytic Reactions. Front. Chem. 7. https://doi.org/10.3389/fchem.2019.00128

104. Burek BO, Sutor A, Bahnemann DW, Bloh JZ (2017) Completely integrated wirelessly-powered photocatalyst-coated spheres as a novel means to perform heterogeneous photocatalytic reactions. Catal. Sci. Technol. 7: 4977-4983. https://doi.org/10.1039/C7CY01537B

105. Moon G-h, Kim W, Bokare AD, Sung N-e, Choi W (2014) Solar production of H2O2 on reduced graphene oxide–TiO2 hybrid photocatalysts consisting of earth-abundant elements only. Energy Environ. Sci. 7: 4023-4028. https://doi.org/10.1039/C4EE02757D

106. Moon G-h, Fujitsuka M, Kim S, Majima T, Wang X, Choi W (2017) Eco-Friendly Photochemical Production of H2O2 through O2 Reduction over Carbon Nitride Frameworks Incorporated with Multiple Heteroelements. ACS Catal. 7: 2886-2895. https://doi.org/10.1021/acscatal.6b03334

107. Teranishi M, Naya S-i, Tada H (2016) Temperature- and pH-Dependence of Hydrogen Peroxide Formation from Molecular Oxygen by Gold Nanoparticle-Loaded Titanium(IV) Oxide Photocatalyst. J. Phys. Chem. C 120: 1083-1088. https://doi.org/10.1021/acs.jpcc.5b10626

108. Goto H, Hanada Y, Ohno T, Matsumura M (2004) Quantitative analysis of superoxide ion and hydrogen peroxide produced from molecular oxygen on photoirradiated TiO2 particles. J. Catal. 225: 223-229. https://doi.org/10.1016/j.jcat.2004.04.001

109. Hykaway N, Sears WM, Morisaki H, Morrison SR (1986) Current-doubling reactions on titanium dioxide photoanodes. J. Phys. Chem. 90: 6663-6667. https://doi.org/10.1021/j100283a014

110. Burek BO, Timm J, Bahnemann DW, Bloh JZ (2019) Kinetic effects and oxidation pathways of sacrificial electron donors on the example of the photocatalytic reduction of molecular oxygen to hydrogen peroxide over illuminated titanium dioxide. Catal. Today 335: 354-364. https://doi.org/10.1016/j.cattod.2018.12.044

111. Shiraishi Y, Kanazawa S, Tsukamoto D, Shiro A, Sugano Y, Hirai T (2013) Selective Hydrogen Peroxide Formation by Titanium Dioxide Photocatalysis with Benzylic Alcohols

and Molecular Oxygen in Water. ACS Catal. 3: 2222-2227. https://doi.org/10.1021/cs400511q

112. Baran T, Wojtyła S, Minguzzi A, Rondinini S, Vertova A (2019) Achieving efficient H2O2 production by a visible-light absorbing, highly stable photosensitized TiO2. Appl. Catal., B: Environ. 244: 303-312. https://doi.org/10.1016/j.apcatb.2018.11.044

113. Xiong X, Zhang X, Liu S, Zhao J, Xu Y (2018) Sustained production of H2O2 in alkaline water solution using borate and phosphate-modified Au/TiO2 photocatalysts. Photochem. Photobiol. Sci. 17: 1018-1022. https://doi.org/10.1039/C8PP00177D

114. Xu J, Dai G, Chen B, He D, Situ Y, Huang H (2020) Construction of Ti3+-TiO2-C3N4por compound coupling photocatalysis and Fenton-like process: Self-driven Fenton-like process without extra H2O2 addition. Chemosphere 241: 125022. https://doi.org/10.1016/j.chemosphere.2019.125022

115. Zhang J, Zheng L, Wang F, Chen C, Wu H, Leghari SAK, Long M (2020) The critical role of furfural alcohol in photocatalytic H2O2 production on TiO2. Appl. Catal., B: Environ. 269: 118770. https://doi.org/10.1016/j.apcatb.2020.118770

116. Zhang Y, Simon KA, Andrew AA, Del Vecchio R, Blough NV (2014) Enhanced Photoproduction of Hydrogen Peroxide by Humic Substances in the Presence of Phenol Electron Donors. Environ. Sci. Technol. 48: 12679-12688. https://doi.org/10.1021/es5035798

117. Zheng L, Su H, Zhang J, Walekar LS, Vafaei Molamahmood H, Zhou B, Long M, Hu YH (2018) Highly selective photocatalytic production of H2O2 on sulfur and nitrogen co-doped graphene quantum dots tuned TiO2. Appl. Catal., B: Environ. 239: 475-484. https://doi.org/10.1016/j.apcatb.2018.08.031

118. Maurino V, Minero C, Pelizzetti E, Mariella G, Arbezzano A, Rubertelli F (2007) Influence of Zn(II) adsorption on the photocatalytic activity and the production of H2O2 over irradiated TiO2. Res. Chem. Intermed. 33: 319-332. https://doi.org/10.1163/156856707779238711

119. Maurino V, Minero C, Mariella G, Pelizzetti E (2005) Sustained production of H2O2 on irradiated TiO2 – fluoride systems. Chem. Comm.: 2627-2629. https://doi.org/10.1039/B418789J

120. Tsukamoto D, Shiro A, Shiraishi Y, Sugano Y, Ichikawa S, Tanaka S, Hirai T (2012) Photocatalytic H2O2 Production from Ethanol/O2 System Using TiO2 Loaded with Au–Ag Bimetallic Alloy Nanoparticles. ACS Catal. 2: 599-603. https://doi.org/10.1021/cs2006873

121. Wang L, Cao S, Guo K, Wu Z, Ma Z, Piao L (2019) Simultaneous hydrogen and peroxide production by photocatalytic water splitting. Chinese J. Catal. 40: 470-475. https://doi.org/10.1016/S1872-2067(19)63274-2

122. Teranishi M, Naya S-i, Tada H (2010) In Situ Liquid Phase Synthesis of Hydrogen Peroxide from Molecular Oxygen Using Gold Nanoparticle-Loaded Titanium(IV) Dioxide Photocatalyst. J. Am. Chem. Soc. 132: 7850-7851. https://doi.org/10.1021/ja102651g

123. Zeng X, Wang Z, Meng N, McCarthy DT, Deletic A, Pan J-h, Zhang X (2017) Highly dispersed TiO2 nanocrystals and carbon dots on reduced graphene oxide: Ternary nanocomposites for accelerated photocatalytic water disinfection. Appl. Catal., B: Environ. 202: 33-41. https://doi.org/10.1016/j.apcatb.2016.09.014

124. Ma R, Wang L, Wang H, Liu Z, Xing M, Zhu L, Meng X, Xiao F-S (2019) Solid acids accelerate the photocatalytic hydrogen peroxide synthesis over a hybrid catalyst of

titania nanotube with carbon dot. Applied Catalysis B: Environmental 244: 594-603. https://doi.org/10.1016/j.apcatb.2018.11.087

125. Zuo G, Li B, Guo Z, Wang L, Yang F, Hou W, Zhang S, Zong P, Liu S, Meng X, Du Y, Wang T, Roy VAL (2019) Efficient Photocatalytic Hydrogen Peroxide Production over TiO2 Passivated by SnO2 Catalysts, vol 9

126. Zheng L, Zhang J, Hu YH, Long M (2019) Enhanced Photocatalytic Production of H2O2 by Nafion Coatings on S,N-Codoped Graphene-Quantum-Dots-Modified TiO2. J. Phys. Chem. C 123: 13693-13701. https://doi.org/10.1021/acs.jpcc.9b02311

127. Low J, Cao S, Yu J, Wageh S (2014) Two-dimensional layered composite photocatalysts. Chem. Comm. 50: 10768-10777. https://doi.org/10.1039/C4CC02553A

128. Ong W-J, Tan L-L, Ng YH, Yong S-T, Chai S-P (2016) Graphitic Carbon Nitride (g-C3N4)-Based Photocatalysts for Artificial Photosynthesis and Environmental Remediation: Are We a Step Closer To Achieving Sustainability? Chem. Rev. 116: 7159-7329. https://doi.org/10.1021/acs.chemrev.6b00075

129. Wang X, Blechert S, Antonietti M (2012) Polymeric Graphitic Carbon Nitride for Heterogeneous Photocatalysis. ACS Catal. 2: 1596-1606. https://doi.org/10.1021/cs300240x

130. Wang X, Maeda K, Thomas A, Takanabe K, Xin G, Carlsson JM, Domen K, Antonietti M (2009) A metal-free polymeric photocatalyst for hydrogen production from water under visible light. Nat. Mater. 8: 76-80. https://doi.org/10.1038/nmat2317

131. Che W, Cheng W, Yao T, Tang F, Liu W, Su H, Huang Y, Liu Q, Liu J, Hu F, Pan Z, Sun Z, Wei S (2017) Fast Photoelectron Transfer in (Cring)–C3N4 Plane Heterostructural Nanosheets for Overall Water Splitting. J. Am. Chem. Soc. 139: 3021-3026. https://doi.org/10.1021/jacs.6b11878

132. Deng Q-F, Liu L, Lin X-Z, Du G, Liu Y, Yuan Z-Y (2012) Synthesis and CO2 capture properties of mesoporous carbon nitride materials. Chem. Eng. J. 203: 63-70. https://doi.org/10.1016/j.cej.2012.06.124

133. Hu S, Chen X, Li Q, Li F, Fan Z, Wang H, Wang Y, Zheng B, Wu G (2017) Fe3+ doping promoted N2 photofixation ability of honeycombed graphitic carbon nitride: The experimental and density functional theory simulation analysis. Appl. Catal., B: Environ. 201: 58-69. https://doi.org/10.1016/j.apcatb.2016.08.002

134. Li S, Dong G, Hailili R, Yang L, Li Y, Wang F, Zeng Y, Wang C (2016) Effective photocatalytic H2O2 production under visible light irradiation at g-C3N4 modulated by carbon vacancies. Appl. Catal., B: Environ. 190: 26-35. https://doi.org/10.1016/j.apcatb.2016.03.004

135. Lima MJ, Silva AMT, Silva CG, Faria JL (2017) Graphitic carbon nitride modified by thermal, chemical and mechanical processes as metal-free photocatalyst for the selective synthesis of benzaldehyde from benzyl alcohol. J. Catal. 353: 44-53. https://doi.org/10.1016/j.jcat.2017.06.030

136. Lu D, Wang H, Zhao X, Kondamareddy KK, Ding J, Li C, Fang P (2017) Highly Efficient Visible-Light-Induced Photoactivity of Z-Scheme g-C3N4/Ag/MoS2 Ternary Photocatalysts for Organic Pollutant Degradation and Production of Hydrogen. ACS Sustain. Chem. Eng. 5: 1436-1445. https://doi.org/10.1021/acssuschemeng.6b02010

137. Moreira NFF, Sampaio MJ, Ribeiro AR, Silva CG, Faria JL, Silva AMT (2019) Metal-free g-C3N4 photocatalysis of organic micropollutants in urban wastewater under visible light. Appl. Catal., B: Environ. 248: 184-192. https://doi.org/10.1016/j.apcatb.2019.02.001

138. Mishra A, Mehta A, Basu S, Shetti NP, Reddy KR, Aminabhavi TM (2019) Graphitic carbon nitride (g–C3N4)–based metal-free photocatalysts for water splitting: A review. Carbon 149: 693-721. https://doi.org/10.1016/j.carbon.2019.04.104

139. Huang D, Li Z, Zeng G, Zhou C, Xue W, Gong X, Yan X, Chen S, Wang W, Cheng M (2019) Megamerger in photocatalytic field: 2D g-C3N4 nanosheets serve as support of 0D nanomaterials for improving photocatalytic performance. Appl. Catal., B: Environ. 240: 153-173. https://doi.org/10.1016/j.apcatb.2018.08.071

140. Wen J, Xie J, Chen X, Li X (2017) A review on g-C3N4-based photocatalysts. Appl. Surf. Sci. 391: 72-123. https://doi.org/10.1016/j.apsusc.2016.07.030

141. Yang W, Zhang X, Xie Y (2016) Advances and challenges in chemistry of two-dimensional nanosheets. Nano Today 11: 793-816. https://doi.org/10.1016/j.nantod.2016.10.004

142. Gillan EG (2000) Synthesis of Nitrogen-Rich Carbon Nitride Networks from an Energetic Molecular Azide Precursor. Chem. Mater. 12: 3906-3912. https://doi.org/10.1021/cm000570y

143. Wang Y, Wang X, Antonietti M (2012) Polymeric Graphitic Carbon Nitride as a Heterogeneous Organocatalyst: From Photochemistry to Multipurpose Catalysis to Sustainable Chemistry. Angew. Chem., Int. Ed. 51: 68-89. https://doi.org/10.1002/anie.201101182

144. Du R, Xiao K, Li B, Han X, Zhang C, Wang X, Zuo Y, Guardia P, Li J, Chen J, Arbiol J, Cabot A (2022) Controlled oxygen doping in highly dispersed Ni-loaded g-C3N4 nanotubes for efficient photocatalytic H2O2 production. Chem. Eng. J. 441: 135999. https://doi.org/10.1016/j.cej.2022.135999

145. Torres-Pinto A, Sampaio MJ, Silva CG, Faria JL, Silva AMT (2019) Metal-free carbon nitride photocatalysis with in situ hydrogen peroxide generation for the degradation of

aromatic compounds. Appl. Catal., B: Environ. 252: 128-137. https://doi.org/10.1016/j.apcatb.2019.03.040

146. Wang K, Li Q, Liu B, Cheng B, Ho W, Yu J (2015) Sulfur-doped g-C3N4 with enhanced photocatalytic CO2-reduction performance. Appl. Catal., B: Environ. 176-177: 44-52. https://doi.org/10.1016/j.apcatb.2015.03.045
147. Wang Y, Hong J, Zhang W, Xu R (2013) Carbon nitride nanosheets for photocatalytic hydrogen evolution: remarkably enhanced activity by dye sensitization. Catal. Sci. Technol. 3: 1703-1711. https://doi.org/10.1039/C3CY20836B
148. Chen Z, Zhang S, Liu Y, Alharbi NS, Rabah SO, Wang S, Wang X (2020) Synthesis and fabrication of g-C3N4-based materials and their application in elimination of pollutants. Sci. Total Environ. 731: 139054. https://doi.org/10.1016/j.scitotenv.2020.139054
149. Wang J, Wang S (2022) A critical review on graphitic carbon nitride (g-C3N4)-based materials: Preparation, modification and environmental application. Coord. Chem. Rev. 453: 214338. https://doi.org/10.1016/j.ccr.2021.214338
150. Zhang Y, Liu J, Wu G, Chen W (2012) Porous graphitic carbon nitride synthesized via direct polymerization of urea for efficient sunlight-driven photocatalytic hydrogen production. Nanoscale 4: 5300-5303. https://doi.org/10.1039/C2NR30948C
151. Dong F, Zhao Z, Xiong T, Ni Z, Zhang W, Sun Y, Ho W-K (2013) In Situ Construction of g-C3N4/g-C3N4 Metal-Free Heterojunction for Enhanced Visible-Light Photocatalysis. ACS Appl. Mater. Interfaces 5: 11392-11401. https://doi.org/10.1021/am403653a
152. Xiao H, Wang W, Liu G, Chen Z, Lv K, Zhu J (2015) Photocatalytic performances of g-C3N4 based catalysts for RhB degradation: Effect of preparation conditions. Appl. Surf. Sci. 358: 313-318. https://doi.org/10.1016/j.apsusc.2015.07.213

153. Chen D, Wang K, Hong W, Zong R, Yao W, Zhu Y (2015) Visible light photoactivity enhancement via CuTCPP hybridized g-C3N4 nanocomposite. Appl. Catal., B: Environ. 166-167: 366-373. https://doi.org/10.1016/j.apcatb.2014.11.050

154. Dong F, Li Y, Wang Z, Ho W-K (2015) Enhanced visible light photocatalytic activity and oxidation ability of porous graphene-like g-C3N4 nanosheets via thermal exfoliation. Appl. Surf. Sci. 358: 393-403. https://doi.org/10.1016/j.apsusc.2015.04.034

155. Li X, Pi Y, Wu L, Xia Q, Wu J, Li Z, Xiao J (2017) Facilitation of the visible light-induced Fenton-like excitation of H2O2 via heterojunction of g-C3N4/NH2-Iron terephthalate metal-organic framework for MB degradation. Appl. Catal., B: Environ. 202: 653-663. https://doi.org/10.1016/j.apcatb.2016.09.073

156. Xie L, Ai Z, Zhang M, Sun R, Zhao W (2016) Enhanced Hydrogen Evolution in the Presence of Plasmonic Au-Photo-Sensitized g-C3N4 with an Extended Absorption Spectrum from 460 to 640 nm. PLOS ONE 11: e0161397. https://doi.org/10.1371/journal.pone.0161397

157. Hu S, Qu X, Li P, Wang F, Li Q, Song L, Zhao Y, Kang X (2018) Photocatalytic oxygen reduction to hydrogen peroxide over copper doped graphitic carbon nitride hollow microsphere: The effect of Cu(I)-N active sites. Chem. Eng. J. 334: 410-418. https://doi.org/10.1016/j.cej.2017.10.016

158. Shen L, Xing Z, Zou J, Li Z, Wu X, Zhang Y, Zhu Q, Yang S, Zhou W (2017) Black TiO2 nanobelts/g-C3N4 nanosheets Laminated Heterojunctions with Efficient Visible-Light-Driven Photocatalytic Performance. Sci. Rep. 7: 41978. https://doi.org/10.1038/srep41978

159. Wang Z, Huang Y, Chen M, Shi X, Zhang Y, Cao J, Ho W, Lee SC (2019) Roles of N-Vacancies over Porous g-C3N4 Microtubes during Photocatalytic NOx Removal. ACS Appl. Mater. Interfaces 11: 10651-10662. https://doi.org/10.1021/acsami.8b21987

160. Liang Y, Wu X, Liu X, Li C, Liu S (2022) Recovering solar fuels from photocatalytic CO2 reduction over W6+-incorporated crystalline g-C3N4 nanorods by synergetic modulation of active centers. Appl. Catal., B: Environ. 304: 120978. https://doi.org/10.1016/j.apcatb.2021.120978

161. Fu J, Yu J, Jiang C, Cheng B (2018) g-C3N4-Based Heterostructured Photocatalysts. Adv. Energy Mater. 8: 1701503. https://doi.org/10.1002/aenm.201701503

162. Mamba G, Mishra AK (2016) Graphitic carbon nitride (g-C3N4) nanocomposites: A new and exciting generation of visible light driven photocatalysts for environmental pollution remediation. Appl. Catal., B: Environ. 198: 347-377. https://doi.org/10.1016/j.apcatb.2016.05.052

163. Patnaik S, Sahoo DP, Parida K (2021) Recent advances in anion doped g-C3N4 photocatalysts: A review. Carbon 172: 682-711. https://doi.org/10.1016/j.carbon.2020.10.073

164. Dong X, Cheng F (2015) Recent development in exfoliated two-dimensional g-C3N4 nanosheets for photocatalytic applications. J. Mater. Chem. 3: 23642-23652. https://doi.org/10.1039/C5TA07374J

165. Shiraishi Y, Kanazawa S, Kofuji Y, Sakamoto H, Ichikawa S, Tanaka S, Hirai T (2014) Sunlight-Driven Hydrogen Peroxide Production from Water and Molecular Oxygen by Metal-Free Photocatalysts. Angew. Chem., Int. Ed. 53: 13454-13459. https://doi.org/10.1002/anie.201407938

166. Wood PM (1988) The potential diagram for oxygen at pH 7. Biochem. J. 253: 287-289. https://doi.org/10.1042/bj2530287

167. Yan SC, Lv SB, Li ZS, Zou ZG (2010) Organic–inorganic composite photocatalyst of g-C3N4 and TaON with improved visible light photocatalytic activities. Dalton Trans. 39: 1488-1491. https://doi.org/10.1039/B914110C

168. Torres-Pinto A, Sampaio MJ, Teixo J, Silva CG, Faria JL, Silva AMT (2020) Photo-Fenton degradation assisted by in situ generation of hydrogen peroxide using a carbon nitride photocatalyst. J. Water Process. Eng. 37: 101467. https://doi.org/10.1016/j.jwpe.2020.101467

169. Zhang M, Wang Q, Chen C, Zang L, Ma W, Zhao J (2009) Oxygen Atom Transfer in the Photocatalytic Oxidation of Alcohols by TiO2: Oxygen Isotope Studies. Angew. Chem., Int. Ed. 48: 6081-6084. https://doi.org/10.1002/anie.200900322

170. Shiraishi Y, Kofuji Y, Sakamoto H, Tanaka S, Ichikawa S, Hirai T (2015) Effects of Surface Defects on Photocatalytic H2O2 Production by Mesoporous Graphitic Carbon Nitride under Visible Light Irradiation. ACS Catal. 5: 3058-3066. https://doi.org/10.1021/acscatal.5b00408

171. Zhao L, Bacsik Z, Hedin N, Wei W, Sun Y, Antonietti M, Titirici M-M (2010) Carbon Dioxide Capture on Amine-Rich Carbonaceous Materials Derived from Glucose. ChemSusChem 3: 840-845. https://doi.org/10.1002/cssc.201000044

172. Liu B, Du J, Ke G, Jia B, Huang Y, He H, Zhou Y, Zou Z (2022) Boosting O2 Reduction and H2O Dehydrogenation Kinetics: Surface N-Hydroxymethylation of g-C3N4 Photocatalysts for the Efficient Production of H2O2. Adv. Funct. Mater. 32: 2111125. https://doi.org/10.1002/adfm.202111125

173. Liu W, Song C, Kou M, Wang Y, Deng Y, Shimada T, Ye L (2021) Fabrication of ultra-thin g-C3N4 nanoplates for efficient visible-light photocatalytic H2O2 production via two-

electron oxygen reduction. Chem. Eng. J. 425: 130615. https://doi.org/10.1016/j.cej.2021.130615

174. Zhang Z, Zheng Y, Xie H, Zhao J, Guo X, Zhang W, Fu Q, Wang S, Xu Q, Huang Y (2022) Synthesis of g-C3N4 microrods with superficial C, N dual vacancies for enhanced photocatalytic organic pollutant removal and H2O2 production. J. Alloys Compd. 904: 164028. https://doi.org/10.1016/j.jallcom.2022.164028
175. Wang R, Zhang X, Li F, Cao D, Pu M, Han D, Yang J, Xiang X (2018) Energy-level dependent H2O2 production on metal-free, carbon-content tunable carbon nitride photocatalysts. J. Energy Chem. 27: 343-350. https://doi.org/10.1016/j.jechem.2017.12.014
176. Wei Z, Liu M, Zhang Z, Yao W, Tan H, Zhu Y (2018) Efficient visible-light-driven selective oxygen reduction to hydrogen peroxide by oxygen-enriched graphitic carbon nitride polymers. Energy Environ. Sci. 11: 2581-2589. https://doi.org/10.1039/C8EE01316K
177. Bai J, Sun Y, Li M, Yang L, Li J (2018) The effect of phosphate modification on the photocatalytic H2O2 production ability of g-C3N4 catalyst prepared via acid-hydrothermal post-treatment. Diam. Relat. Mater. 87: 1-9. https://doi.org/10.1016/j.diamond.2018.05.004
178. Deng L, Sun J, Sun J, Wang X, Shen T, Zhao R, Zhang Y, Wang B (2022) Improved performance of photosynthetic H2O2 and photodegradation by K-, P-, O-, and S-co-doped g-C3N4 with enhanced charge transfer ability under visible light. Appl. Surf. Sci. 597: 153586. https://doi.org/10.1016/j.apsusc.2022.153586
179. Chu Y-C, Lin T-J, Lin Y-R, Chiu W-L, Nguyen B-S, Hu C (2020) Influence of P,S,O-Doping on g-C3N4 for hydrogel formation and photocatalysis: An experimental and theoretical study. Carbon 169: 338-348. https://doi.org/10.1016/j.carbon.2020.07.053

180. Feng C, Tang L, Deng Y, Wang J, Liu Y, Ouyang X, Yang H, Yu J, Wang J (2021) A novel sulfur-assisted annealing method of g-C3N4 nanosheet compensates for the loss of light absorption with further promoted charge transfer for photocatalytic production of H2 and H2O2. Appl. Catal., B: Environ. 281: 119539. https://doi.org/10.1016/j.apcatb.2020.119539

181. Liu Y, Zheng Y, Zhang W, Peng Z, Xie H, Wang Y, Guo X, Zhang M, Li R, Huang Y (2021) Template-free preparation of non-metal (B, P, S) doped g-C3N4 tubes with enhanced photocatalytic H2O2 generation. J. Mater. Sci. Technol. 95: 127-135. https://doi.org/10.1016/j.jmst.2021.03.025

182. Ding Y, Maitra S, Wang C, Zheng R, Zhang M, Barakat T, Roy S, Liu J, Li Y, Hasan T, Su B-L (2022) Hydrophilic bi-functional B-doped g-C3N4 hierarchical architecture for excellent photocatalytic H2O2 production and photoelectrochemical water splitting. J. Energy Chem. 70: 236-247. https://doi.org/10.1016/j.jechem.2022.02.031

183. Wang W, Zhang W, Cai Y, Wang Q, Deng J, Chen J, Jiang Z, Zhang Y, Yu C (2022) Introducing B—N unit boosts photocatalytic H2O2 production on metal-free g-C3N4 nanosheets. Nano Research. https://doi.org/10.1007/s12274-022-4976-0

184. Qu X, Hu S, Bai J, Li P, Lu G, Kang X (2018) Synthesis of band gap-tunable alkali metal modified graphitic carbon nitride with outstanding photocatalytic H2O2 production ability via molten salt method. J. Mater. Sci. Technol. 34: 1932-1938. https://doi.org/10.1016/j.jmst.2018.04.019

185. Gupta SK, Mao Y (2021) A review on molten salt synthesis of metal oxide nanomaterials: Status, opportunity, and challenge. Progress in Materials Science 117: 100734. https://doi.org/10.1016/j.pmatsci.2020.100734

186. Yang L, Dong G, Jacobs DL, Wang Y, Zang L, Wang C (2017) Two-channel photocatalytic production of H2O2 over g-C3N4 nanosheets modified with perylene imides. J. Catal. 352: 274-281. https://doi.org/10.1016/j.jcat.2017.05.010

187. Zhao Y, Zhang P, Yang Z, Li L, Gao J, Chen S, Xie T, Diao C, Xi S, Xiao B, Hu C, Choi W (2021) Mechanistic analysis of multiple processes controlling solar-driven H2O2 synthesis using engineered polymeric carbon nitride. Nat. Commun. 12: 3701. https://doi.org/10.1038/s41467-021-24048-1

188. Pan Y, Liu X, Zhang W, Shao B, Liu Z, Liang Q, Wu T, He Q, Huang J, Peng Z, Liu Y, Zhao C (2022) Bifunctional template-mediated synthesis of porous ordered g-C3N4 decorated with potassium and cyano groups for effective photocatalytic H2O2 evolution from dual-electron O2 reduction. Chem. Eng. J. 427: 132032. https://doi.org/10.1016/j.cej.2021.132032

189. Teng Z, Cai W, Sim W, Zhang Q, Wang C, Su C, Ohno T (2021) Photoexcited single metal atom catalysts for heterogeneous photocatalytic H2O2 production: Pragmatic guidelines for predicting charge separation. Appl. Catal., B: Environ. 282: 119589. https://doi.org/10.1016/j.apcatb.2020.119589

190. Chang X, Yang J, Han D, Zhang B, Xiang X, He J (2018) Enhancing Light-Driven Production of Hydrogen Peroxide by Anchoring Au onto C3N4 Catalysts Catalysts, vol 8

191. Ahmed MT, Abdullah H, Kuo D-H (2022) Highly efficient photocatalytic H2O2 generation over dysprosium oxide-integrated g-C3N4 nanosheets with nitrogen deficiency. Chemosphere 307: 135910. https://doi.org/10.1016/j.chemosphere.2022.135910

192. Chu C, Miao W, Li Q, Wang D, Liu Y, Mao S (2022) Highly efficient photocatalytic H2O2 production with cyano and SnO2 co-modified g-C3N4. Chem. Eng. J. 428: 132531. https://doi.org/10.1016/j.cej.2021.132531

193. Yang Y, Zeng G, Huang D, Zhang C, He D, Zhou C, Wang W, Xiong W, Li X, Li B, Dong W, Zhou Y (2020) Molecular engineering of polymeric carbon nitride for highly efficient photocatalytic oxytetracycline degradation and H2O2 production. Appl. Catal., B: Environ. 272: 118970. https://doi.org/10.1016/j.apcatb.2020.118970

194. Zhang M, Jiang Y, Xu X, Yu X, Shen W, Luo M, Ding L, Chen H (2022) Facile synthesis of porous 1,3,5-Trihydroxybenzene substituted g-C3N4 for boosted photocatalytic Rhodamine B degradation and H2O2 production. J. Alloys Compd. 925: 166604. https://doi.org/10.1016/j.jallcom.2022.166604

195. Zhang P, Zhang J, Wang D, Zhang F, Zhao Y, Yan M, Zheng C, Wang Q, Long M, Chen C (2022) Modification of g-C3N4 with hydroxyethyl cellulose as solid proton donor via hydrogen bond to enhance H2O2 production. Appl. Catal., B: Environ. 318: 121749. https://doi.org/10.1016/j.apcatb.2022.121749

196. Torres-Pinto A, Boumeriame H, Silva CG, Faria JL, Silva AMT (2023) Boosting Carbon Nitride Photoactivity by Metal-Free Functionalization for Selective H2O2 Synthesis under Visible Light. ACS Sustain. Chem. Eng. https://doi.org/10.1021/acssuschemeng.2c04512

197. Wang A, Liang H, Chen F, Tian X, Yin S, Jing S, Tsiakaras P (2022) Facile synthesis of C3N4/NiIn2S4 heterostructure with novel solar steam evaporation efficiency and photocatalytic H2O2 production performance. Appl. Catal., B: Environ. 310: 121336. https://doi.org/10.1016/j.apcatb.2022.121336

198. Farzin F, Rofouei MK, Mousavi M, Ghasemi JB (2022) A novel Z-scheme oxygen-doped g-C3N4 nanosheet/NaBiS2 nanoribbon for efficient photocatalytic H2O2 production and organic pollutants degradation. J. Phys. Chem. Solids 163: 110588. https://doi.org/10.1016/j.jpcs.2022.110588

199. Zhao X, You Y, Huang S, Wu Y, Ma Y, Zhang G, Zhang Z (2020) Z-scheme photocatalytic production of hydrogen peroxide over Bi4O5Br2/g-C3N4 heterostructure under visible light. Appl. Catal., B: Environ. 278: 119251. https://doi.org/10.1016/j.apcatb.2020.119251

200. Yang Y, Zeng Z, Zeng G, Huang D, Xiao R, Zhang C, Zhou C, Xiong W, Wang W, Cheng M, Xue W, Guo H, Tang X, He D (2019) Ti3C2 Mxene/porous g-C3N4 interfacial Schottky junction for boosting spatial charge separation in photocatalytic H2O2 production. Appl. Catal., B: Environ. 258: 117956. https://doi.org/10.1016/j.apcatb.2019.117956

201. Yang Q, Li R, Wei S, Yang R (2022) Schottky functionalized Z-scheme heterojunction photocatalyst Ti2C3/g-C3N4/BiOCl: Efficient photocatalytic H2O2 production via two-channel pathway. Appl. Surf. Sci. 572: 151525. https://doi.org/10.1016/j.apsusc.2021.151525

202. Zhang H, Bai X (2022) Protonated g-C3N4 coated Co9S8 heterojunction for photocatalytic H2O2 production. J. Colloid Interface Sci. 627: 541-553. https://doi.org/10.1016/j.jcis.2022.07.077

203. Zhong J, Huang J, Liu Y, Li D, Tan C, Chen P, Liu H, Zheng X, Wen C, Lv W, Liu G (2022) Construction of double-functionalized g-C3N4 heterojunction structure via optimized charge transfer for the synergistically enhanced photocatalytic degradation of sulfonamides and H2O2 production. J. Hazard. Mater. 422: 126868. https://doi.org/10.1016/j.jhazmat.2021.126868

204. Geng X, Wang L, Zhang L, Wang H, Peng Y, Bian Z (2021) H2O2 production and in situ sterilization over a ZnO/g-C3N4 heterojunction photocatalyst. Chem. Eng. J. 420: 129722. https://doi.org/10.1016/j.cej.2021.129722

205. Hou W-C, Wang Y-S (2017) Photocatalytic Generation of H2O2 by Graphene Oxide in Organic Electron Donor-Free Condition under Sunlight. ACS Sustain. Chem. Eng. 5: 2994-3001. https://doi.org/10.1021/acssuschemeng.6b02635

206. Liang C, Guo H, Zhang L, Ruan M, Niu C-G, Feng H-P, Wen X-J, Tang N, Liu H-Y, Zeng G-M (2019) Boosting molecular oxygen activation ability in self-assembled plasmonic p-n semiconductor photocatalytic heterojunction of WO3/Ag@Ag2O. Chem. Eng. J. 372: 12-25. https://doi.org/10.1016/j.cej.2019.04.137

207. Song H, Wei L, Chen C, Wen C, Han F (2019) Photocatalytic production of H2O2 and its in situ utilization over atomic-scale Au modified MoS2 nanosheets. J. Catal. 376: 198-208. https://doi.org/10.1016/j.jcat.2019.06.015

208. Zhang W, Chen X, Zhao X, Yin M, Feng L, Wang H (2020) Simultaneous nitrogen doping and Cu2O oxidization by one-step plasma treatment toward nitrogen-doped Cu2O@CuO heterostructure: An efficient photocatalyst for H2O2 evolution under visible light. Appl. Surf. Sci. 527: 146908. https://doi.org/10.1016/j.apsusc.2020.146908

209. Liu L, Gao M-Y, Yang H, Wang X, Li X, Cooper AI (2021) Linear Conjugated Polymers for Solar-Driven Hydrogen Peroxide Production: The Importance of Catalyst Stability. J. Am. Chem. Soc. 143: 19287-19293. https://doi.org/10.1021/jacs.1c09979

210. Wang H, Yang C, Chen F, Zheng G, Han Q (2022) A Crystalline Partially Fluorinated Triazine Covalent Organic Framework for Efficient Photosynthesis of Hydrogen Peroxide. Angew. Chem., Int. Ed. 61: e202202328. https://doi.org/10.1002/anie.202202328

211. Yu X, Viengkeo B, He Q, Zhao X, Huang Q, Li P, Huang W, Li Y (2021) Electronic Tuning of Covalent Triazine Framework Nanoshells for Highly Efficient Photocatalytic H2O2 Production. Adv. Sustain. Syst. 5: 2100184. https://doi.org/10.1002/adsu.202100184

212. Shiraishi Y, Hagi T, Matsumoto M, Tanaka S, Ichikawa S, Hirai T (2020) Solar-to-hydrogen peroxide energy conversion on resorcinol–formaldehyde resin photocatalysts prepared by acid-catalysed polycondensation. Commun. Chem. 3: 169. https://doi.org/10.1038/s42004-020-00421-x

213. Shiraishi Y, Matsumoto M, Ichikawa S, Tanaka S, Hirai T (2021) Polythiophene-Doped Resorcinol–Formaldehyde Resin Photocatalysts for Solar-to-Hydrogen Peroxide Energy Conversion. J. Am. Chem. Soc. 143: 12590-12599. https://doi.org/10.1021/jacs.1c04622

214. Gryszel M, Rybakiewicz R, Głowacki ED (2019) Water-Soluble Organic Dyes as Molecular Photocatalysts for H2O2 Evolution. Adv. Sustain. Syst. 3: 1900027. https://doi.org/10.1002/adsu.201900027

215. Jakešová M, Apaydin DH, Sytnyk M, Oppelt K, Heiss W, Sariciftci NS, Głowacki ED (2016) Hydrogen-Bonded Organic Semiconductors as Stable Photoelectrocatalysts for Efficient Hydrogen Peroxide Photosynthesis. Adv. Funct. Mater. 26: 5248-5254. https://doi.org/10.1002/adfm.201601946

216. Yin M, Chen X, Wan Y, Zhang W, Feng L, Zhang L, Wang H (2020) Doping Carbon Nitride Quantum Dots into Melamine-Silver Matrix: An Efficient Photocatalyst with Tunable Morphology and Photocatalysis for H2O2 Evolution under Visible Light. ChemCatChem 12: 1512-1518. https://doi.org/10.1002/cctc.201902045

217. Fuku K, Takioka R, Iwamura K, Todoroki M, Sayama K, Ikenaga N (2020) Photocatalytic H2O2 production from O2 under visible light irradiation over phosphate ion-coated Pd nanoparticles-supported BiVO4. Appl. Catal., B: Environ. 272: 119003. https://doi.org/10.1016/j.apcatb.2020.119003

218. Wang Z, Wang Y, Huang L, Liu X, Han Y, Wang L (2020) La2Zr2O7/rGO synthesized by one-step sol-gel method for photocatalytic degradation of tetracycline under visible-light. Chem. Eng. J. 384: 123380.

219. Kofuji Y, Ohkita S, Shiraishi Y, Sakamoto H, Tanaka S, Ichikawa S, Hirai T (2016) Graphitic Carbon Nitride Doped with Biphenyl Diimide: Efficient Photocatalyst for Hydrogen Peroxide Production from Water and Molecular Oxygen by Sunlight. ACS Catal. 6: 7021-7029. https://doi.org/10.1021/acscatal.6b02367

220. Lu Y, Huang Y, Zhang Y, Huang T, Li H, Cao J-j, Ho W (2019) Effects of H2O2 generation over visible light-responsive Bi/Bi2O2−xCO3 nanosheets on their photocatalytic NOx removal performance. Chem. Eng. J. 363: 374-382. https://doi.org/10.1016/j.cej.2019.01.172

221. Xiong J, Li X, Huang J, Gao X, Chen Z, Liu J, Li H, Kang B, Yao W, Zhu Y (2020) CN/rGO@BPQDs high-low junctions with stretching spatial charge separation ability for photocatalytic degradation and H2O2 production. Appl. Catal., B: Environ. 266: 118602. https://doi.org/10.1016/j.apcatb.2020.118602

222. Chang A-L, Nguyen V-H, Lin K-YA, Hu C (2020) Selective synthesis of ZIFs from zinc and nickel nitrate solution for photocatalytic H2O2 production. Arab. J. Chem. 13: 8301-8308. https://doi.org/10.1016/j.arabjc.2020.04.027

223. Liu Y, Zhao Y, Wu Q, Wang X, Nie H, Zhou Y, Huang H, Shao M, Liu Y, Kang Z (2021) Charge storage of carbon dot enhances photo-production of H2 and H2O2 over Ni2P/carbon dot catalyst under normal pressure. Chem. Eng. J. 409: 128184. https://doi.org/10.1016/j.cej.2020.128184

224. Gryszel M, Markov A, Vagin M, Głowacki ED (2018) Organic heterojunction photocathodes for optimized photoelectrochemical hydrogen peroxide production. J. Mater. Chem. 6: 24709-24716. https://doi.org/10.1039/C8TA08151D

225. Gryszel M, Sytnyk M, Jakešová M, Romanazzi G, Gabrielsson R, Heiss W, Głowacki ED (2018) General Observation of Photocatalytic Oxygen Reduction to Hydrogen Peroxide by Organic Semiconductor Thin Films and Colloidal Crystals. ACS Appl. Mater. Interfaces 10: 13253-13257. https://doi.org/10.1021/acsami.8b01295

226. Węcławski MK, Jakešová M, Charyton M, Demitri N, Koszarna B, Oppelt K, Sariciftci S, Gryko DT, Głowacki ED (2017) Biscoumarin-containing acenes as stable organic semiconductors for photocatalytic oxygen reduction to hydrogen peroxide. J. Mater. Chem. 5: 20780-20788. https://doi.org/10.1039/C7TA05882A

227. Wadnerkar N, Gueskine V, Głowacki ED, Zozoulenko I (2020) Density Functional Theory Mechanistic Study on H2O2 Production Using an Organic Semiconductor Epindolidione. J. Phys. Chem. A 124: 9605-9610. https://doi.org/10.1021/acs.jpca.0c08496

228. Oka K, Winther-Jensen B, Nishide H (2021) Organic π-Conjugated Polymers as Photocathode Materials for Visible-Light-Enhanced Hydrogen and Hydrogen Peroxide Production from Water. Adv. Energy Mater. 11: 2003724. https://doi.org/10.1002/aenm.202003724

229. Khomenko VG, Barsukov VZ, Katashinskii AS (2005) The catalytic activity of conducting polymers toward oxygen reduction. Electrochim. Acta 50: 1675-1683. https://doi.org/10.1016/j.electacta.2004.10.024

230. Mitraka E, Gryszel M, Vagin M, Jafari MJ, Singh A, Warczak M, Mitrakas M, Berggren M, Ederth T, Zozoulenko I, Crispin X, Głowacki ED (2019) Electrocatalytic Production of

Hydrogen Peroxide with Poly(3,4-ethylenedioxythiophene) Electrodes. Adv. Sustain. Syst. 3: 1800110. https://doi.org/10.1002/adsu.201800110

231. Rabl H, Wielend D, Tekoglu S, Seelajaroen H, Neugebauer H, Heitzmann N, Apaydin DH, Scharber MC, Sariciftci NS (2020) Are Polyaniline and Polypyrrole Electrocatalysts for Oxygen (O2) Reduction to Hydrogen Peroxide (H2O2)? ACS Appl. Energy Mater 3: 10611-10618. https://doi.org/10.1021/acsaem.0c01663
232. Wang Y, Vogel A, Sachs M, Sprick RS, Wilbraham L, Moniz SJA, Godin R, Zwijnenburg MA, Durrant JR, Cooper AI, Tang J (2019) Current understanding and challenges of solar-driven hydrogen generation using polymeric photocatalysts. Nature Energy 4: 746-760. https://doi.org/10.1038/s41560-019-0456-5
233. Xu X, Zhong H, Huang W, Sui Y, Sa R, Chen W, Zhou G, Li X, Li D, Wen M, Jiang B (2023) The construction of conjugated organic polymers containing phenanthrenequinone redox centers for visible-light-driven H2O2 production from H2O and O2 without any additives. Chem. Eng. J. 454: 139929. https://doi.org/10.1016/j.cej.2022.139929
234. Zhao W, Yan P, Li B, Bahri M, Liu L, Zhou X, Clowes R, Browning ND, Wu Y, Ward JW, Cooper AI (2022) Accelerated Synthesis and Discovery of Covalent Organic Framework Photocatalysts for Hydrogen Peroxide Production. J. Am. Chem. Soc. 144: 9902-9909. https://doi.org/10.1021/jacs.2c02666
235. Huang W, Luo W, Li Y (2020) Two-dimensional semiconducting covalent organic frameworks for photocatalytic solar fuel production. Mater. Today 40: 160-172. https://doi.org/10.1016/j.mattod.2020.07.003
236. Krishnaraj C, Sekhar Jena H, Bourda L, Laemont A, Pachfule P, Roeser J, Chandran CV, Borgmans S, Rogge SMJ, Leus K, Stevens CV, Martens JA, Van Speybroeck V, Breynaert E, Thomas A, Van Der Voort P (2020) Strongly Reducing (Diarylamino)benzene-Based

Covalent Organic Framework for Metal-Free Visible Light Photocatalytic H2O2 Generation. J. Am. Chem. Soc. 142: 20107-20116. https://doi.org/10.1021/jacs.0c09684

237. Li L, Xu L, Hu Z, Yu JC (2021) Enhanced Mass Transfer of Oxygen through a Gas–Liquid–Solid Interface for Photocatalytic Hydrogen Peroxide Production. Adv. Funct. Mater. 31: 2106120. https://doi.org/10.1002/adfm.202106120

238. Wu Q, Cao J, Wang X, Liu Y, Zhao Y, Wang H, Liu Y, Huang H, Liao F, Shao M, Kang Z (2021) A metal-free photocatalyst for highly efficient hydrogen peroxide photoproduction in real seawater. Nat. Commun. 12: 483. https://doi.org/10.1038/s41467-020-20823-8

239. Miklos DB, Remy C, Jekel M, Linden KG, Drewes JE, Hübner U (2018) Evaluation of advanced oxidation processes for water and wastewater treatment – A critical review. Water Res. 139: 118-131. https://doi.org/10.1016/j.watres.2018.03.042

240. Garcia-Muñoz P, Fresno F, de la Peña O'Shea VA, Keller N (2019) Ferrite Materials for Photoassisted Environmental and Solar Fuels Applications. Top. Curr. Chem. 378: 6. https://doi.org/10.1007/s41061-019-0270-3

241. Li X, Liu W, Ma J, Wen Y, Wu Z (2015) High catalytic activity of magnetic FeOx/NiOy/SBA-15: The role of Ni in the bimetallic oxides at the nanometer level. Appl. Catal., B: Environ. 179: 239-248. https://doi.org/10.1016/j.apcatb.2015.05.034

242. Yalfani MS, Contreras S, Medina F, Sueiras JE (2011) Hydrogen substitutes for the in situ generation of H2O2: An application in the Fenton reaction. J. Hazard. Mater. 192: 340-346. https://doi.org/10.1016/j.jhazmat.2011.05.029

243. Underhill R, Lewis RJ, Freakley SJ, Douthwaite M, Miedziak PJ, Akdim O, Edwards JK, Hutchings GJ (2018) Oxidative Degradation of Phenol using in situ Generated Hydrogen Peroxide Combined with Fenton's Process. Johnson Matthey Technology Review 62: 417-425. https://doi.org/10.1595/205651318X15302623075041

244. Sable SS, Georgi A, Contreras S, Medina F (2021) Fenton-like oxidation of phenol with in-situ generated hydrogen peroxide and Pd/Fe-zeolite catalysts. Water-Energy Nexus 4: 95-102. https://doi.org/10.1016/j.wen.2021.06.001

245. Mavrikis S, Perry SC, Leung PK, Wang L, Ponce de León C (2021) Recent Advances in Electrochemical Water Oxidation to Produce Hydrogen Peroxide: A Mechanistic Perspective. ACS Sustain. Chem. Eng. 9: 76-91. https://doi.org/10.1021/acssuschemeng.0c07263

246. Schmidt F, Bernhard M, Morell H, Pascaly M (2014) The HPPO Process - A Novel Route to Propylene Oxide. DGMK Tagungsbericht 2014 3: 243-244.

247. Amano F, Yamaguchi T, Tanaka T (2006) Photocatalytic Oxidation of Propylene with Molecular Oxygen over Highly Dispersed Titanium, Vanadium, and Chromium Oxides on Silica. J. Phys. Chem. B 110: 281-288. https://doi.org/10.1021/jp0557868

248. Nguyen V-H, Lin SD, Wu JC-S (2015) Synergetic photo-epoxidation of propylene over VTi/MCM-41 mesoporous photocatalysts. J. Catal. 331: 217-227. https://doi.org/10.1016/j.jcat.2015.09.001

249. Reed SM, Hutchison JE (2000) Green Chemistry in the Organic Teaching Laboratory: An Environmentally Benign Synthesis of Adipic Acid. J. Chem. Educ. 77: 1627. https://doi.org/10.1021/ed077p1627

250. Sato K, Aoki M, Noyori R (1998) A "Green" Route to Adipic Acid: Direct Oxidation of Cyclohexenes with 30 Percent Hydrogen Peroxide. Science 281: 1646-1647. https://doi.org/10.1126/science.281.5383.1646

251. Shang M (2016) The direct synthesis of adipic acid from cyclohexene and hydrogen peroxide by a continuous micro-flow process, Eindhoven University of Technology (The Netherlands)

252. Burek BO, Bormann S, Hollmann F, Bloh JZ, Holtmann D (2019) Hydrogen peroxide driven biocatalysis. Green Chem. 21: 3232-3249. https://doi.org/10.1039/C9GC00633H

253. Gomez de Santos P, Cervantes FV, Tieves F, Plou FJ, Hollmann F, Alcalde M (2019) Benchmarking of laboratory evolved unspecific peroxygenases for the synthesis of human drug metabolites. Tetrahedron 75: 1827-1831. https://doi.org/10.1016/j.tet.2019.02.013

254. Chenault HK, Whitesides GM (1987) Regeneration of nicotinamide cofactors for use in organic synthesis. Appl. Biochem. Biotechnol. 14: 147-197. https://doi.org/10.1007/BF02798431

255. Holtmann D, Hollmann F (2016) The Oxygen Dilemma: A Severe Challenge for the Application of Monooxygenases? ChemBioChem 17: 1391-1398. https://doi.org/10.1002/cbic.201600176

256. Hofrichter M, Ullrich R (2006) Heme-thiolate haloperoxidases: versatile biocatalysts with biotechnological and environmental significance. Appl. Microbiol. Biotechnol. 71: 276-288. https://doi.org/10.1007/s00253-006-0417-3

257. Fernández-Fueyo E, van Wingerden M, Renirie R, Wever R, Ni Y, Holtmann D, Hollmann F (2015) Chemoenzymatic Halogenation of Phenols by using the Haloperoxidase from Curvularia inaequalis. ChemCatChem 7: 4035-4038. https://doi.org/10.1002/cctc.201500862

258. Björkling F, Godtfredsen SE, Kirk O (1990) Lipase-mediated formation of peroxycarboxylic acids used in catalytic epoxidation of alkenes. J. Chem. Soc., Chem. Commun.: 1301-1303. https://doi.org/10.1039/C39900001301

259. Hofrichter M, Ullrich R (2014) Oxidations catalyzed by fungal peroxygenases. Curr. Opin. Chem. Biol. 19: 116-125. https://doi.org/10.1016/j.cbpa.2014.01.015

260. Karich A, Scheibner K, Ullrich R, Hofrichter M (2016) Exploring the catalase activity of unspecific peroxygenases and the mechanism of peroxide-dependent heme destruction. J. Mol. Catal. 134: 238-246. https://doi.org/10.1016/j.molcatb.2016.10.014

261. Maciá-Agulló JA, Corma A, Garcia H (2015) Photobiocatalysis: The Power of Combining Photocatalysis and Enzymes. Chem. Eur. J. 21: 10940-10959. https://doi.org/10.1002/chem.201406437

262. Özgen FF, Runda ME, Schmidt S (2021) Photo-biocatalytic Cascades: Combining Chemical and Enzymatic Transformations Fueled by Light. ChemBioChem 22: 790-806. https://doi.org/10.1002/cbic.202000587

263. Zhang W, Burek BO, Fernández-Fueyo E, Alcalde M, Bloh JZ, Hollmann F (2017) Selective Activation of C−H Bonds in a Cascade Process Combining Photochemistry and Biocatalysis. Angew. Chem., Int. Ed. 56: 15451-15455. https://doi.org/10.1002/anie.201708668

264. Holtmann D, Krieg T, Getrey L, Schrader J (2014) Electroenzymatic process to overcome enzyme instabilities. Catal. Commun. 51: 82-85. https://doi.org/10.1016/j.catcom.2014.03.033

265. Pan H, Gao Y, Li N, Zhou Y, Lin Q, Jiang J (2021) Recent advances in bicarbonate-activated hydrogen peroxide system for water treatment. Chem. Eng. J. 408: 127332. https://doi.org/10.1016/j.cej.2020.127332

266. Chardon CP, Matthée T, Neuber R, Fryda M, Comninellis C (2017) Efficient Electrochemical Production of Peroxodicarbonate Applying DIACHEM® Diamond Electrodes. ChemistrySelect 2: 1037-1040. https://doi.org/10.1002/slct.201601583

267. Cotillas S, Sánchez-Carretero A, Cañizares P, Sáez C, Rodrigo MA (2011) Electrochemical Synthesis of Peroxyacetic Acid Using Conductive Diamond Electrodes. Ind. Eng. Chem. Res. 50: 10889-10893. https://doi.org/10.1021/ie2009422

268. Cañizares P, Sáez C, Sánchez-Carretero A, Rodrigo MA (2008) Influence of the characteristics of p-Si BDD anodes on the efficiency of peroxodiphosphate electrosynthesis process. Electrochem. commun. 10: 602-606. https://doi.org/10.1016/j.elecom.2008.01.038

269. Davis J, Baygents JC, Farrell J (2014) Understanding Persulfate Production at Boron Doped Diamond Film Anodes. Electrochim. Acta 150: 68-74. https://doi.org/10.1016/j.electacta.2014.10.104